12-2020

Spectroscopic Diagnostics for Supersonic Air Microwave Discharges

James E. Caplinger

SPECTROSCOPIC DIAGNOSTICS FOR SUPERSONIC AIR MICROWAVE DISCHARGES

DISSERTATION

James E. Caplinger

AFIT-ENP-DS-20-D-016

DEPARTMENT OF THE AIR FORCE
AIR UNIVERSITY

AIR FORCE INSTITUTE OF TECHNOLOGY

Wright-Patterson Air Force Base, Ohio

AFIT-ENP-DS-20-D-016

SPECTROSCOPIC DIAGNOSTICS FOR SUPERSONIC DISCHARGES

DISSERTATION

Presented to the Faculty

Graduate School of Engineering and Management

Air Force Institute of Technology

Air University

Air Education and Training Command

in Partial Fulfillment of the Requirements for the

Degree of Doctor of Philosophy in Applied Physics

James E. Caplinger, B.S., M.S.

7 December 2020

AFIT-ENP-DS-20-D-016

SPECTROSCOPIC DIAGNOSTICS FOR SUPERSONIC DISCHARGES

DISSERTATION

James E. Caplinger, B.S., M.S.

Committee Membership:

Dr. Glen P. Perram
Chairman

Major Daniel J. Emmons, PhD
Member

Dr. Carl R. Hartsfield
Member

Dr. Steven F. Adams
Member

AFIT-ENP-DS-20-D-016

Abstract

Optical Emission Spectroscopy (OES) is an increasingly relevant technique in plasma diagnostics due to its inherent non-invasive nature and simple application relative to other popular techniques. In this work, common OES techniques are combined with novel methods, developed here, in an effort to provide comprehensive OES techniques for stationary and supersonic air microwave discharges. To this end, a detailed collisional-radiative model for strong atomic oxygen lines has been developed and used to identify the importance of often overlooked mechanisms including cascade emission and metastable excitation. Using these results, a combined argon actinometry technique was developed which makes use of the two strong oxygen triplets (777 nm and 844 nm) as well as the common N_2/N_2+ method in order to make simultaneous experimental estimates of gas temperature, dissociation fraction, electron temperature and electron density in a medium pressure synthetic air microwave discharge. Finally, a similar technique is proposed and tested in a supersonic flowing air microwave discharge which shows promise for rapid spatial imaging of electron temperature and ionization fraction in high Mach plasma flows.

Acknowledgements

I am sincerely grateful for the expert guidance, consistent support and patience of my advisor, Dr. Glen P. Perram, who has a clear passion for scientific research and is strongly dedicated to the success of his students. In addition to my advisor, the committee was particularly involved and crucial in completing this work. I express my significant gratitude to Major Daniel J. Emmons, Dr. Carl R. Hartsfield and Dr. Steven F. Adams for both joining my committee and consistently supporting my research by lending their unique expertise and valuable time. I also need to acknowledge the help, support, and friendship of my many current and past colleagues in the PPSL who constitute an extremely unique, talented and pleasant group of researchers. Finally, I thank my loving wife and daughter for their support, patience, and companionship every day, especially during my often time consuming education.

Table of Contents

Page

List of Figures

List of Tables

SPECTROSCOPIC DIAGNOSTICS FOR SUPERSONIC DISCHARGES

I. Introduction

The challenge of accurate plasma diagnostics along with the diversity and complexity of modern plasma sources has created a consistent need for a broad toolbox of plasma diagnostic techniques [8]. This need, along with the increasing availability of kinetic and spectroscopic data, has led to a number of novel diagnostic techniques which make use of the rich optical spectrum of low temperature plasmas [9, 10]. Simultaneously, the availability of Boltzmann solvers such as BOLSIG [11] and LoKI-B [12], have removed the often inaccurate requirement of assuming a Maxwellian or otherwise analytic electron energy distribution function (EEDF). Optical emission spectroscopy (OES) plasma diagnostic techniques are attractive due to their non-invasive nature, potential accuracy, and simple implementation. OES and similar plasma diagnostics are the fundamental tools used in experimental plasma physics and allow us to understand, control, and study the physics of our laboratory plasmas. These techniques provide information regarding the densities, temperatures, and energy distributions of charged and neutral particles. In doing so, they enable us to make advances towards applications in over the horizon radar, blackout mitigation and sensing for hypersonic vehicles, as well as space superiority.

As an example, vehicles traveling at high Mach numbers begin to ionize and dissociate the surrounding gases generating a plasma sheath. The plasma sheath can cause the blackout phenomenon in which the plasma is opaque for RF frequencies important for communication and telemetry. This problem has received extensive research since the beginning of the space era, yet still hasn't seen applied solutions. For nearly all proposed solutions, it is necessary to measure plasma parameters, primarily the electron density, in order to

implement the mitigation technique and verify its efficacy [13–16]. Another motivation for characterization of a high speed vehicle's sheath relates more directly to vehicle survivability. The high temperature and chemically kinetic environment requires a great deal of consideration regarding thermal management [17]. Information regarding the chemical composition and temperatures of the sheath could indicate whether ablation and degradation remain at allowable levels. One of the only options for electron diagnostics in this application is passive OES. In terms of air platform applications, the non-invasive nature provides a potentially crucial advantage as an OES sensor could remain conformal or even operate at long stand-off distances. Even though preliminary analysis of spectra can be complex and require detailed numerical models, often for operational systems the results can be distilled to a simple relationship between line ratios and a parameter of interest. This leads to the overall objective of this work: the development a novel and simplified method of determining plasma parameters in a high-Mach vehicles plasma sheath.

To this end, a detailed of study of existing suitable OES methods has been conducted and a novel technique has been developed which uses a combination of the commonly used N_2/N_2^+ ratio along with the prominent infrared atomic oxygen lines (777 nm and 844 nm) to produces simultaneous estimates of multiple plasma parameters including dissociation fraction, electron density, electron density, and gas temperature. This new method makes use of the strong excitation cross section for metastable excitation of the $3p\,^5P$ state [18], which introduces an apparent electron density dependence on line ratios involving the 777.4 nm atomic oxygen line. Additionally, a bench-top microwave plasma flow is used to test and explore these techniques in both the case of a subsonic flow and that of a supersonic flow. In chapter II, the basics of microwave discharges, laboratory supersonic flows, and OES are discussed along with a wide review of literature relevant to OES diagnostics in general and those applied to supersonic plasma jets. Chapter III details a relatively complete collisional-radiative model of atomic oxygen developed for this work which is used

to determine the relative importance of excitation mechanisms of O(3p ^{3}P) and O(3p ^{5}P) states. In chapter IV, a novel actinometry technique is explored in the case of the subsonic discharge, which makes use of the results in chapter III. Finally, in chapter V, the use of the previously developed and newly introduced techniques is explored in a supersonic microwave plasma flow.

II. Background

2.1 Microwave Discharges

Microwave discharges, or gas discharges driven by microwave frequency (300 MHz – 300 GHz) electromagnetic waves, are one of the most common methods of driving laboratory plasmas. They are versatile in application and may offer several advantages over other plasmas sources: operation at pressures ranging from atmospheric to below 1 mTorr, electrode-less configurations, and operation at wide ranges of power and plasma volume [19]. Additionally, many examples in literature have shown that microwave discharges are capable of being sustained in supersonic flows [19–23] at relatively low power when compared to alternative methods using DC or inductively coupled RF sources. Plasmas can be generated using microwave sources in a variety of ways. Some common applications include electron cyclotron resonance sources (ECR), surface wave discharges, cavity microwave discharges, and waveguide microwave discharges. For this work, the focus will be the simple application of a waveguide microwave discharge, in which a discharge tube is passed through a rectangular microwave waveguide and plasma is excited by standing microwave modes [24]. For the waveguide and antenna used in this work, a rectangular WR-340 (43 $\times$ 86 mm) type waveguide, the fundamental mode is the transverse electric ($m,n = 1,0$) or TE10 mode [25]. The transverse electric mode satisfies the condition that $E_z = 0$, where z is the longitudinal dimension of the waveguide and the dominant direction of the wave vector (k). The electric field is then only in the x and y or transverse directions in the waveguide. For the 10 mode, where the first index is by convention the larger of the two dimensions, the electric field oscillates primarily along the short side of the waveguide and is sinusoidal in magnitude along z. This mode is shown in figure 1 below within the dimensions of the WR-340 waveguide for 2.54 GHz microwave operating at 6 kW waveguide power.

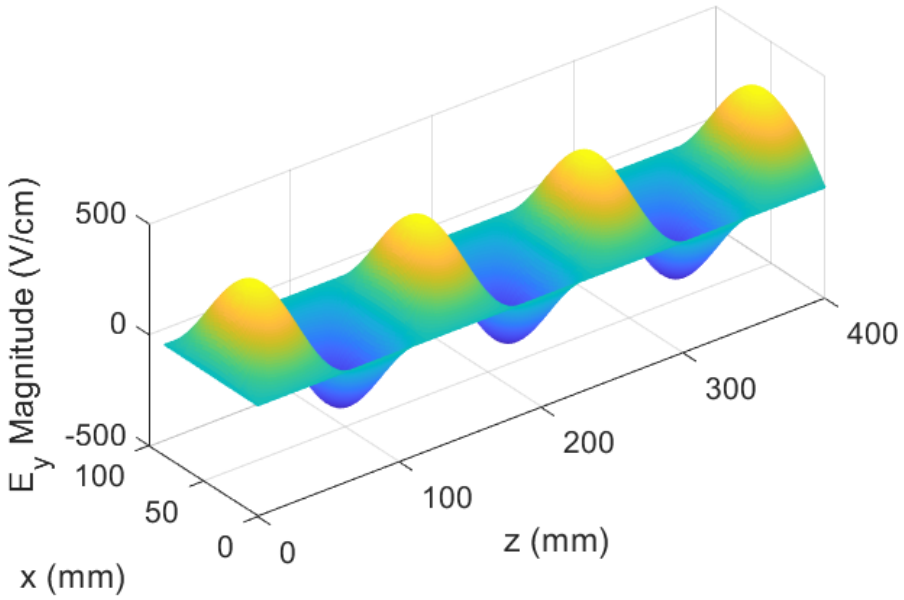

Figure 1. Electric field spatial distribution for the TE10 mode and a microwave power of 6 kW

For waveguide microwave discharges, it is standard practice to position the dielectric discharge tube through the shortest transverse dimension at $\lambda/4$ from the terminating end of the waveguide. From figure 1, the reason for this becomes obvious, as this configuration would place the discharge tube in the maxima of electric field amplitude with the field pointing along the length of the tube. Microwave discharges, not unlike other wave heated type discharges, are generated when the electric field is sufficiently strong to produce a cascade of ionization. For the case of air (N_2 and O_2), with ionization energies of approximately 15.581 and 12.07 eV, corresponding to ultra-violet (UV) photons near 100 nm in wavelength ($f > 10^6$ GHz), microwave photons alone will not create any ionization [26]. For this reason, microwave discharges (along with all MW, RF, and DC discharges), require the presence of seed electrons, though the addition of excited neutrals may aid ignition. If the electric field from the microwave source is strong enough to accelerate seed electrons to an energy greater than the neutral ionization energy (electron speeds $> 2 \times 10^6$ m/s at 12.07 eV) before an electron-neutral collision, a cascade ionization can occur, resulting in

breakdown. The breakdown threshold for the case of continuous or long pulse is given by [26],

$$\mathrm{E}_b = 3.684\ \mathrm{P}\left(1 + f^2/\nu_c^2\right)^{1/2}\ kV/m, \tag{1}$$

where E_b is the electric field threshold necessary for breakdown, P is the pressure in Torr, f is the microwave frequency, and ν_c is the electron-neutral collision frequency. For N_2, the electron-neutral momentum transfer collision frequency can be expressed as [27],

$$\nu_{e-\mathrm{N}_2} = 2.33 \times 10^{-11} n_{\mathrm{N}_2}\left(1 - 1.21 \times 10^{-4}\mathrm{T}_e\right)\mathrm{T}_e\ s^{-1}, \tag{2}$$

where T_e is in units of eV and n_{N_2} is in cm^{-3}. If it is assumed that $1.21 \times 10^{-4}\ \mathrm{T}_e << 1$, and write the N_2 density as a function of pressure, the approximate collision frequency can be written as

$$\nu_{e-\mathrm{N}_2} = 225\mathrm{T}_e\mathrm{P}\ \mathrm{MHz}\ eV^{-1}\ \mathrm{Torr}^{-1}. \tag{3}$$

Using the above collision frequency along with a 2.54 GHz microwave frequency, 1 eV electrons and 1 Torr pressure, the breakdown field can be shown to be approximately 417 V/cm. Also, in the case of atmospheric pressure and $\nu_{e-\mathrm{N}_2} >> f$ it can be seen that equation 1 approaches the known DC breakdown threshold for air at approximately 2.8 kV/mm [26]. This information is crucial to experimental design, as unwanted waveguide breakdown can be problematic. Other important factors for breakdown include seed electron density and microwave pulse length, with breakdown threshold field increasing with decreasing pulse length [26].

2.2 Electron Energy Distribution Functions

The electron energy distribution function (EEDF), also commonly expressed as an electron energy probability function (EEPF), gives the fraction of the electron population at all

possible energies. For this work, accurate knowledge of this distribution function is crucial. This is due to the fact that the production rates of radiative species are often dominated by direct electron impact excitation (EIE). In fact, optical emission spectroscopy relies in many cases on the dominance of EIE in order to indirectly probe plasma properties. In order to determine direct electron excitation rates, the appropriate cross section along with an estimate of the electron energy distribution function (EEDF) are required. The direct impact electron excitation rate, $k_e^{(j)}$, for some transition $i \rightarrow j$ can be calculated as

$$k_e^{(j)} = \left\langle \sigma_{i\rightarrow j} \mathrm{v}_e \right\rangle = 100\sqrt{2e/m} \int_{U_{th}}^{\infty} \sigma_{i\rightarrow j}(U) f_e(U) \sqrt{U} dU, \tag{4}$$

where $\sigma_{i\rightarrow j}$ is the direct impact electron excitation cross section for the transition in cm^2, v_e is the electron speed, e is the fundamental charge, m is the mass of an electron in kg, f_e is the EEDF in units of eV^{-1}, and U is the energy in eV. The coefficient $100\sqrt{2e/m}$ represents the speed of an electron at 1 eV in cm/s [28]. f_e is often also expressed alternatively in units of $\mathrm{eV}^{-3/2}$ (EEPF), as is the case of the default BOLSIG+ output, and that in this case the integral in equation 4 should include an additional $\sqrt{U}$ as the EEDF (f_e) is scaled by that factor relative to the EEPF. The EEDF is the electron solution to the Boltzmann equation for a given discharge, which along with its moments, form the basis of the kinetic theory. A general form of the Boltzmann equation, in the context of gaseous discharges, is [11],

$$\frac{\delta f}{\delta t} + \mathbf{v} \cdot \nabla f - \frac{e}{m} \mathbf{E} \cdot \nabla_v f = \mathrm{C}[f]. \tag{5}$$

Here $f(r,v,t)$ is the time dependent 6-dimensional phase space distribution function which is defined as the function which produces the total number of particles with range $\Delta^3 r \Delta^3 v$ at time t [26], r is the position coordinate, and v is the velocity. Additionally in equation 5, $\mathbf{E}$ is the electric field, e and m are the charge and mass of an electron, and C is a function that describes time evolution of f due to collisional momentum transfer. C can be seen here

as a source term. The most commonly assumed solution to equation 5 is the well-known Maxwellian distribution, for the case of thermal equilibrium [26, 29],

$$f_e(U) = 2\sqrt{\frac{U}{\pi}}\mathrm{T}_e^{-3/2}e^{-U/\mathrm{T}_e}. \tag{6}$$

The Maxwellian EEDF is commonly used to describe many types of laboratory plasmas, including non-equilibrium plasmas, even when the actual EEDF may be non-Maxwellian. This is typically because often the actual EEDF is unknown and the Maxwellian is easily handled and may be a fair approximation for some applications. The value in using an EEDF such as the Maxwellian is that it may be described by a single parameter, the temperature. The entire idea of an electron temperature, which is used with ubiquity in plasma physics, relies on the EEDF being Maxwellian. However, as the solution to the two-term Boltzmann equation relies primarily on the reduced electric field E/N and for any resulting EEDF corresponding to a specific E/N, an effective electron temperature can be found as 2/3 the mean electron energy. In this case the effective electron temperature can be used as an intuitive label for the EEDF and associated E/N. For this work, the assumption that the EEDF is Maxwellian may not be valid, especially for use in equations such as equation 4, where production rates of radiative species are highly sensitive to EEDF shape and the projection of species dependent cross sections on that shape. Any resulting error in rate calculations will propagate to spectral line intensities and be compounded in spectra line ratios. As is shown in later sections, the spectroscopic techniques of interest in this work rely heavily on those spectral line ratios in order to accurately predict electron density. For this reason, the example of many similar OES analyses in literature is followed, in which the EEDF is calculated numerically using BOLSIG+, a Boltzmann solver developed by Hagelaar and Pitchford [11]. BOLSIG+ is an efficient small program which solves for the steady state two-term approximation of the Boltzmann equation for electrons in a spatially uniform electric field [11]. Figure 2 below shows an example of using BOLSIG+ to calcu-

late the EEDF for the case of an air microwave discharge at medium pressure as compared with two analytic EEDFs.

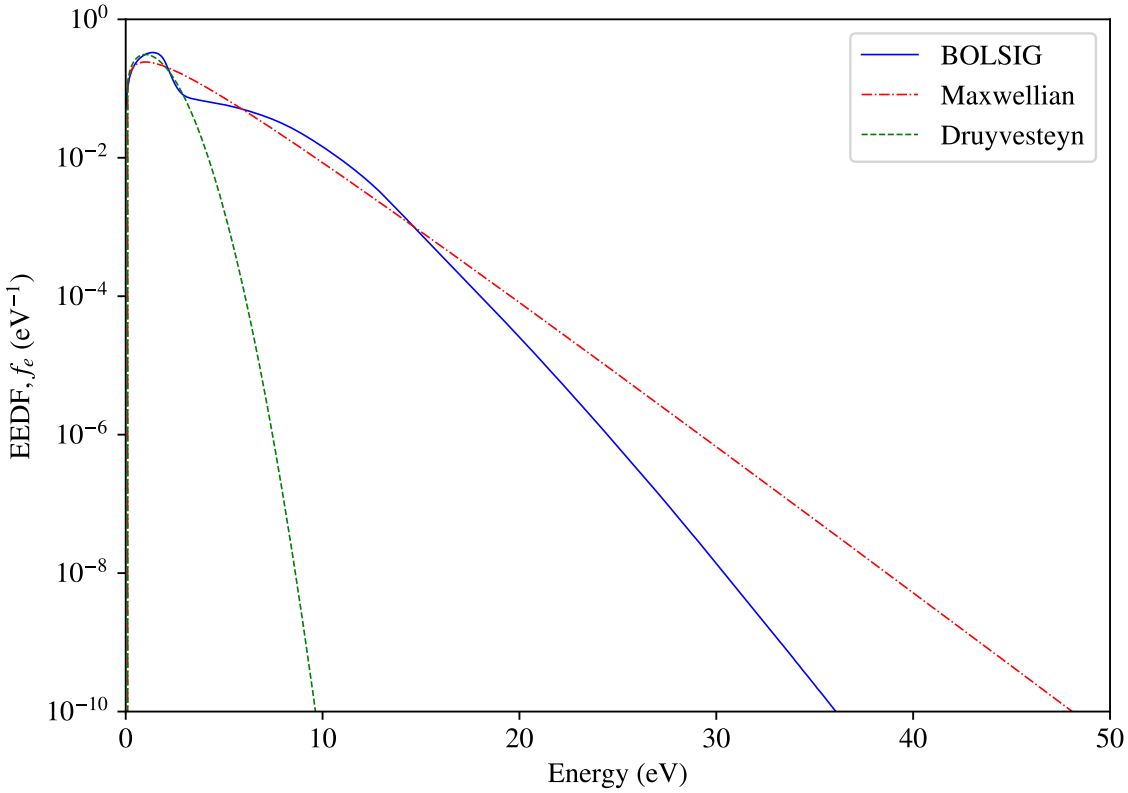

Figure 2. Comparison of analytical and numerically (BOLSIG+) calculated EEDFs for a medium pressure air discharge with $T_e = 2\ eV$ for each.

The solver accepts tabulated collisional cross sections and therefore can accurately account for collisional energy transfer for any electron-electron or electron-neutral collisions as long as accurate cross sections are available. The BOLSIG+ EEDF in the figure above was calculated using available cross sections for N_2 and O_2. For comparison with the analytical functions, which were calculated for an electron temperature of 2 eV, the BOLSIG EEDF reflects an 'effective' temperature of $(2/3)\langle U_e \rangle = 2$ eV. The Druyvesteyn function is a distribution function which assumes electron-neutral collisions are elastic or rather have constant cross sections, an approximation which is reasonable for certain gases at low energies such as H_2 and helium [29]. This approximation results in a similar analytic

expression to that of the Maxwellian distribution in equation 6 except that the quantity in the exponential is squared $\left(e^{-(U/\mathrm{T}_e)^2}\right)$. Some authors will freely vary the exponent of the $(U/\mathrm{T}_e)^x$ term from $x = 1$ to $x = 2$ in order to fit their experimental EEDFs on a continuous scale between the Maxwellian and Druyvesteyn solutions [30]. If the BOLSIG+ solution from initial calculations is accurate, it is indeed the case that our experimental EEDF will be highly non-Maxwellian and any analytical form will likely induce large error into the OES intensity predictions. Even with the BOLSIG EEDF solution, an 'effective' or average temperature to describe the overall energy distribution can be used. This temperature can be shown to be $\mathrm{T}_{eff} = (2/3)\langle \mathrm{U}_e \rangle$, where $\langle \mathrm{U}_e \rangle$ is the average electron energy [9]. All electron temperatures reported in the modeling and experimental results of this work refer to this effective electron temperature.

2.3 Basic Spectroscopic Models for Air Plasmas

One of the most striking features of plasmas is their characteristic glow. This glow is a result of a complex set of excitation mechanisms and subsequent relaxation by spontaneous emission. This set of mechanisms and its corresponding emission spectrum varies significantly depending on plasma conditions. As such, an optical emission spectrum produced by a bulk plasma contains a wealth of information regarding relative densities and energy distributions of all radiative species as well as non-radiative species, such as electrons and metastable states, which often significantly influence the populations of strongly radiative states. Basic spectroscopic models such as the ones discussed below provide the framework for the more advanced models used and developed in chapters III and IV. All such models approximate the relationship between emission intensity and experimental parameters. For this reason, these models and others enable the estimation of electron temperature, electron density, neutral densities, dissociation fractions, rotational temperatures, vibrational distribution functions, as well as other relevant parameters.

Line Intensities and the Corona Model.

For spontaneous emission from an excited atomic or molecular species to a lower state ($i \rightarrow k$), the radiated intensity from a volume V and a solid angle Ω is given by

$$I_{ik} = (V\Omega) A_{ik} h\nu_{ik} n_i, \tag{7}$$

where A_{ik} is the Einstein A coefficient for the transition, $h\nu_{ik}$ is the energy of the emitted photon and n_i is the number density in the initial or upper state i [31,32]. If the transition is a multiplet, consisting of multiple $J \rightarrow J'$ transitions, and it may not be possible to resolve and measure the intensity of each line in the multiplet independently, it is necessary to calculate the effective multiplet Einstein A coefficient. For multiplet transitions, the total emitted intensity is

$$I_{ik} = (V\Omega) \sum_J \sum_{J'} A_{ik}(J,J') h\nu_{ik}(J,J') n_{i,J}, \tag{8}$$

where $n_{i,J}$ is the density of state i in level J ($n_i = \sum_J n_{i,J}$). In the case where only the lower state has spin-orbit splitting and the upper state consists of only one J state, equation 8 simplifies to $I_{ik} = (V\Omega) \sum_{J'} A_{ik}(J,J') h\nu_{ik}(J,J') n_i$, since the total density in the upper state is $n_{i,J}$. If instead the upper state does have spin-orbit splitting, then density of each upper J state must be calculated. If the states are statistically distributed, the densities are given by

$$n_{i,J} = \frac{n_i (2J+1) e^{-E_{i,J}/k\mathrm{T}}}{q}, \tag{9}$$

where q is the partition function, k is the Boltzmann constant, T is the temperature and $2J+1$ is the degeneracy of level J, and $E_{i,J}$ is the energy of the state. Due to the small energy spacing of the fine structure, it is a fair approximation that $E_{i,J} \approx E_i$, for all J. Thus the temperature dependence, which is also present in the partition function q cancels. A similar approximation can be made of $h\nu$ in equation 8. In this case equation 9 is simply

$n_{i,J} = n_i (2J+1)/q$, where $q = \sum_J (2J+1)$ and is equal to the total degeneracy of state i, $g_i = (2L+1)(2S+1)$, where L is the coupled orbital angular momentum, and S is the coupled spin [32]. Thus, the total multiplet emission intensity in equation 8 can be written as

$$I_{ik} = (V\Omega)\, h\nu_{ik} n_i \sum_J \sum_{J'} \frac{A_{ik}(J,J')\,(2J+1)}{g_i}, \tag{10}$$

and the effective multiplet Einstein A coefficient for the transition $i \rightarrow k$ can be seen to be

$$A'_{ik} = \sum_J \sum_{J'} \frac{A_{ik}(J,J')\,(2J+1)}{g_i}. \tag{11}$$

In this way, according to equation 11, effective Einstein A coefficients for multiplet transitions have been calculated for atomic oxygen transitions important for this work. These values and other important radiative parameters, along with values for other relevant species are given in table 1 below.

Table 1. Einstein A coefficients, wavelengths, and upper state radiative lifetimes for optical transitions relevant to this work. Radiative lifetimes for N_2 and N_2^+ represent the inverse of the sum of radiative rates originating from the upper vibrational state rather than the effective lifetime of electronic state and were taken from Gilmore et al. [1]. Wavelengths for N_2 and N_2^+ represent the band origin.

Species	Transition ($i \rightarrow k$)	A_{ik} (s^{-1})	$\tau_i(s)$	λ (nm)	Ref.
O	$3s\ ^5S^\circ \rightarrow 2p^4\ ^3P$	5.56e3	1.80e-4	135.7	[33]
O	$4d\ ^5D^\circ \rightarrow 3p\ ^5P$	7.62e6	7.11e-8	615.7	[33]
O	$3p\ ^5P \rightarrow 3s\ ^5S^\circ$	3.69e7	2.71e-8	777.4	[33]
O	$3p\ ^3P \rightarrow 3s\ ^3S^\circ$	3.22e7	3.11e-8	844.6	[33]
Ar	$4p'^{\,2}\left[{}^1/_2\right]_0 \rightarrow 4s'^{\,2}\left[{}^1/_2\right]_1^\circ$	4.50e7	2.21e-8	750.4	[33]
N_2	$N_2(C^3\Pi_u)_{v=0} \rightarrow N_2(B^3\Pi_g)_{v=2}$	8.91e6	3.67e-8	380.4	[1]
N_2^+	$N_2^+(B^2\Sigma_u^+)_{v=0} \rightarrow N_2^+(X^1\Sigma_g^+)_{v=0}$	1.21e7	5.55e-8	391.4	[1]

Optical emission spectroscopy techniques typically use ratios of strong atomic and molecular lines whose driving mechanisms can be reduced to a few important processes which are dominantly driven by parameters of interest. In the case of electron tempera-

ture and electron density diagnostics, it is ideal if electron processes such as direct electron impact excitation dominate production while optically accessible spontaneous emission dominates loss. The simplest example of this situation is known as the corona model, in which population only occurs specifically via direct electron impact excitation from the ground state. In this case, the steady state density of some excited state j can be written as

$$n_j = \frac{n_0 n_e k_e^{(j)}}{\sum_{i<j} A_{ij}}, \tag{12}$$

where n_j is the steady state density, n_0 is the ground state density, n_e is the electron density, and $k_e^{(j)}$ is the electron excitation rate as calculated by equation 4. Substituting the above density in the line intensity expression in equation 7, the line intensity in the case of the corona model can be written as

$$I_{ik} = (V\Omega)\frac{A_{ik} h\nu_{ik} n_0 n_e k_e^{(j)}}{\sum_{i<j} A_{ij}}, \tag{13}$$

Where A_{ik} and A_{ij} are the effective multiplet Einstein A coefficients, A'_{ik} and A'_{ij}, when appropriate. This basic model, forms the foundation for all of the spectroscopic diagnostic techniques discussed and developed in chapters III and IV. In the chapters that follow, the superscript for rates (k^j) is in some cases replaced with two indices referring to the lower and upper states and in other cases the superscript is simply the term symbol for the relevant upper state while the lower state is assumed to be the ground state, unless otherwise stated.

N_2 Rotational-Vibrational Spectra.

The prominent $N_2(C-B)$ second positive system (SPS) along with the $N_2^+(B-X)$ first negative system (FNS) together comprise the vast majority of the near UV spectra for air discharges. In the case of these and other molecular transitions, application of simple spectroscopic models for emission intensity, such as the corona model discussed above, require

the integration of entire vibrational bands. Extracting accurate intensities in the case of this work presents two primary difficulties. The first being that the FNS at 391 nm is overlapped by the $\Delta v = 3$ bands of the SPS. The second difficulty is that SPS $v' \rightarrow v'' = 0 \rightarrow 2$ band is overlapped by the $v' \rightarrow v'' = 1 \rightarrow 3$ band of the SPS. To overcome these issues, the full spectrum is fit ranging from approximately 362 nm to 400 nm using full spectral models of the FNS and SPS which depend on rotational temperatures and a freely varying vibrational distribution. Many full descriptions of this and similar models can be found in a number of publications regarding the popular OES technique of extracting rotational temperatures from the SPS [34–37]. In short, the model calculates the discrete rotational/vibrational energy levels using ro-vibrational molecular constants and the relative intensities using the rotational temperature, a vibrational distribution function, Franck-Condon factors, and Hönl-London factors. These discrete lines are then convolved with a pseudo-Voigt line shape function which has been fit to the instrument line shape. The model makes use of a variety of widely available molecular and radiative data for the SPS and FNS [1, 38, 39]. Alternatively, the band intensities can be approximated by their peak intensities along with analytic equations given in [40]. One significant benefit of fitting the full spectrum is obtaining an estimate of gas temperature, as the rotational temperature of the $N_2(C^3\Pi_u)$ state is reasonably approximated to be equal to the gas temperature [34, 35]. This allows for the use of this measured gas temperature along with operating pressure in order to compute initial gas densities used in calculating neutral gas densities according to the ideal gas law, as well as for any gas-kinetic type scaling temperature of collisional quenching rates. Radiative parameters for FNS and SPS transitions relevant to this work are given in table 1 above. The Einstein A coefficients for vibrational transitions are taken from Gilmore et al. [1] and are related to the total electronic transition Einstein A coefficient by the appropriate $v' \rightarrow v''$ Franck-Condon factors.

2.4 Isentropic flows and Nozzle design

Generation of supersonic laboratory flows are typically accomplished using convergent-divergent nozzles, for example the de Laval nozzle, along with a sufficient pressure differential to support the flow. In the case of most gases, the necessary pressure ratio that must be sustained to reach Mach 1 is near 0.5 [41]. On the convergent side the flow is subsonic and the pressure drops until it reaches the throat where the Mach number is 1, while in the divergent section the pressure decreases further and the flow becomes supersonic [41]. In the supersonic portion of the flow downstream of the exit, the gas temperature drops sharply as the random thermal motion is converted to the higher speed directed flow [42]. The design Mach number of a convergent-divergent nozzle is based on the isentropic flow relation

$$\frac{\mathrm{A}}{\mathrm{A}^*} = \frac{1}{\mathrm{M}}\left[\left(\frac{2}{k+1}\right)\left(1+\frac{k-1}{2}\mathrm{M}^2\right)\right]^{\frac{k+1}{2(k-1)}}, \tag{14}$$

where A is the downstream area (including any boundary layer), A^* is the throat area, M is the Mach number, and k is the ratio of specific heats. A value of $k = 1.4$ is used for the calculations here. If the exit velocity is Mach 3.4, for example, equation 14 yields a ratio of $\mathrm{A}/\mathrm{A}^* \approx 6.5$. Using a similar isentropic relation, the expected pressure ratio as measured by pressure transducers experimentally can be expressed as

$$\frac{\mathrm{P}_i}{\mathrm{P}_f} = \left(1+\frac{k-1}{2}\mathrm{M}^2\right)^{\frac{k}{k-1}}, \tag{15}$$

where P_i and P_f are the pressure before and after nozzle, respectively, relative to the flow direction. In the case of a Mach 3.4 nozzle, the expected pressure ratio is $\mathrm{P}_i/\mathrm{P}_f \approx 71$. These equations will be used as the fundamental tools for the design and testing of the supersonic flow in chapter V.

2.5 Previous Work

N_2 Optical Emission Spectroscopy.

A primary focus of this work is determination of plasma parameters using the $N_2(C-B)$ second positive system and the $N_2^+(B-X)$ first negative system. Because these systems are so dominant in air discharge spectra and their relative kinetics have been shown to be sensitive to plasma parameters, they constitute some of the most promising candidates for OES diagnostics in air. As such, these systems continue to see increasing attention, particularly as a means of determining the reduced electric field (E/N) and electron density of a discharge. There are many examples in recent literature in which electron density is determined using N_2 OES in nitrogen containing plasmas. The first such example is Lebedev and Shakhatov (2005) [43]. The authors developed a novel method for determining electron density and electric field using the vibrational distribution of the $N_2(C^3\Pi_u)$ state. The method used a 68 reaction kinetic model including reactions involving 10 electronic states of N_2 as well as the ground state of atomic nitrogen. The work was performed in a low pressure RF discharge. This method was followed by simpler methods performed by Isola in 2009 [44] as well as Zhu and Pu in 2008 [10] who instead used an intensity ratio of the $N_2(C-B)$ spectra to the $N_2^+(B-X)$ spectra and included far less kinetics. The latter method has become a relatively standard practice and will become the initial focus of this work, despite the fact that it requires either a calibration point or a measurement of absolute irradiance. Isola et al. (2009) [44], in an early example of a typical approach to these techniques, measured electron density and temperature using the ratio of the SPS and FNS bands. The authors did not measure absolute irradiance (as is common in other works [22, 45–48], but rather used one calibration point of electron temperature or density (via Langmuir probe) in order to use a simple ratio technique. This was performed in a medium pressure (2-4 Torr) pure N_2 discharge. Results were shown to agree with Lang-

muir probe measurements. This effort is highly relevant to this work as a similar approach is taken in chapter IV.

Another relevant study was performed in 2013, in which a 16 reaction excitation model was used by Pothiraja et al. [48] to deduce a dependence of electron density and reduced electric field on absolute photoemission of the FNS and SPS in an atmospheric N_2/He pulsed microdischarge. It was assumed that the $N_2(C^3\Pi_u)$ and $N_2^+(B^2\Sigma_u^+)$ states are populated by three primary methods: direct excitation from the ground state, direct excitation from the $N_2(A)$ metastable state and a pooling reaction from the metastable state. The authors then used fast intensified charge-coupled device (ICCD) imaging along with two interference filters, each having an approximately 5 nm full-width at half maximum (FWHM), one centered on the primary band head of the FNS and one centered on the primary band head of the SPS, in order to experimentally determine absolute photo-emission from the two systems. These two values were then used to calculate electron density with high spatial and temporal resolution. If all assumptions used were valid this method is highly novel and useful in determining electron density in atmospheric pressure N_2/He plasmas [35]. A similar approach was taken by Steves et al. (2013) [47], where a 6 mechanism kinetic scheme was used for the $N_2(C^3\Pi_u)$ and $N_2^+(B^2\Sigma_u^+)$ states. This method was used to determine electron density and temperature in a low pressure oxygen RF/Microwave discharges. Here N_2 was mixed into the volume at a 5% ratio as a sensing gas. The authors determined however that the OES analysis alone was not enough to deduce a unique set of electron density and temperature parameters as two solutions produced similar emission intensities. For this reason, a resonance probe was used to confirm the results, validating one of the two possible solutions.

Finally, a recent study by Bílek et al. (2019) [40] conducted a thorough study of the use of the N_2/N_2^+ ratio for determination of reduced electric field in transient discharges for pure nitrogen. This study is a significant contribution as it examines 101 reaction mech-

anisms and provides distilled lists of important mechanisms for specific cases in terms of working pressure and specific vibrational bands used. In the case most relevant to this work, for medium pressure (7.6 Torr) and the use of the FNS(0,0)/SPS(0,2) ratio, the authors highlight the mechanism set used by Isola et al. [44] in addition to several important collisional processes including collisional quenching of $N_2(C^3\Pi_u)$ and $N_2^+(B^2\Sigma_u^+)$ by N_2 as well as V-T relaxation of the $N_2(C^3\Pi_u), v = 1$ to the $N_2(C^3\Pi_u), v = 0$ state. Though the latter process, $N_2(C^3\Pi_u)_{v=1} + N_2 \rightarrow N_2(C^3\Pi_u)_{v=0} + N_2$, for which the rate is comparable to the quenching rates of $N_2(C^3\Pi_u), v = 0$, is difficult to include in simple models as absolute density in $N_2(C^3\Pi_u), v = 1$ is not typically known.

OES using strong atomic oxygen lines.

The two strong oxygen triplets, 844 nm multiplet ($3p^3P \rightarrow 3s^3S^\circ$) and 777.4 nm multiplet ($3p^5P \rightarrow 3s^5S^\circ$) , are among the strongest lines in the optical spectra of air discharges. As is the case of the similarly dominant N_2 spectra, they present one of the best opportunities for passive characterization of air plasmas. Here a brief overview of recent literature which exploit these two lines is provided. A significant fraction of the literature relates regarding these lines relates to actinometry techniques, the previous work regarding those techniques is detailed in chapter IV. The basic emission analysis for these two triplets are generally considered to follow the corona model with addition of a dissociative excitation route from O_2, the importance of which was highlighted in 1991 by Collart et al. [49]. As such the two lines are primarily sensitive to the EEDF or effective electron temperature and the dissociation fraction of the plasma. Several recent studies have made use of these lines in order to make determinations of local electron temperatures. Recently, Tsutsumi et al. (2017) [50] used an advanced actinometry approach which imaged the ratio of the two strong oxygen lines to well know argon lines. This data was used to produce spatially resolved determinations of both dissociation fraction and mean electron energy. In a sim-

ilar study, performed by the same group, Greb et al. (2013) [51], the same method was used and compared well against a more explicit and trustworthy method of two-photon absorption laser-induced fluorescence (TALIF). In 2011, Milosavljevic et al. [52] examined the use of these strong triplets in a fluorocarbon/O_2/argon discharge. The authors note the importance of both cascade emission (as is discussed in great detail in chapter III) and heating of the EEDF tail induced by the presence of the fluorocarbon, on the applicability of the 777 nm for OES diagnostics. This study is also one of the only examples in literature which studies the 615.7 nm multiplet ($4d\ ^5D^\circ \rightarrow 3p\ ^5P$) in any detail. In chapter IV, the 615.7 nm multiplet is examined as a candidate for techniques similar to those which use the other lines discussed above. Previous work regarding these atomic oxygen lines show their great utility as plasma diagnostics as well as potential for application in novel techniques. Though as will be seen in chapters III and IV, there are many considerations which make their applicability highly situational, and the 844 nm line tends to follow the basic models more reliably than that of the 777 nm line.

Supersonic Plasma Jets.

There is a wide variety of interesting applications of supersonic plasma flows, including thin film deposition [53], high speed aerodynamics [20], general material processing [54], laboratory modeling of space vehicle atmospheric entry [42], and gas-dynamic lasers [55]. Therefore the characterization and development of laboratory supersonic flows has been a consistently studied topic for decades. These supersonic plasma flows are characterized by large densities of excited and ground state species which would typically be subject to fast collisional deactivation in stationary discharges, such as metastables, dissociated atoms, and vibrationally excited molecules [56]. Though there are a variety of methods of achieving supersonic plasma flows, their differences are similar to the general differences in typical plasma sources as they are typically direct-current (DC), radio-frequency (RF),

or high frequency microwave driven. The other necessary element is of course a standard converging-diverging nozzle (de Laval), the design of which is complicated by the difficulty of manufacturing materials which can withstand the highly kinetic and high temperature environments generated by the discharges. In the case of DC supersonic discharges, a water-cooled metal nozzle is often used and doubles as either the anode or cathode, as in the case of the experimental work of Lago et al. (2007) [21]. For microwave flows, power has been applied on both the subsonic side of the flow [20, 22] and in the supersonic portion of the flow [57]. For this work, the general design was chosen to follow those who have used microwave excitation in the supersonic portion, with the nozzle incident on the cavity [20, 22]. A good example of an RF supersonic flow is the case of Sember et al. (2002) [58], in which a high power (20 kW) inductively coupled plasma (ICP) torch and de Laval nozzle configuration was expanded into a low pressure chamber.

Numerous diagnostics have been employed on the types of discharges discussed above and follow a trend similar to stationary plasmas. Lago et al. (2007) used OES and a Langmuir probe to study a plasma jet which was produced by a "vortex stabilized dc-arc torch" and the gas used was a CO_2 N_2 mixture. They report rotational and vibrational temperatures from fits of the N_2 SPS as well as electron temperatures (EEDF) from the Langmuir probe. This study was conducted in order to predict conditions for Martian atmospheric entry at hypersonic velocities [21]. Nikolic et al. (2013) built a supersonic microwave excited Mach 2 argon plasma flow, in which a Laval nozzle was coupled into a microwave wave guide and a 2.54 GHz magnetron is used to ionize the Mach flow downstream from the nozzle [22]. Here OES diagnostics of argon were used to produce spatially resolved density distributions of excited argon states. In 2009, Mazouffre and Pawelec [42] used laser induced fluorescence (LIF) to measure the velocity distribution function of the O($3s\ ^5S^\circ$) atomic oxygen metastable in a CO_2 supersonic plasma expansion, by pumping the 777.4 nm multiplet ($3p^5P \rightarrow 3s^5S^\circ$) . The location of shocks are indicated by abrupt in-

creases in the perpendicular temperature of the metastable atoms, additionally, the authors observed a common phenomenon for these types of discharges in which the perpendicular temperature falls below the parallel temperature in the expansion region as collisions are too infrequent to thermalize the two temperatures. LIF appears to be a popular technique in these plasma flows, Broc et al. (2004) [56] used LIF in order to spatially resolve densities of NO, atomic nitrogen, and atomic oxygen in an RF supersonic flow and noted similar axial density distributions for each which approximately follow a Z_{th}^{-2} dependence, where Z_{th} is the axial position downstream relative to the throat. There are many examples in literature of OES measurements of rotational temperatures, including [20,21,56,59,60]. Similar OES techniques, along with LIF techniques for determining species densities, appear to be among the most popular optical diagnostic techniques in plasma flows.

Diagnostics of electron temperatures and densities were not widely found in the literature search conducted for this work, though there are examples, as in [58], where stark broadening of the H_β line was used to determine electron density and a Saha equilibrium was assumed to calculate an electron temperature. In another work, a Langmuir probe was used to characterize the electron population [21], as discussed above. In summary, diagnostics and sources used in supersonic flows are similarly diverse to those used in other laboratory plasmas, but because knowledge of local gas temperatures and densities is more limited in the case of these highly dynamic supersonic flows, more attention is needed to develop diagnostics to measure these basic bulk gas properties.

III. Atomic Oxygen Collisional-Radiative Model

The corona model, as discussed in section 2.3, along with corrections such as metastable excitation and cascade contributions, has been widely used in plasma diagnostics, particularly in plasmas with a single atomic or molecular species or with trace amounts of a second species. [9, 10] However, in air plasmas, due to the vast number of reactive species and non-equilibrium processes present, this corona approximation and its extensions are often not predictive of actual spectra. This is especially true for medium (near 1 Torr) and high pressure plasmas (atmospheric pressure) where quenching rates with neutral species are high. However, if quenching rates are known and electron excitation and spontaneous emission rates are sufficiently high, line intensities can still be strongly dependent on electron parameters even in complex multispecies plasmas. [61]

Such an opportunity is presented by the strong optical lines of excited atomic oxygen. For example, the 844 nm oxygen line originating from the 3p ^{3}P $\rightarrow$ 3s ^{3}S$^\circ$ transition has a condensed set of mechanisms accepted in literature [62] based on only quenching, electron impact excitation from the ground state, and spontaneous emission (though dissociative excitation is considered for high electron temperatures). For the remainder of this dissertation, this set of mechanisms is referred to as the extended corona model. In this situation, the steady state density for the 3p ^{3}P state can be written as

$$n_{\left(3p\,^3P\right)} = \frac{n_O n_e < \sigma_e v_e > + n_{O_2} n_e < \sigma_{de} v_e >}{\sum_{f<i} A_{if} + \sum_m n_m Q_{im}}, \tag{16}$$

where σ_e and σ_{de} are the electron impact excitation and dissociation excitation cross sections, respectively, v_e is the electron speed, n_O, n_{O_2}, n_e, and n_m are the atomic oxygen, molecular oxygen, electron, and quencher densities, respectively, A_{if} is the Einstein coefficient for spontaneous emission transition $i \rightarrow f$ and Q_{im} is the quenching rate for species i on quencher m. This analytic 2 level, 4 mechanism model (extended corona model) de-

pends only on electron temperature or the electron energy distribution function (EEDF), electron density, pressure, and dissociation fraction. For this reason, the 844 nm line can be and is used as a diagnostic and for model validation. Recently, these basic assumptions have been extended to the similarly intense line at 777 nm from the 3p ^{5}P $\rightarrow$ 3s ^{5}S$^\circ$ transition [50, 51, 63]. In this case, the ratio of 777 nm to the 844 nm line ratio can be found to be

$$\frac{I_{777nm}}{I_{844nm}} = \frac{A_{777}\lambda_{844}\tau_{5P}}{A_{844}\lambda_{777}\tau_{3P}}\left[\frac{n_O k_e^{5P} + n_{O_2} k_{de}^{5P}}{n_O k_e^{3P} + n_{O_2} k_{de}^{3P}}\right], \tag{17}$$

where τ is the lifetime of the species, and k is the appropriate rate calculated from $<\sigma v_e>$, where the brackets denote the mean value. The utility of the above expression is obvious since an experimentally measured ratio is only a function of two unknowns, dissociation fraction and electron temperature or EEDF, as electron density and molecular oxygen densities cancel. Used along with other experimental data this method has been effective in determining both unknowns [50,51,63]. However, quenching rates for common species besides molecular oxygen are not available in literature for the 3p ^{5}P state which makes use of the 777 nm line more problematic in air plasmas. Additionally, besides limited positive diagnostic results, this extended corona model has not been thoroughly validated. Unlike commonly used rare-gas diagnostic techniques, this extended corona model for oxygen lacks any accounting for metastable excitation or cascade contributions. The latter is commonly neglected for oxygen states due to the recommended and available cross sections being direct electron excitation cross sections rather than apparent cross sections which include cascade effects. The objectives of this chapter are to test the validity of the extended corona model for modeling the 777 nm / 844 nm line ratio and to quantify the impact of electron excitation from the metastables (^{1}S, ^{1}D, and 3s ^{5}S$^\circ$) and the low lying 3s ^{3}S$^\circ$ state, as well as cascade emission from higher lying states.

For these reasons, a collisional-radiative model has been developed for atomic oxygen

valid for a range of gas compositions using the best available cross sections and collisional rates [3, 7, 18, 62, 64]. Although other thorough collisional-radiative models for atomic oxygen exist in literature [61, 65, 66], none were suited to answer the questions posed here and each would benefit from a more modern rate package. The basis of the model is a 96 level system which considers electron impact excitation, electron impact de-excitation, electron impact dissociative excitation, spontaneous emission, and quenching from 10 collisional partners. Additionally, effective cascade emission cross sections are calculated to account for cascade emission populating of the 3p ^{3}P and 3p ^{5}P states. The inclusion of a cascade rate using this cross section is less ideal than using apparent cross sections, which is recommended for OES diagnostic techniques [9]. However, the commonly used and recommended cross sections for the oxygen states considered here are direct cross sections that are either measured or calculated as direct cross sections or cascade corrected apparent cross sections [7]. A potential advantage of this approach is that apparent cross sections are inherently pressure dependent due to radiation trapping. The calculated 777 nm/844 nm oxygen line ratio is calculated and presented using (1) the 96 level collisional-radiative model, (2) the extended corona model, and (3) the extended corona model including cascade contributions. Mechanisms accounting for discrepancies between the models are identified using a rate sensitivity analysis.

3.1 Kinetic Model

The collisional-radiative model developed here is a mechanism reduced version of the general approach of Vlcek et al. [28]. The model considers the following processes: (1) direct electron impact excitation (k_e^{if}) and de-excitation (k_{ed}^{if}) where i and f are the level indices given in Table 2, (2) dissociative excitation (k_{de}^{f}) from molecular oxygen, (3) quenching from a number of collisional partners as detailed in Table 7, and (4) spontaneous emission. In the equations below the energy ordered state indices, i and f, represent the initial

and final states of the process, respectively. In the case of dissociative excitation the product O_l is arbitrary. Table 2 gives a summary of the lowest 10 states used in this model.

$$O_i + e^- \underset{k_{ed}^{if}}{\overset{k_e^{if}}{\longleftrightarrow}} O_f + e^- \tag{18}$$

$$O_2 + e^- \xrightarrow{k_{de}^{f}} O_f + O_l + e^- \tag{19}$$

$$O_i + m \xrightarrow{k_q^{if}} O_f + m \tag{20}$$

$$O_i \xrightarrow{A_{if}} O_f + \gamma \tag{21}$$

Table 2. First 10 oxygen levels considered

index	Configuration	Term	g	E (eV)
0	$2s^2 2p^4$	^{3}P	9	0.009668
1	$2s^2 2p^4$	^{1}D	5	1.967364
2	$2s^2 2p^4$	^{1}S	1	4.189746
3	$2s^2 2p^3(4S^\circ)3s$	$^5S^\circ$	5	9.146091
4	$2s^2 2p^3(4S^\circ)3s$	$^3S^\circ$	3	9.521364
5	$2s^2 2p^3(4S^\circ)3p$	^{5}P	15	10.740638
6	$2s^2 2p^3(4S^\circ)3p$	^{3}P	9	10.988841
7	$2s^2 2p^3(4S^\circ)4s$	$^5S^\circ$	5	11.837606
8	$2s^2 2p^3(4S^\circ)4s$	$^3S^\circ$	3	11.930385
9	$2s^2 2p^3(4S^\circ)3d$	$^5D^\circ$	25	12.078633
10	$2s^2 2p^3(4S^\circ)3d$	$^3D^\circ$	15	12.087030

Quenching.

The first order decay rate coefficients, k_q^{if} represent the quenching from all collisional partner species m which produce the transition $i \to f$. The total quenching of the state i is

calculated as

$$\sum_f k_q^{if} = \sum_m Q_{im} n_m. \tag{22}$$

Where Q_{im} are the literature rates for quenching of oxygen species i by collision partner species $m = N_2, O_2, Ar, etc.$ as summarized in table 7, and n_m is the density of the m^{th} quencher. As the majority of quenching rates are not reported with a temperature dependence and have been measured at 300 K when indicated, a gas temperature of 300 K was assumed for all calculations in this work, rather than extrapolating the rates to higher temperatures. Quenching rates for many excited states are not available in literature. In cases with blank entries in table 7, rates were assumed to be zero. In the case of the 3s ^{3}S$^\circ$ state, quenching rates were assumed to be equal to that of the 3s ^{5}S$^\circ$ state, as quenching rates for the latter were found for common collision partners in [67]. Similarly, rates for quenching of 3p ^{5}P for collision partners besides O_2 were assumed to be equal to those of the 3p ^{3}P, as this assumption has been used by [3, 63]. In the case of quenching of 3p ^{3}P and 3p ^{5}P on O_2, rates have been measured and taking the approximation above would have yielded an error of approximately 15%, with measured rate uncertainties reported to be 5.3% and 16.7% for the 3p ^{3}P [2] and 3p ^{5}P [3] states, respectively. Thus, in the only case where data is available, our above assumptions are within rate coefficient measurement error. For excited states above the 3p ^{3}P state ($i > 6$), quenching rates were neglected.

Because products in quenching processes are typically not detailed for published rates, and it was ideal to conserve density; an approximate scheme was developed in order to estimate branching coefficients. This allowed for estimates of the rate k_q^{if} to be used rather than the sum over all f. As an estimate, the normalized maxima of the electron impact excitation cross sections was chosen as these branching coefficients. Thus the quenching rates were calculated as

$$k_q^{if} = \frac{\max(\sigma_e^{if})}{\sum_{k<i, k\neq f} \max(\sigma_e^{ik})} \sum_m Q_{im} n_m \tag{23}$$

Table 3. Quenching rates used for this work ($cm^3\ s^{-1}$). Temperature dependent rates were evaluated at 300 K. Values with † are assumed.

$m\backslash i$	^1D	^1S	$3s\ ^5S^\circ$	$3s\ ^3S^\circ$	$3p\ ^5P$	$3p\ ^3P$
N_2	2.3e-11 [62]	1.0e-17 [62]	3.5e-11 [67]	3.5e-11†	5.9e-10†	5.9e-10 [2]
O_2	3.4e-11 [62]	2.4e-13 [62]	2.2e-10 [67]	2.2e-10†	1.1e-09 [3]	9.3e-10 [2]
Ar	5.9e-13 [68]	-	2.9e-15 [67]	2.9e-15†	1.0e-10†	1.0e-10 [69]
CO_2	-	-	5.3e-10 [67]	5.3e-10†	-	-
H_2O	-	-	-	-	4.9e-09†	4.9e-09 [69]
O	8.0e-12 [62]	1.8e-11 [62]	-	-	-	-
N	-	1.0e-12 [62]	-	-	-	-
O_3	2.3e-10 [62]	6.0e-10 [62]	-	-	-	-
NO	-	-	1.9e-10 [67]	1.9e-10†	-	-
$O_2(a)$	-	1.7e-10 [62]	-	-	-	-

For comparison of this approximation, there exist a small amount of data regarding branching ratios for quenching of the $3p\ ^3P$ state. Dagdigian et al. [3] measured the branching from $3p\ ^3P$ to the $3p\ ^5P$ to be 8% and 3% for O_2 and N_2 collisional partners, respectively. Uncertainties for those values were stated to be approximately a factor of 2 and it was noted the values were low considering the energy spacing of the states and the large energy difference between the $3p\ ^3P$ and the next lowest state. More recently, Tendo et al. [68] measured the branching ratio of $3p\ ^3P$ quenching to $3s\ ^3S^\circ$ with collisional partner argon and found a value of approximately 40%. Using method of equation 23, the branching ratio for $3p\ ^3P$ quenching with an arbitrary collisional partner was found to be approximately 28%, 65% and 7% to the $3p\ ^5P$, $3s\ ^3S^\circ$ and $3s\ ^5S^\circ$ states, respectively. In the absence of a more accurate method, the branching scheme as described above was used, except in the cases of $3p\ ^3P$ quenching to $3p\ ^5P$ on O_2 and N_2 collisional partners, where the results of Dagdigian et al. [3] were used. In most cases, determining the final state for collisional quenching is not crucial for spectroscopic diagnostics of atomic oxygen as it largely populates states which are not strong radiators and would otherwise be similarly populated by radiation. However, in the case of $3p\ ^3P$ quenching to $3p\ ^5P$, good estimates for branching ratios may

be crucial for some circumstances as the rate can become comparable to direct electron impact excitation from the ground state.

Electron Impact Dissociation and Dissociative Excitation.

In order to directly model the distribution of states of atomic oxygen in a discharge, it is crucial to understand electron impact dissociation and its resulting fragments. For the model in this work, it is assumed that all atomic oxygen is a result of electron collisions with $O_2(X^3\Sigma_g^-)$ and all atomic oxygen production from excited O_2 and O_3 is ignored. Though rates for direct electron impact excitation from ground state atomic oxygen typically dominate dissociation excitation rates for high lying excited states, the latter are clearly non-negligible. For example, it is well known that dissociative excitation is an important populating process in oxygen discharges, particularly for the 777.4 nm multiplet ($3p^5P \rightarrow 3s^5S^\circ$) [70].

Though dissociation of O_2 has been extensively studied [64, 71–77] by both time of flight and emission methods, the rates and cross sections currently exist in a variety of capacities. This is due to the nature of dissociation, various channels, and emission cascade contributions. For example, Cosby [74], measured the total dissociation cross section for electron impact of O_2 in vibrationally excited O_2 with $v \leq 4$. Dissociation was reasoned to be dominated by two sets of fragments, $O(^3P)+O(^3P)$ and $O(^3P)+O(^1D)$. In addition to the total dissociation cross section, Cosby gives a partial dissociation cross section for dissociation fragments above an energy threshold of 2.7 eV. Table 4 provides a summary of the dissociative excitation rates and cross sections used for this work. Dissociative excitation rates are included in the model for the first 7 states. Any dissociative excitation for higher states that results in cascading emission into the lower 7 states is already included in the dissociative excitation cross sections by the nature of those experiments.

Table 4. Dissociative excitation rates and cross sections

Configuration	Term	Threshold	$\sigma_{DE}(100\,\text{eV})$	$k^{DE}(1\,\text{eV})$	σ_{DE} Ref.
		eV	$10^{-20}\,\text{cm}^2$	cm^3s^{-1}	
$2s^2 2p^4$	^{3}P	13.5	330	2.44e-12	[74]
$2s^2 2p^4$	^{1}D	13.5	330	6.23e-14	[74]
$2s^2 2p^4$	^{1}S	16	204	6.57e-17	[72]
$2s^2 2p^3(4S^\circ)3s$	$^5S^\circ$	14.3	647	6.03e-16	[72]
$2s^2 2p^3(4S^\circ)3s$	$^3S^\circ$	14.4	293	1.64e-16	[71]
$2s^2 2p^3(4S^\circ)3p$	^{5}P	16.7	430	4.28e-17	[64]
$2s^2 2p^3(4S^\circ)3p$	^{3}P	17	200	1.97e-17	[64]

Global Loss Rates.

Due to the inclusion of dissociation and dissociative excitation, it is necessary to include a mechanism for loss of all atomic oxygen species in order to maintain a desired dissociation fraction. Ideally, rates for dominant recombination and loss mechanisms such as 3-body recombination and a wall rate with accurate rates for each excited state would be included. However, because a complete set of such rates does not appear to be available in literature, a global loss rate is included. This effective approximation is that all atomic oxygen states have the same wall and recombination rates. Each possible value of this loss rate corresponds to a resulting dissociation fraction when the model reaches equilibrium. Rather than set this global loss rate directly, a target dissociation fraction is set and the loss rate is determined numerically as the rate which leads to an equilibrium with the desired dissociation fraction. This is accomplished by allowing the model to adjust the global loss rate at each time step depending on whether the actual dissociation fraction agrees with the target dissociation fraction. For a given dissociation fraction, the model converges rapidly to a global loss rate. To ensure that this method for determining the rate does not impact the final results, it was confirmed that initializing the simulation with a fixed loss rate yields identical results to the method discussed above. Because this global loss rate balances

atomic oxygen population by dissociation, it is on the order of the dissociative excitation rates.

Finally, it is noted that this global loss rate does not significantly impact strongly radiating states and remains orders of magnitude less than the total removal rates of the 3p ^{3}P and 3p ^{5}P states. The largest value of the loss rate observed for all the calculations presented here, relative to other important removal rates (spontaneous emission and quenching) was approximately 14% and 10% of the quenching rates of the 3p ^{3}P and 3p ^{5}P states, respectively. However, this was observed at 1 mTorr where even the quenching rates are negligible. The impact of including this global loss rate is discussed further in section 4, particularly with respect to comparing the results of the collisional-radiative model to the corona models which do not include this rate.

Numerical Model.

The electron impact and dissociative excitation rates were calculated in the usual way, $k = \langle \sigma v_e \rangle$, using electron energy distribution functions generated by BOLSIG [11] and appropriate cross sections from literature. For simplicity only initial gas species (O_2 ,N_2 ,Ar) and dissociated atomic oxygen were considered for the BOLSIG EEDF calculations, though in most cases inclusion of atomic oxygen had a negligible impact on the EEDF and subsequent results, and in these cases it was excluded from EEDF calculations for simplicity. Electron impact excitation cross sections from the ground state were taken from Laher and Gilmore (1990) [7]. For electron excitation from the first 6 excited states, cross sections were taken from Barklem (2007) [18]. Cross sections from literature sources which did not include data tables were digitized from figures. A summary of the cross sections for dissociative excitation and their sources is given in Table 4. Einstein coefficients for spontaneous emission were taken from NIST [33]. The rate equation for an arbitrary level,

denoted by index j, is

$$\frac{dn_j}{dt} = n_e \sum_{i<j} n_i k_e^{ij} + n_e \sum_{i>j} n_i k_{ed}^{ij} + n_e n_{O_2} k_{de}^{j} + \sum_{i>j} n_i k_q^{ij} + \sum_{i>j} n_i A_{ij} - n_e \sum_{f>j} n_j k_e^{jf} - n_e \sum_{f<j} n_j k_{ed}^{jf} - \sum_{f<j} n_j k_q^{jf} - \sum_{f<j} n_j A_{jf} - n_j R, \tag{24}$$

where rate R is the global removal or loss rate, as discussed in section 2.3. Equation 24 represents a set of j coupled first order linear differential equations. The steady state solution is found by using a numerical ordinary differential equation (ODE) solver, with initial conditions $[n_e, n_0, n_{0_2}, T_e]$. The ODE solution was chosen over the typically more desirable direct eigenvalue matrix methods due to poorly conditioned rate matrices. However, both methods were shown to produce the same steady state results independent of reasonable choices for ODE initial conditions. The ODE algorithm used was a python implementation of the LSODA ODE library, which uses a backward differentiation formula (BDF) algorithm for stiff systems.

Gas densities used for initial conditions and for calculating quenching rates are calculated based on fractional concentrations, dissociation fraction (defined here as the fraction of reagent which has been dissociated), and using the ideal gas law at the appropriate pressure and assuming a gas temperature of 300 K. If the temperature dependence of the quenching rates is ignored, which may be reasonable at low pressures, the results here can be extrapolated to higher temperatures by adjusting the indicated pressure appropriately. For the conditions studied here, gas temperature was not found to be an important input parameter for the BOLSIG EEDF calculations, though a value of 300 K was taken.

3.2 Effective Cascade Cross Section

In an effort to simplify the results of this model for use in basic diagnostic techniques along with recommended direct electron excitation cross sections, the total effective cascade cross section was calculated. In the case of Maxwellian EEDFs, a temperature dependent effective cascade rate can be used. However, for non-Maxwellian EEDFs, such as those generated by BOLSIG [11] or LoKI-B [12], fits to standard temperature dependent rate coefficients had significant residuals. Thus the effective cascade cross section should be used to account for cascade in non-Maxwellian cases. If the mechanisms of highly $(j > 7)$ excited states are limited to direct electron impact excitation and spontaneous emission, the steady state density is

$$n_j = \frac{n_e n_0 < \sigma_{0j} v_e > + \sum_{i>j} n_i A_{ij}}{\sum_{f<j} A_{jf}}. \tag{25}$$

The total cascade into state k is

$$C_k = \sum_{j>k} A_{jk} n_j = \sum_{j>k} A_{jk} \frac{n_e n_0 < \sigma_{0j} v_e > + C_j}{\sum_{f<j} A_{jf}} = n_e n_0 < \sigma^{(1)}_{eff} v_e > + \sum_{j>k} \frac{A_{jk} C_j}{\sum_{f<j} A_{jf}}, \tag{26}$$

where

$$\sigma^{(1)}_{eff} = \sum_{j>k} \frac{A_{jk} \sigma_{0j}}{\sum_{f<j} A_{jf}} \tag{27}$$

is the first order effective cascade cross section, as it does not consider cascade for any states beyond state k. However, the total effective cascade cross section can be iteratively determined using the recursive nature of equation 26, beginning with a highly excited state for which it can be assumed that the cascade contribution is negligible. Effective total cascade cross sections calculated in this way, using 96 states of oxygen, for the 3p ^{3}P and 3p ^{5}P states are shown in Figure 3.

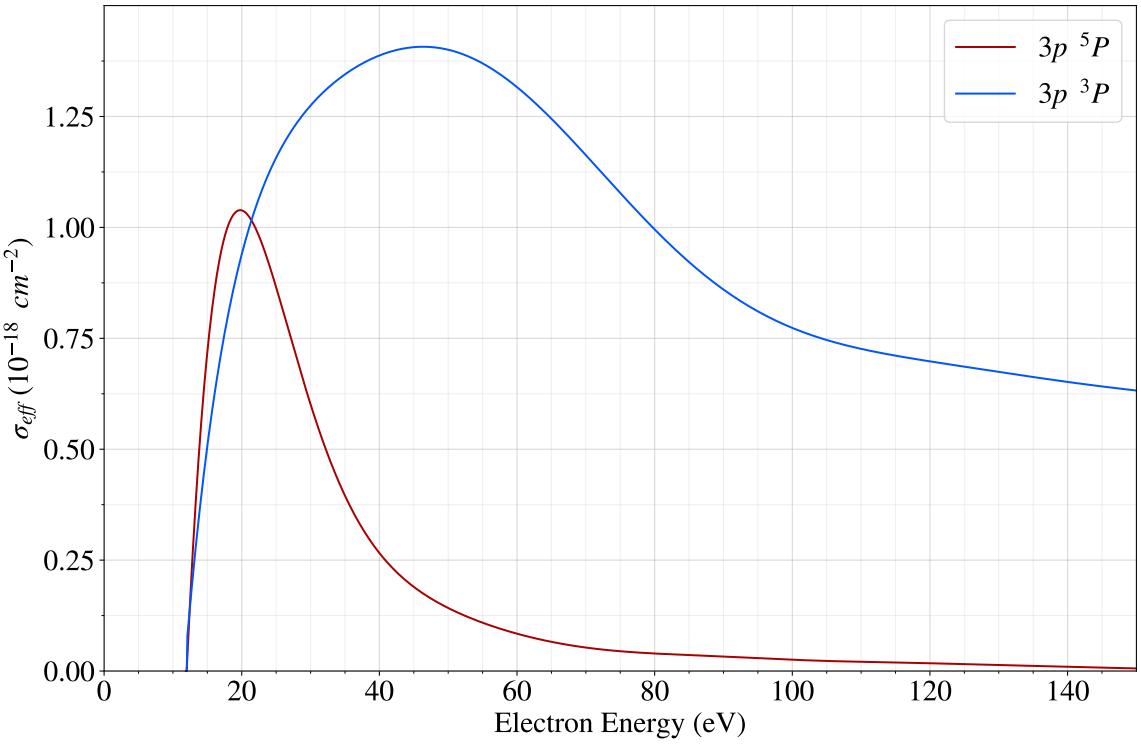

Figure 3. Effective Cascade cross sections for the 3p ^{3}P **and** 3p ^{5}P **states as calculated for 96 excited states of oxygen.**

3.3 Results

Unless stated otherwise, the following results were calculated for an electron density of 10^{10} cm^{-3}. A gas temperature of 300 K is assumed for all calculations. In all cases BOLSIG [11] is used to generate the EEDF for a variety of values for reduced electric field, E/N, and the effective electron temperature is taken to be 2/3 the mean electron energy. Bulk gas species considered for BOLSIG calculations are 98 % O_2, 2% Ar for figure 5 and 80% N_2, 20% O_2 in all other figures. In most cases the impact of dissociation fragments and other species on the EEDFs are assumed to be negligible. As part of this work, inclusion of the appropriate amount of atomic oxygen for a given dissociation fraction in the BOLSIG EEDF calculations was investigated. For the case of the synthetic air mixture, the impact on all results was negligible. In the case of the oxygen argon mixture, the fractional

concentration of atomic oxygen did modify the resulting EEDFs in a manner significant enough to impact the line ratio results, particularly at low temperatures (< 2 eV) and high dissociation fractions (10%). For this reason, both the results for considering only bulk gas species (O_2/Ar) and the results which include atomic oxygen (O_2/Ar/O) are included in calculation of EEDFs, in the case of the oxygen argon mixture. For all synthetic air results present here, only the bulk gas species (N_2/O_2) are used in BOLSIG EEDF calculations. Quenching partners considered for all results include the appropriate bulk gas species (N_2/O_2 or O_2/Ar), dissociation fragments O and N, where nitrogen is assumed to have the same dissociation fraction as oxygen, as well as O_3 and $O_2(a^1\Delta_g)$ each at 5% the concentration of O_2. In general our results were not sensitive to the concentrations of $O_2(a^1\Delta_g)$, O_3, and N. This is because only the ^{1}S and ^{1}D have non-zero quenching rates with these species for this work, and the ^{1}S and ^{1}D have weak electron excitation cross sections to the 3p ^{3}P state and a null electron excitation cross section to the 3p ^{5}P state.

Figure 4 shows the steady state fractional concentration of the first 6 excited states for a synthetic air mixture $(80\%\ N_2,\ 20\%\ O_2)$, an effective electron temperature of 3 eV, and a dissociation fraction of 10%. The metastable ^{1}D and ^{1}S states and the 3s ^{5}S$^\circ$ state, all with long radiative lifetimes, have considerable concentrations at low pressures and decrease at higher pressures due to collisions with heavy neutral particles. The remainder of the states in the active region, 3s ^{3}S$^\circ$, 3p ^{5}P and 3p ^{3}P, have concentrations which remain relatively constant with pressure as short radiative lifetimes dominate until collisional de-excitation becomes comparable. For the 3s ^{3}S$^\circ$ state, this occurs at approximately 10 Torr while in the 3p ^{5}P and 3p ^{3}P collisional de-excitation or quenching becomes non-negligible near approximately 0.1 Torr. Note that after 0.1 Torr, the increasingly shorter lifetime of the 3p ^{5}P and 3p ^{3}P states leads to an increase of rates which populate the lower energy 3s ^{5}S$^\circ$ and 3s ^{3}S$^\circ$ states, which accounts for the inflection of the 3s ^{5}S$^\circ$ concentration at high pressures and the delayed decline, with respect to pressure, in concentration of the 3s ^{3}S$^\circ$

state.

The validity of the extended corona 777 nm/844 nm line ratio model, as given in equation 17, most strongly depends on operating pressure and dominant gas species used to calculate the electron energy distribution function. Two sets of results are presented; one for the case of an oxygen plasma with trace amounts of argon (2%) and one for the case of synthetic air $(79\%\ N_2,\ 21\%\ O_2)$. The expected 777 nm/ 844 nm line ratio was calculated using 3 different methods: (1) using the 96 level collisional radiative model as described in section 2, (2) the basic model often used in literature and given by equation 1 and (3) the basic model in equation 1 with the inclusion of a cascade emission rate calculated using the cross sections found in section 3.

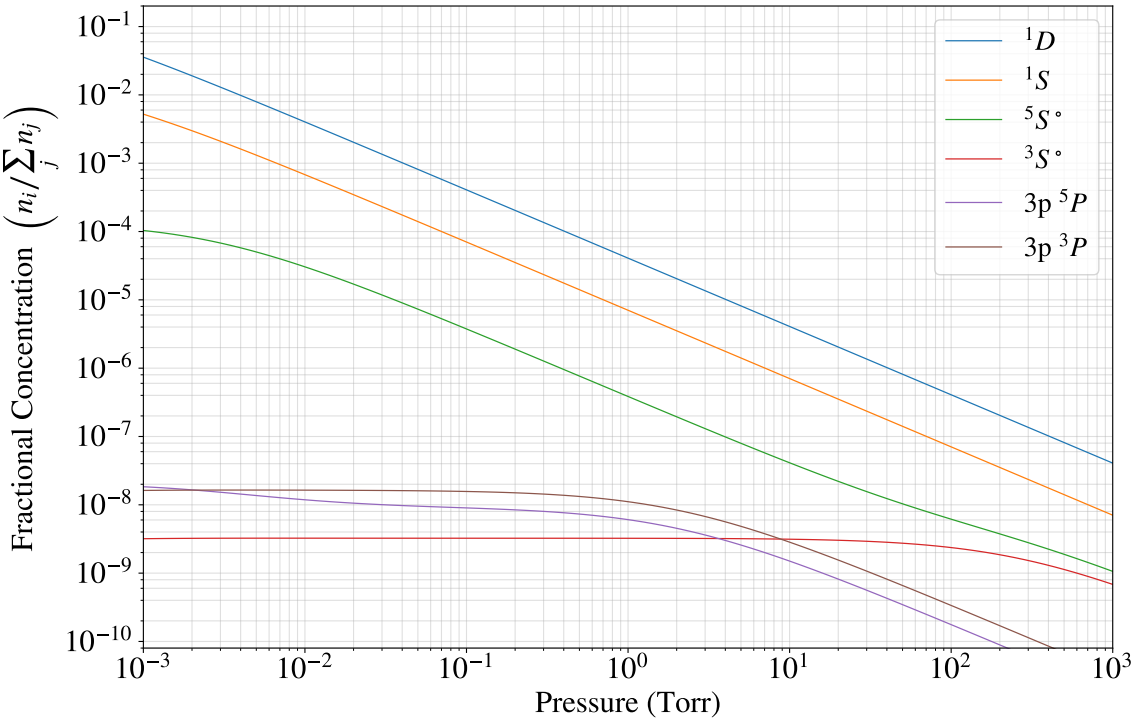

Figure 4. Steady state fractional concentrations for the first 6 excited states as calculated by the 96 collisional-radiative model.

Figure 5 illustrates the results for the oxygen/argon mixture for operating pressures of 760, 1, and 0.001 Torr and at both 10% and 1% dissociation. In each case there is a large discrepancy between the collisional-radiative model and the basic models, particularly at low temperatures. In order to determine the mechanisms underlying this discrepancy, a simple rate sensitively analysis was employed. Each element of the rate matrix was independently (all other rates remained constant while one rate was interrogated) and iteratively adjusted over a range of approximately $\pm 20\%$, while the resulting impact on the line ratio was observed. This way a new matrix was constructed, with the shape of the rate matrix, containing the derivatives of the line ratio with respect to each individual rate. Based on this rate sensitivity analysis, it was found that at low temperatures the line ratio as calculated by the collisional-radiative model is strongly influenced by electron impact excitation from the metastables. At higher temperatures, the discrepancy is a result of both cascade emission from excited states and collisional quenching of the 3p ^{3}P state to the 3p ^{5}P state.

The largest discrepancy between the basic model and the collisional radiative model was observed at low pressures, where the strong influence of metastables exists at all temperatures.

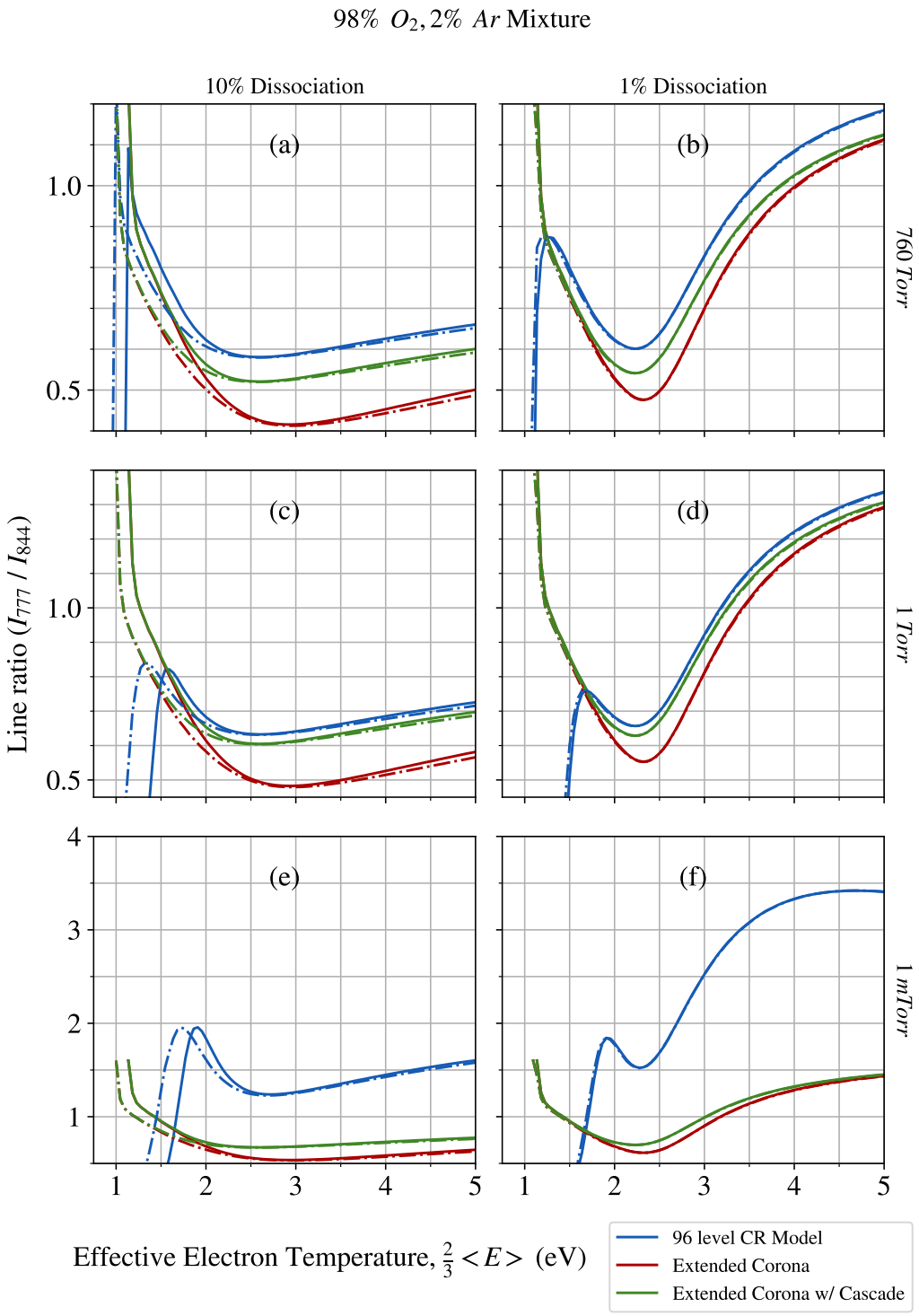

Figure 5. Calculated line ratios using the collisional radiative model and basic models for the 98 % Oxygen 2% Argon mixture for (a) 760 Torr and 10% dissociation fraction, (b) 760 Torr and 1% dissociation fraction, (c) 1 Torr and 10% dissociation fraction, (d) 1 Torr and 1% dissociation fraction, (e) 1 mTorr and 10% dissociation fraction, (f) 1 mTorr and 1% dissociation fraction. Dashed lines were calculated using BOLSIG EEDFs which considered bulk species and atomic oxygen at the labeled dissociation fraction. Solid lines only considered bulk species for EEDF calculations.

Figure 6 shows the results for synthetic air, where the inclusion of nitrogen as the dominant species drastically alters the EEDF and the subsequent dependence of the calculated line ratio on the effective electron temperature. In the case of synthetic air, excitation from metastable states accounts for discrepancies only at low pressures, figure 6 (e) and (f). At higher pressures, 1 Torr and 760 Torr, cascade emission and collisional quenching of the 3p ^{3}P state to the 3p ^{5}P state account for the differences between the basic model and the collisional radiative model. Another disagreement between the basic corona models and the collisional-radiative model is the strong electron density dependence the line ratio has at low pressures. Figure 7 shows the 777 nm/844 nm line ratio as a function of electron density for the case of synthetic air, an effective electron temperature of 3 eV and a dissociation fraction of 5%. The ratio was calculated for four different pressures. The results show that the density dependence can only be ignored for high pressures or for low electron densities. The sensitivity analysis highlighted that the calculated line ratio at low pressures and high densities is highly sensitive to the kinetics of the 3s ^{5}S$^\circ$ state. The kinetic situation for the 3s ^{5}S$^\circ$ state in these conditions is complex and strongly depends on nearly all of the first 7 states in the model. It should be noted again that the line ratios calculated in Figures 5 and 6 used an electron density of 10^{10} cm^{-3}. This value was chosen as it is a reasonable average for laboratory plasmas. However, the agreement between the different models illustrated in 5 and 6 would be diminished for electron densities larger than 10^{10} cm^{-3} for the 1 Torr and 1 mTorr cases. For densities lower than 10^{10} cm^{-3} the line ratios calculated for both the 760 Torr and 1 Torr cases would be nearly unchanged, while the 1 mTorr case would see significantly better agreement.

Among the possibilities for additional mechanisms underlying the discrepancies presented in figures 5 and 6 is the global loss rate which is included in the collisional-radiative model and ignored in the corona models. To investigate this further the line ratios were calculated for the parameters in figures 5 and 6 using the corona model as in equation 17,

with the addition of the same global loss rate used by the collisional-radiative model in the denominator. The error of this line ratio, relative to the line ratio calculated using equation 17 was at most 0.0003%. Therefore it is concluded that the discrepancies incurred by the global loss rate are negligible compared to those discovered by the rate sensitivity analysis and discussed above.

Finally, for reference, Figure 8 provides the 777 nm/844 nm line ratio as calculated by the 96 level collisional-radiative model as a function of dissociation fraction and electron temperature for 9 separate pairs of electron density and pressure. Figure 8 should provide relatively accurate results outside of provided values for electron density particular for lower densities at medium to high pressures.

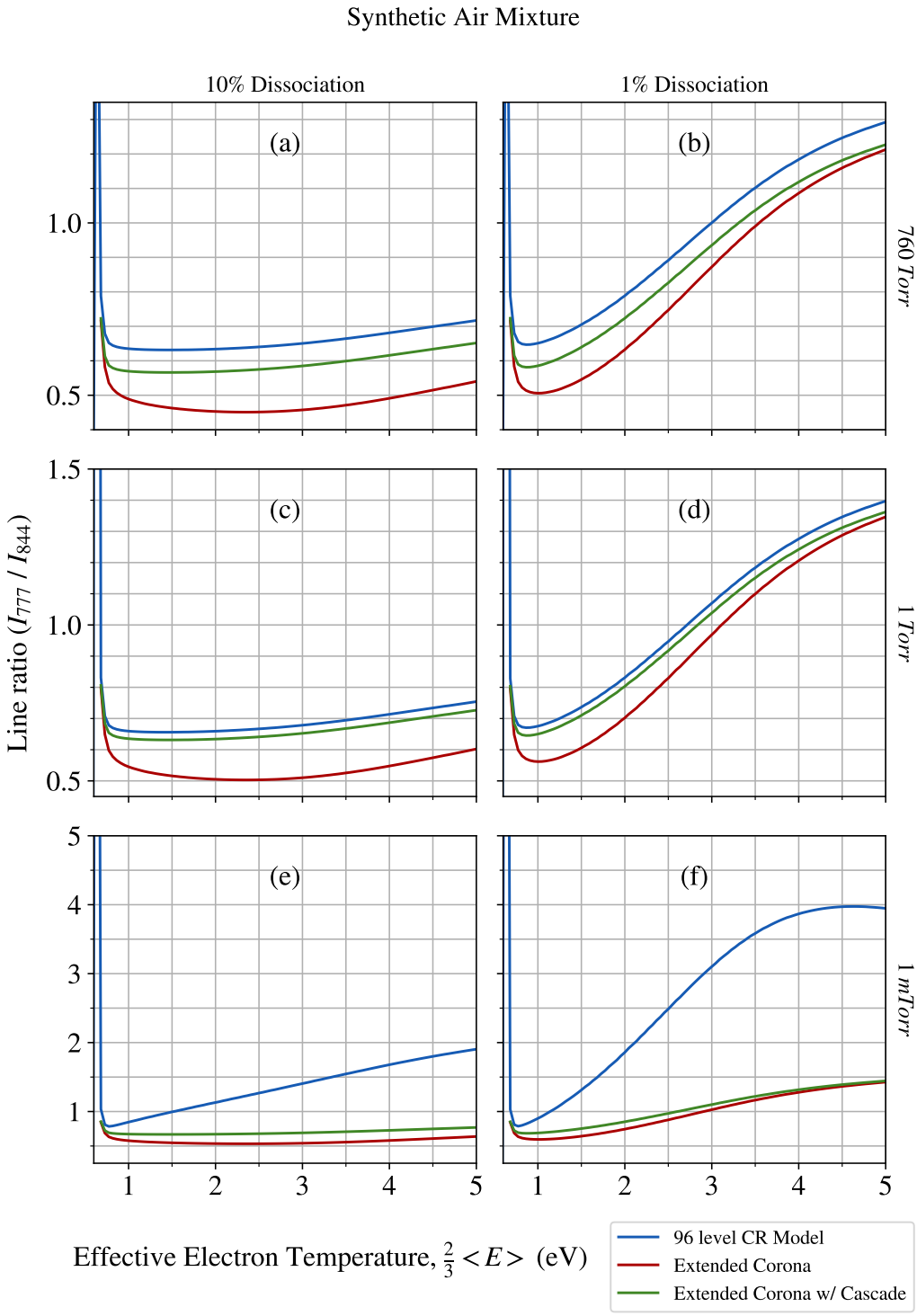

Figure 6. Calculated line ratios using the collisional radiative model and basic models for the synthetic air mixture for (a) 760 Torr and 10% dissociation fraction, (b) 760 Torr and 1% dissociation fraction, (c) 1 Torr and 10% dissociation fraction, (d) 1 Torr and 1% dissociation fraction, (e) 1 mTorr and 10% dissociation fraction, (f) 1 mTorr and 1% dissociation fraction.

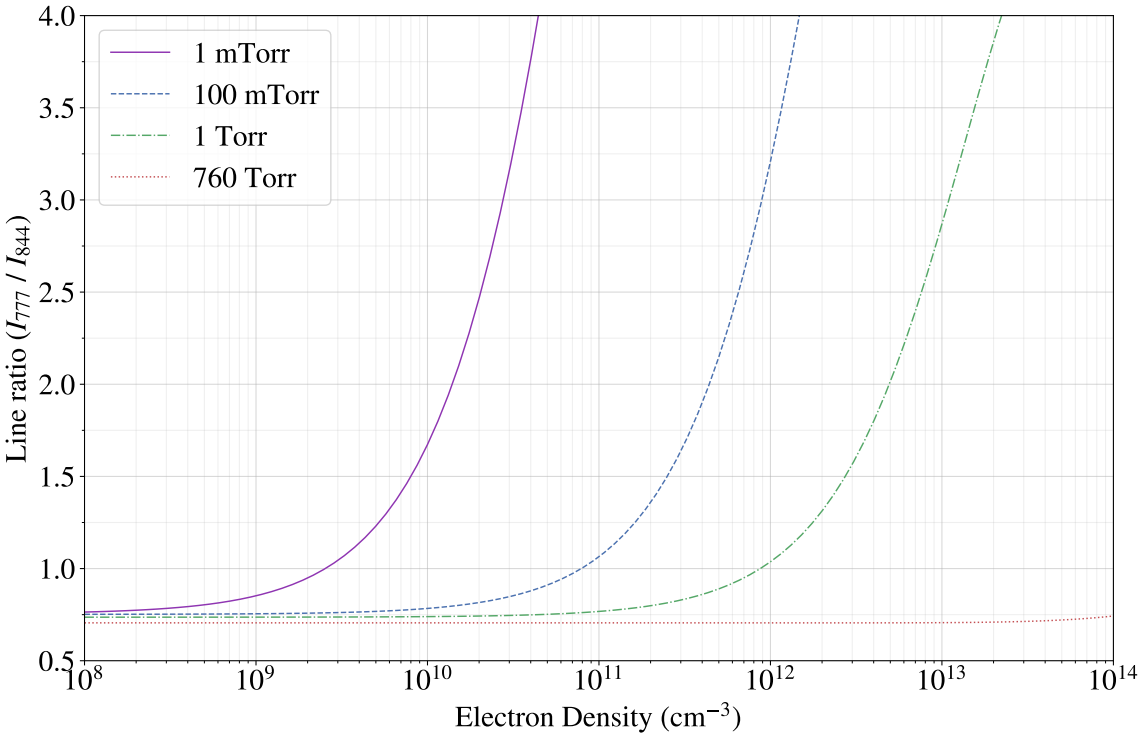

Figure 7. Calculated line ratios using the collisional radiative model as a function of electron density for 1 mTorr, 100 mTorr, 1 Torr and 760 Torr in synthetic air. Ratios were calculated at an effective electron temperature of 3 eV and a dissociation fraction of 5%

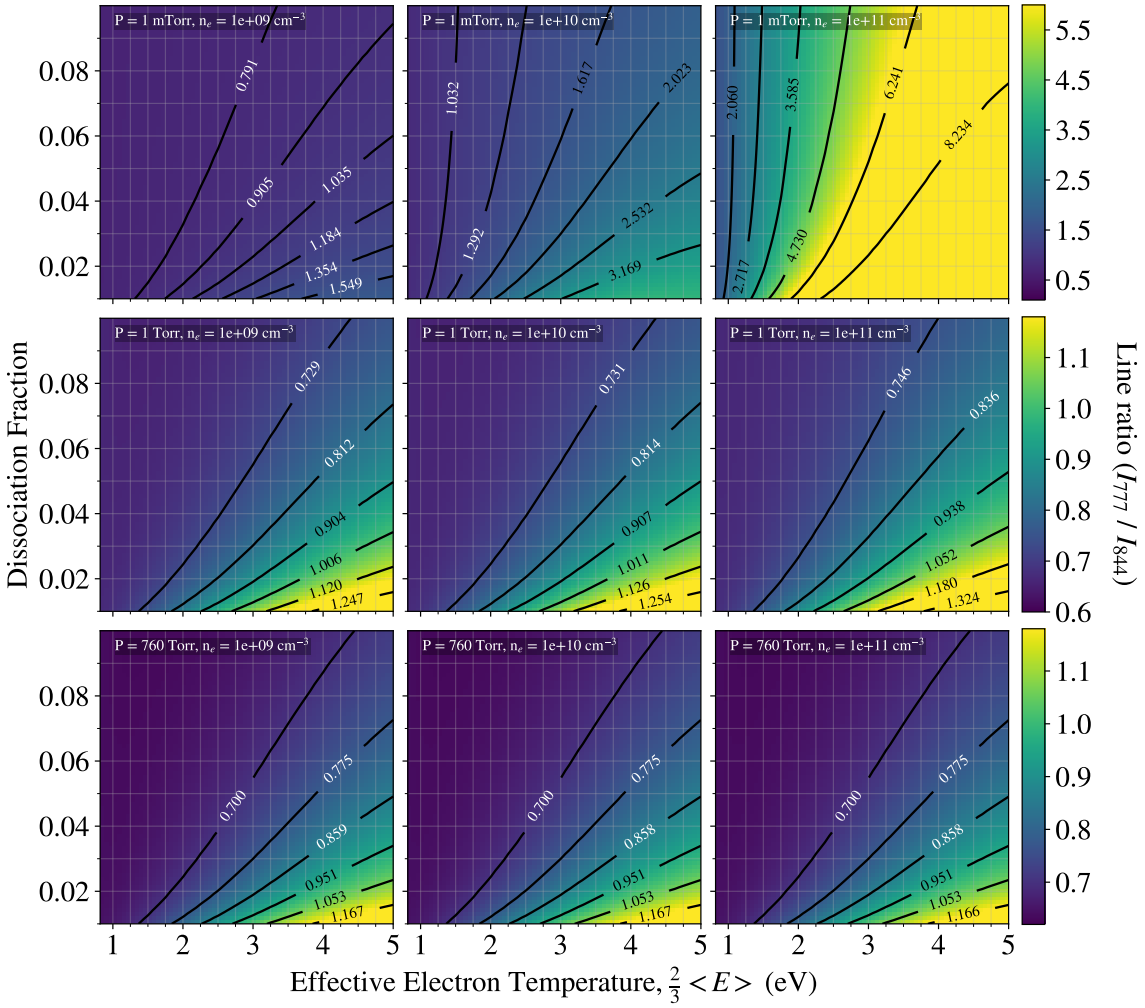

Figure 8. Calculated line ratios using the collisional radiative model as a function of dissociation fraction and effective electron temperature for synthetic air at a range of electron densities and pressures and at a gas temperature of 300 K.

3.4 Discussion

In all cases, the cascade rate using the effective cascade cross sections calculated in section 3 increased the agreement of the basic model with the collisional radiative model without drastically complicating calculation of the line ratio. Table 5 gives the mean error of the basic corona models with respect to the collisional-radiative model for synthetic air over the 1-5 eV effective electron temperature range. In some cases, such as at 1 Torr for both gas mixtures (Figure 5 c and d, Figure 6 c and d), the inclusion of cascade emission

provides good agreement between the corona based model and the 96 level collisional radiative model, with an average error of less than 4% for 1 Torr in synthetic air. In general, the basic models become poor approximations at low pressures where slow collisional relaxation rates of ^{1}D, ^{1}S, and 3s ^{5}S$^\circ$ states lead to increased densities in those states and subsequent step-wise electron impact excitation to the 3p ^{3}P and 3p ^{5}P states. Though even at low pressures the calculated line ratio has a weak dependence on ^{1}D and ^{1}S densities, the electron impact excitation rates from the 3s ^{5}S$^\circ$ state are found to strongly influence the calculated line ratio. This is because the rate for excitation from 3s ^{5}S$^\circ$ to 3p ^{5}P is nearly 20 times that of 3s ^{5}S$^\circ$ to 3p ^{3}P at 1 eV. At low pressures, the densities of the 3s ^{5}S$^\circ$ state are significantly high such that the excitation rate for the 3p ^{5}P state from the 3s ^{5}S$^\circ$ state is a significant fraction of the electron excitation from the ground state. Additionally, because the kinetics of the 3s ^{5}S$^\circ$ state are strongly connected by electron excitation to the 3s ^{3}S$^\circ$, 3p ^{5}P, and 3p ^{3}P states and strongly populated by emission from the 3p ^{5}P state, its steady state density depends on nearly all of the first 7 states of atomic oxygen. This complex reliance of the spectra on the 3s ^{5}S$^\circ$ state provides the strong dependence of the 777 nm/844 nm line ratio on electron density at low pressures and high electron densities. Figure 9 shows the magnitude of the steady state rates to and from the 3s ^{5}S$^\circ$ state as calculated using the collisional radiative model at low pressure (1 mTorr) and high electron density (10^{12} cm^{-3}). This shows the importance of the 3s ^{5}S$^\circ$ state on the 777 nm/844 nm line ratio as well as the behavior that leads to a strong dependence on electron density as shown in Figure 7.

Besides cascade emission and metastable excitation, the rate of collisional relaxation with heavy particles from the 3p ^{3}P to the 3p ^{5}P has been identified as an important process at high pressure. Because of this, accurate quenching rates for the 3p ^{3}P as well as a branching ratio to the 3p ^{5}P must be included in any model to accurately predict the 777 nm/844 nm line ratio at high pressure when heavy particles are present. In compari-

son to the collisional-radiative model, not accounting for 3p ^{5}P production by this method accounts for approximately 7-10% average error in line ratio at atmospheric pressure.

Table 5. Mean error of extended corona models as compared to the 96 level CR model for synthetic air

Conditions		Mean Error	
Pressure (Torr)	Dissociation Fraction	Ext. Corona	Ext. Corona w/ Casc.
0.001	0.10	57.9%	47.6%
0.001	0.01	61.6%	57.9%
1.0	0.10	22.8%	3.78%
1.0	0.01	10.3%	3.01%
760	0.10	27.7%	9.92%
760	0.01	13.9%	6.96%

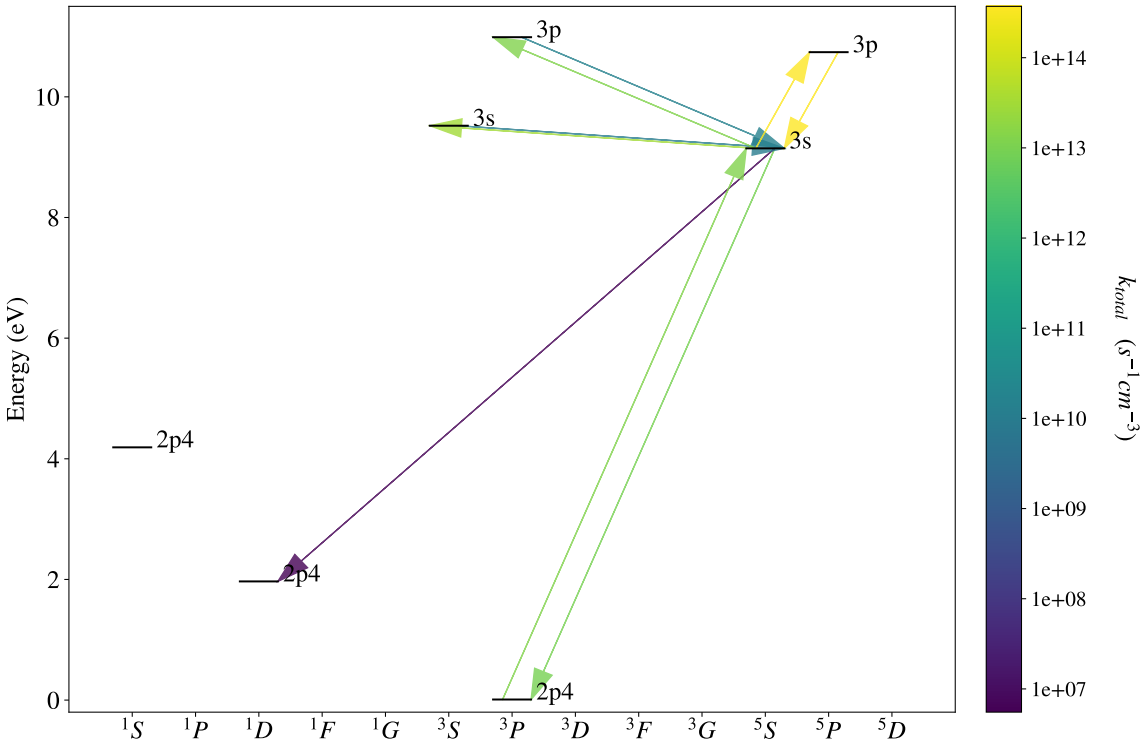

Figure 9. Energy level diagram of the first 7 levels of atomic oxygen showing the steady state total rates to and from the 3s ^{5}S° **state.**

IV. Experimental Combined Actinometry of a stationary discharge

Given the highly reactive nature of atomic oxygen and its importance in plasma chemistry processes in air plasmas, determination of its absolute density has been an important diagnostic. Argon actinometry seems to have emerged as the preferred technique for determination of absolute atomic oxygen density or dissociation fraction in most cases, likely due to its relatively simple experimental requirements when compared to more robust methods such as laser absorption spectroscopy. The argon actinometry approach is accomplished by adding to a discharge trace amounts of argon, referred to as the 'actinometer', of which the concentration is known. Because emission intensities for lines which are dominantly populated by electron excitation from the ground state species are proportional to the ground state density, the ratio of an argon actinometer line to an appropriate oxygen line is proportional to the ratio of ground state densities of argon and oxygen. Since the concentration of argon is known and the ground state is the dominant state for both species, atomic oxygen concentration can be determined [50, 70, 78–80]. The general technique makes use of one of two strong infrared oxygen triplets (777 nm and 844 nm) and was first reported by Walkup et al. in 1986 [70] , validated for use in low energy N_2/O_2 discharges by Granier et al. in 1994 [78] and improved by Katsch et al. in 2000 [79] to include dissociative excitation, which allowed this oxygen actinometry technique to be applied in higher power laboratory plasmas with a significant fraction of electrons beyond the dissociative excitation threshold ($\approx 20eV$). The latter work was made possible by cross sections measured by Schulmann et al. [64]. Additionally, Katsch et al. observed a significant discrepancy in oxygen densities measured when the actinometer line is compared to the 844 nm multiplet ($3p^3P \rightarrow 3s^3S^\circ$) , and those determined using the 777.4 nm multiplet ($3p^5P \rightarrow 3s^5S^\circ$) , with the former having better agreement with the more trustworthy laser spectroscopy method. The authors proposed this discrepancy was due to dissociative excitation from the common metastable $O_2(^1\Delta)$ state. In the years since the development of these techniques,

many authors have used both the 777 nm and 844 nm multiplets for actinometry and similar measurements with positive results in a variety of laboratory discharges [50, 80–84]. Still others have seen significant disagreement between the two actinometry ratios [49, 85–88]. It seems the general consensus is that both techniques can provide acceptable estimates of absolute atomic oxygen density but that the 844 nm line is typically more reliable.

In this chapter dissociation fractions are compared as measured using both 844 nm and 777 nm actinometry, as well as actinometry using the relatively weaker 616 nm oxygen line from the 4d ^{5}D$^\circ \rightarrow$ 3p ^{5}P transition, in a medium pressure N_2-O_2 microwave discharge. The reduced electric field or effective electron temperature ($2/3$ mean electron energy) and subsequent electron energy distribution functions (EEDF) are found using the N_2/N_2^+ line ratio method [40, 44], as well as methods which use the actinometer and the oxygen lines. Similar to many previous results [85–88], the results here show strong disagreement between dissociation fractions predicted by the 844 nm multiplet ($3p^3P \rightarrow 3s^3S^\circ$) and those predicted using the 777.4 nm multiplet ($3p^5P \rightarrow 3s^5S^\circ$) . To potentially resolve discrepancy, it is proposed here that the discrepancies when observed are due to the relatively high excitation rate of the 777.4 nm multiplet ($3p^5P \rightarrow 3s^5S^\circ$) from the metastable 3s ^{5}S$^\circ$ state, as evidenced by the cross sections determined by Barklem [18]. Given this assumption, which is supported by our previous work [89] and a detailed collisional-radiative model, the absolute 3s ^{5}S$^\circ$ density and electron density can be deduced using a combined actinometry approach. This 3s ^{5}S$^\circ$ density as measured experimentally is presented and corresponding electron densities predicted by a collisional-radiative model and a basic analytic model are compared with values in literature for similar discharges. Results regarding the 616 nm actinometry are inconclusive due to unknown quenching and metastable excitation rates, though the line seems promising for future work. Additionally, its inclusion along with the other two oxygen lines could be used to remove an additional unknown parameter, thus removing the requirement of the argon actinometer. As a result of this paper it is

suggested that the 777 nm actinometry technique may be unreliable if metastable excitation is ignored and that a combined actinometry technique, which uses both common oxygen lines along with the N_2/N_2^+ line ratio method, may be applicable which can simultaneously determine the effective electron temperature, dissociation fraction, absolute 3s $^5S^\circ$ density and electron density. Before describing our experimental results, it is necessary to detail the many kinetic models used in this work. Sections 4.1 and 4.2 below describe the kinetic schemes which support the experimental diagnostics.

4.1 Line Intensity Models

The actinometry approach and similar optical emission spectroscopy (OES) techniques rely on the estimation of line intensities using simple analytic models where the list of important populating and de-populating processes has been greatly distilled. This work makes use of four atomic lines and two diatomic nitrogen systems, all of which are dominantly populated by electron collisional processes and primarily de-populated by optical emission. A summary of the optical transitions and excitation mechanisms considered are given in table 6. Populating mechanisms include direct impact electron excitation from the ground state, dissociative excitation, cascade emission and metastable excitation. Collisional de-excitation is considered for all oxygen and argon states as well as for both excited molecular nitrogen states (section 4.1), all references and relevant rates for collisional de-excitation are given in table 7.

Argon.

The argon 750.4 nm line $\left(4p'^{\,2}\left[{}^1/_2\right]_0 \rightarrow 4s'^{\,2}\left[{}^1/_2\right]_1^\circ\right)$ is generally considered to follow the basic corona model [79], in which population only proceeds through direct electron excitation from ground state argon and loss occurs only by spontaneous emission. In the corona approximation, the line intensity of the 750 nm line is

$$I_{\mathrm{Ar}750} = K(\lambda_{750}) n_{Ar} n_e k_e^{4p'} A_{750} \tau_{4p'}, \tag{28}$$

where $K(\lambda)$ is the relative instrument calibration coefficient at the appropriate wavelength, n_e is the electron density, n_{Ar} is the density of the argon ground state, A is the Einstein A coefficient for spontaneous emission, τ is the effective lifetime and k_e is the electron excitation rate from the ground state. In the absence of collisional quenching, the lifetime is simply $\tau = 1/\sum_{f<i} A_{if}$. If quenching is non-negligible, the effective lifetime is calculated as

$$\tau = \frac{1}{\sum_{f<i} A_{if} + \sum_m q_m n_m}, \tag{29}$$

where q_m and n_m is the rate coefficient and density, respectively, of quencher m, and the sum is over all relevant species. Finally, a coefficient is defined which contains detectivity and optical branching at λ as $P_\lambda = K(\lambda_{ik}) A_{ik} \tau_i$ [40], with radiative lifetimes of upper states and Einstein A coefficients are given in table 1. The choice of electron excitation cross section for the Ar $\left(4p'^{\,2}\left[{}^1/_2\right]_0\right)$ state can significantly change the actinometry results, as discussed in Pagnon et al. [94]. For example, the cross sections from Chilton et al. [90] have different shapes and higher maximum values than the cross section given in Katsch et al. [79]. For this work the cross section given by Chilton et al. [90] is used, as it includes more supporting data, such as comparisons with other results. In all cases in this work, the excitation rates are calculated using EEDFs (f_e) generated by the well-known BOLSIG+ Boltzmann solver [11]. The primary input parameter for the BOLSIG EEDF calculations is the reduced electric field (E/N). From the resulting EEDF, the effective electron temperature ($2/3$ mean electron energy) is calculated and used in this work as a primary output and label for each EEDF. The cross sections used as BOLSIG inputs were generated from the LXcat database and contained cross sections for N_2, O_2, Ar and O at ratios consistent with

experimental parameters and approximate dissociation fraction [95–99].

Oxygen.

For reference, a partial energy level diagram for atomic oxygen is given in figure 10. The general approach for oxygen is similar to the corona model as described above with the addition of dissociative excitation rate as proposed by Katsch et al. [79] and an electron impact induced cascade emission rate derived from our previous work [89] (which uses the direct electron excitation cross sections from Laher and Gilmore [7]). These Cascade excitation cross sections for states relevant to this work are given in table 9. For the remainder of this dissertation this kinetic situation is referred to as the extended corona model. The line intensity for each of the oxygen lines is then

$$I_{ik} = P_\lambda \left[n_O n_e (k_e + k_{csc}) + n_{O_2} n_e k_{de} \right]. \tag{30}$$

Quenching of atomic oxygen states has been relatively well studied with O(3p ^{3}P) known from multiple works [2, 69] for all collisional partners relevant to this work (N_2, O_2, Ar). It should be noted that this is another significant reason that actinometry using the 844 nm line is preferable, particularly in air plasmas. Collisional relaxation of atomic oxygen metastables has also been investigated, with rates having been measured for the first three excited states (^{1}D, ^{1}S, 3s ^{5}S$^\circ$) on a wide variety of collisional partners [62, 67, 68]. However, no studies appear to exist for quenching of the 4d ^{5}D$^\circ \rightarrow$ 3p ^{5}P line and quenching rates for the 3p ^{5}P state are only known for molecular oxygen as a collisional partner. At a working pressure of 0.75 Torr the collisional branching for the O(3p ^{3}P) state in air is approximately 16% at 300K and 28% if scaled to a gas temperature of 900 K. Clearly these rates are non-negligible, thus reasonable values are assumed for the unknown rates. As a best guess, the quenching rate on N_2 for the 3p ^{5}P state is assumed to be the same as the 3p ^{3}P state, as in previous work [63, 89]. To account for uncertainties associated

with this assumption, the lifetimes of the 3p ^{5}P state are calculated with quenching rates on N_2 ranging from zero to the quenching rate of 3p ^{5}P for molecular oxygen collisional partners, which is the highest value of all the quenching rates relevant to this work, at a value of $1.1 \times 10^{-9} cm^3 s^{-1}$. This range of potential quenching rates are incorporated into the general experimental uncertainty for dissociation fractions measured using the 777 nm line. Because quenching rates for oxygen species on argon are typically small and argon constitutes a relatively small partial pressure for this work, uncertainty regarding this rate is considered negligible and it is assumed that rate is the same as that of the 3p ^{3}P state. For the 616 nm line originating from the 4d ^{5}D$^\circ$ state, as there are no known rates, two possible situations are tested: one in which the quenching rates are negligible and one in which they are assumed equal to the 3p ^{3}P values. Effective lifetimes for all states in this work are calculated as described for argon in section 4.1 above, using the quenching coefficients in table 7 and scaled to the gas temperature approximated by the N_2 SPS OES method described in section 4.4 by a factor of $\sqrt{T/T_m}$, where T is the gas temperature assumed here and T_m is the temperature at which the quenching rate was measured. This factor arises from the assumption that the quenching rates carry a gas-kinetic linear dependence on mean molecular velocity ($k \approx \langle v \rangle \sigma$) [100].

If in addition to the mechanisms in equation 30, the 3p ^{5}P state is also produced by excitation from the 3s ^{5}S$^\circ$ state, the intensity of the 777 nm line can be expressed as

$$I_{777} = P_{777} \left[n_O n_e (k_e + k_{csc}) + n_{O_2} n_e k_{de} + n_{^5S} n_e k_{em} \right]. \tag{31}$$

Thus far there are 4 equations for line intensities (750 nm Ar, 615 nm O, 777 nm O and 844 nm O) and three line ratios can be written, each having the 750 nm argon line in the numerator. The three actinometry ratios are then

$$\frac{I_{750(Ar)}}{I_{616(O)}} = \frac{P_{750}}{P_{616}}\left[\frac{n_{Ar}k_e^{4p'}}{n_O(k_e^{5D}+k_{csc}^{5D})+n_{O_2}k_{de}^{5D}}\right], \tag{32}$$

$$\frac{I_{750(Ar)}}{I_{844(O)}} = \frac{P_{750}}{P_{844}}\left[\frac{n_{Ar}k_e^{4p'}}{n_O(k_e^{3P}+k_{csc}^{3P})+n_{O_2}k_{de}^{3P}}\right], \tag{33}$$

$$\frac{I_{750(Ar)}}{I_{777(O)}} = \frac{P_{750}}{P_{777}}\left[\frac{n_{Ar}k_e^{4p'}}{n_O(k_e^{5P}+k_{csc}^{5P})+n_{O_2}k_{de}^{5P}+n_{5S}k_{em}^{5P}}\right]. \tag{34}$$

In the case of equations 32 and 33, one can solve for n_O and get the argon actinometry relations for both the 616 nm and 844 nm lines

$$n_O^{616}(f_e) = \frac{1}{(k_e^{5D}+k_{csc}^{5D})}\left[\frac{I_{616(O)}}{I_{750(Ar)}}\frac{P_{750}}{P_{616}}n_{Ar}k_e^{4p'} - n_{O_2}k_{de}^{5D}\right], \tag{35}$$

$$n_O^{844}(f_e) = \frac{1}{(k_e^{3P}+k_{csc}^{3P})}\left[\frac{I_{844(O)}}{I_{750(Ar)}}\frac{P_{750}}{P_{844}}n_{Ar}k_e^{4p'} - n_{O_2}k_{de}^{3P}\right]. \tag{36}$$

A similar solution for oxygen density, given by the extended corona model, is typically written for the 777 nm line as well, in which metastable excitation is ignored. Both cases for the 777 nm solution, with and without metastable excitation, are examined in sections 4.4 and 4.5. Any two actinometry ratios following the extended corona model, as in equations 35 and 36 (or similarly equation 37 for a given metastable density), provide two equations and two effective unknowns: atomic oxygen density (or equivalently dissociation fraction) and electron energy distribution function. A solution for both unknowns can be arrived at for a given set of experimental ratios. This is accomplished by calculating BOLSIG EEDFs (f_e) for a wide range of feasible reduced electric fields and selecting the f_e (and corresponding effective electron temperature) which minimizes the difference between oxygen densities predicted by each line ratio. With both f_e and n_O known, the density of the 3s ^{5}S$^\circ$ metastable state in equation 34 can be solved for, as shown below:

$$n_{5S}(n_O, f_e) = \frac{1}{k_{em}^{5P}} \left[\frac{I_{777(O)}}{I_{750(Ar)}} \frac{P_{750}}{P_{777}} n_{Ar} k_e^{4p'} - n_O (k_e^{5P} + k_{csc}^{5P}) - n_{O_2} k_{de}^{5P} \right]. \tag{37}$$

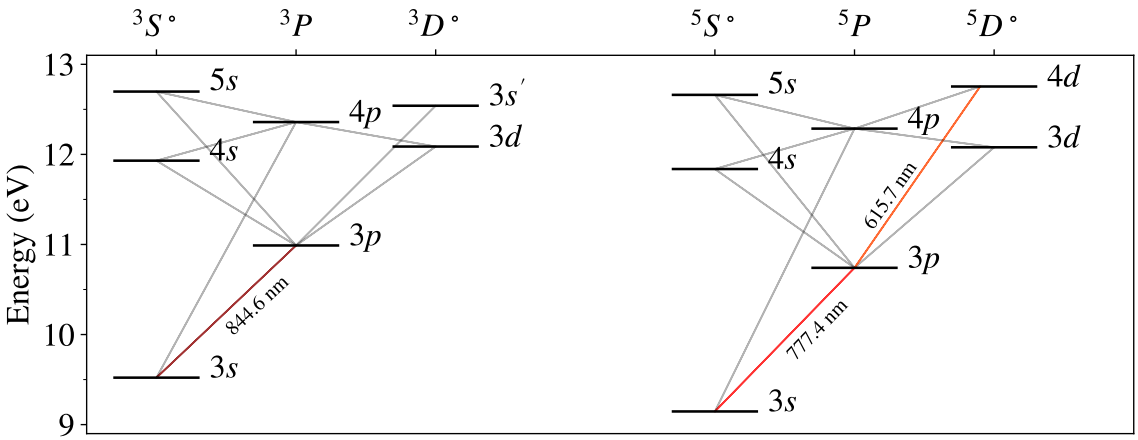

Figure 10. Partial energy level diagram for atomic oxygen. Radiative transitions with Einstein A coefficients greater than $10^5\ s^{-1}$ are shown. Oxygen lines used for actinometry are labeled with wavelengths and shown in color. The O($2p^4\ ^3P$) ground state, which is not shown, belongs to the triplet manifold, therefore the lowest quintet state, O($3s\ ^5S^\circ$), is metastable.

Molecular Nitrogen.

In order to better compare the results of the 3 atomic oxygen lines, use the common N_2/N_2^+ line ratio method [40,44] is used in order to make an independent determination of the experimental f_e. This method compares the relative excitation of the $N_2(C^3\Pi_u)$ state to that of the $N_2^+(B^2\Sigma_u^+)$ state by observing the second positive system (SPS), $N_2(C-B)$, and the first negative system (FNS), $N_2^+(B-X)$. The line intensity models as used by Isola et al. [44] are as follows

$$I_{SPS}(v', v'') = P_{SPS}(v', v'') \left[n_X n_e k_e^{(X-C)} \right], \tag{38}$$

$$I_{FNS}(v', v'') = P_{FNS}(v', v'') \left[n_X n_e k_e^{(X-B)} + n_e^2 k_e^{(Xp-B)} \right], \tag{39}$$

where v', v'' are the initial and final vibrational quantum numbers, respectively and n_X is the density of $N_2(X^1\Sigma_g^+)$. In the above equations it is assumed that $N_2(C^3\Pi_u)$ follows the corona model i.e. population is dominated by electron excitation from $N_2(X^1\Sigma_g^+)$ and loss is dominated by spontaneous emission. In the case of $N_2^+(B^2\Sigma_u^+)$, population occurs by both electron impact ionization from $N_2(X^1\Sigma_g^+)$ and electron excitation from $N_2^+(X^1\Sigma_g^+)$, while loss also dominantly proceeds through spontaneous emission. In the latter case, assumed quasi-neutrality of the plasma along with the assumption that $N_2^+(X^1\Sigma_g^+)$ is the dominant ion are used to substitute the density of $N_2^+(X^1\Sigma_g^+)$ with that of the electron density in equation 39. To account for the likely non-negligible densities of oxygen and argon ions, the slight correction that $n_{N_2^+} \approx \rho_{N_2} n_e$ is made, where ρ_{N_2} is the fractional partial pressure of N_2. A particular line ratio of interest is then

$$\frac{I_{SPS}(v', v'')}{I_{FNS}(v', v'')} = \frac{P_{SPS}(v', v'')}{P_{FNS}(v', v'')} \left[\frac{n_X k_e^{(X-C)}}{n_X k_e^{(X-B)} + \rho_{N_2} n_e k_e^{(Xp-B)}} \right]. \tag{40}$$

Quenching rates for both the $N_2(C^3\Pi_u)$ and $N_2^+(B^2\Sigma_u^+)$ are used to calculate the effective lifetime of each state since they are available for both N_2 and O_2 collisional partners, rates used are given in table 7. Equation 40 can be used to calculate the modeled band ratio for a given BOLSIG EEDF (f_e) and electron density. Such ratios are calculated for a wide range of possible EEDFs and corresponding reduced electric fields, solutions can then be selected as any EEDF which corresponds to an intersection of the experimentally measured intensity ratio and the modeled intensity ratio. In this way the $N_2(C^3\Pi_u)$ / $N_2^+(B^2\Sigma_u^+)$ band ratio can be used to estimate the experimental EEDF and corresponding effective electron temperature for a given electron density. For sufficiently hot discharges with low electron densities, the excitation route $N_2^+(X^1\Sigma_g^+) \rightarrow N_2^+(B^2\Sigma_u^+)$ may be reasonably ignored as the ratio is only weakly a function of electron density. However, for our expected electron density (up to approximately 10^{12}cm^{-3}, based on previous studies), it was found that the excitation route $N_2^+(X^1\Sigma_g^+) \rightarrow N_2^+(B^2\Sigma_u^+)$ is important and the mechanism presents the existences of two

electron temperature solutions (one cold and one hot) for a given electron density. This situation arises due to the competition between the two production mechanisms of $N_2^+(B^2\Sigma_u^+)$, found in the denominator of equation 40, and the large difference in activation energies of the two processes. As such, the same relative intensity, I_{FNS}, can be achieved in two cases; one at low temperatures where the cross section for the $N_2^+(X^1\Sigma_g^+) \rightarrow N_2^+(B^2\Sigma_u^+)$ is dominant and one for higher temperatures where the $N_2(X^1\Sigma_g^+) \rightarrow N_2^+(B^2\Sigma_u^+)$ route dominates. This lack of a unique solution was similarly observed by Steves et al. [47]. Though the ratio remains more sensitive to electron temperature than electron density for densities lower than 10^{13}cm^{-3}, it is necessary to assume a reasonable electron density and further to resolve between the two electron temperature solutions. For this purpose, an electron density of $8 \times 10^{11}\text{cm}^{-3}$ was assumed for N_2/N_2^+ results presented in section 4.4, the basis of this assumption is discussed in section 4.5. Both possible corresponding electron temperature solutions are presented in section 4.4.

Table 7. Quenching rates relevant to this work ($10^{-10}\text{cm}^3\ \text{s}^{-1}$). Gas temperatures from references [2–5] were stated as 300 K or near room temperature, reference [6] was measured at 330 K, and all others are assumed to have been measured at 300 K.

$m\backslash i$	$N_2(C^3\Pi_u)_{v=0}$	$N_2^+(B^2\Sigma_u^+)_{v=0}$	Ar $(4p'^{\,2}\,[^1/_2]_0)$	O $(3s\,^5S^\circ)$	O $(3p\,^5P)$	O$(3p\,^3P)$
N_2	0.132 [40]	8.84 [40]	0.32 [4]	0.35 [67]	-	5.9 [2]
O_2	3.0 [5]	10.45 [6]	7.6 [4]	2.2 [67]	11 [3]	9.3 [2]
Ar	-	-	0.16 [4]	2.9e-5 [2]	-	0.21 [101]

4.2 Modeling O($3s\,^5S^\circ$) density and electron density dependence

Analytic model.

A similar expression to those used in section 4.1 can be developed to estimate the density of the metastable $3s\,^5S^\circ$ state and its dependence upon electron density. Assuming

production proceeds via direct electron excitation from the ground state, electron induced cascade emission, and electron impact dissociative excitation while loss occurs dominantly by collisional processes and weakly by spontaneous emission (as the radiative lifetime is 0.18 ms [33]), the steady state density of the 3s ^{5}S$^\circ$ state can be approximated as

$$n_{5_S}(n_e, n_O, n_{O2}, P, f_e) = [n_O n_e (k_e + k_{csc}) + n_{O_2} n_e k_{de}]\, \tau(P), \tag{41}$$

where the lifetime, τ is calculated at the working pressure, P, and for the appropriate gas composition. Collisional relaxation rates for relevant collisional partners are given in table 7. Alternatively, if the 3s ^{5}S$^\circ$ density is known, equation 41 can be rewritten to solve for electron density:

$$n_e = \frac{n_{5_S}}{[n_O(k_e + k_{csc}) + n_{O_2} k_{de}]\, \tau(P)}. \tag{42}$$

Equation 42 above creates the potential for an experimental determination of electron density after actinometry methods have determined the oxygen ground state and metastable densities. In addition to using the analytical model discussed above, the CRM as detailed in chapter III can be used to predict the 3s ^{5}S$^\circ$ steady state density for our experimental parameters along with a particular value for electron density, n_e. Because n_e is the only unknown and the 3s ^{5}S$^\circ$ steady state density strongly depends on n_e, n_e can be determined by minimizing the residual between the experimentally determined metastable 3s ^{5}S$^\circ$ density and the modeled 3s ^{5}S$^\circ$ density. This process will be used and compared to the analytical method described above (equation 42) and discussed in sections 4.4 and 4.5.

4.3 Experimental Setup

The discharge used in this work was a relatively simple microwave discharge which was designed to operate in the medium pressure regime (0.1-10 Torr) and at high power. The

general experimental apparatus is detailed in figure 19. Microwave power was generated with a high power (6 kW) magnetron operating at 2.54 GHz and coupled into a WR340 rectangular waveguide (43 x 86 mm). The operating mode was the transverse electric TE10 mode. Reflected power was managed and measured using an inline circulator and a motorized 3 stub tuner was used for impedance matching. Forward of the circulator and tuner, the plasma was generated in a fused quartz tube with an inside diameter of 1 cm and approximately 60 cm in length, which was placed through the waveguide and was configured so that the electric field is at a maximum at its location and is parallel to the tube axis. To accomplish this, a suitable hole was drilled through both of the wider transverse sides a distance $\lambda/4$ from the waveguide end. The waveguide terminates into copper plate. Copper tubing several centimeters in length was placed around the quartz tubing on the outside of the waveguide in order to reduce microwave leakage, it also likely contributed to the plasma generation efficiency. To further reduce leaking, copper mesh surrounded the remainder of the quartz tubing, which still allowed for optical probing of the plasma volume. The pressure, flow, and gas content were all regulated using three mass flow controllers, calibrated for N_2 (200 SCCM), O_2 (101 SCCM) and argon (140 SCCM). Vacuum was provided by a small oil roughing pump. Pressure was monitored on the inlet side of the tube with a convection gauge and on the vacuum side of the tube with two capacitance manometers of different precision ranges (1 Torr and 1000 Torr full scale ranges).

For the results presented below, the forward microwave power was set to 3 KW and the average power absorbed by the system remained near 600 watts. The argon actinometer was provided at a fractional partial pressure of approximately 5%. Operating pressure was sustained at 0.75 Torr (100 Pa), which corresponds to a total gas flow rate of approximately 50 SCCM. The argon mass flow controller was operated at approximately 1.77% of full scale which can introduce significant error when calculating gas partial fractions. To assess

this error, the differences in required flow rate of a mass flow controller operating near 50 SCCM to sustain a pressure of 0.75 Torr with and without the 5% admixture of argon was used. In this case, the error of the measurement is 1% of the set point or 0.5 SCCM. In this way the argon mass flow controller's set point was confirmed to be approximately 2.5 +/- 0.5 SCCM. Thus, the total error in argon number density is near 20%. This value of uncertainty was propagated for calculation of O(3s ^{5}S$^\circ$) and electron density uncertainty but was not included in the comparison of dissociation fractions as any uncertainty would affect the results for each actinometry ratio nearly uniformly. At this volumetric flow rate, the linear flow speed is approximately 10 m/s with a residence time in the quartz tube of approximately 60 ms. The microwave power source was enabled for a duration of 5 seconds for each acquisition and the spectra was time integrated for 3 seconds in the center of the pulse duration to avoid any inconsistencies related to delayed plasma ignition or early termination jitter. Total oxygen fraction was varied from nearly zero to approximately that of the oxygen fraction in air (21%), though it was found that for oxygen fractions below 6% the signal to noise ratio for the 616 nm oxygen line was too low to extract reliable line intensities.

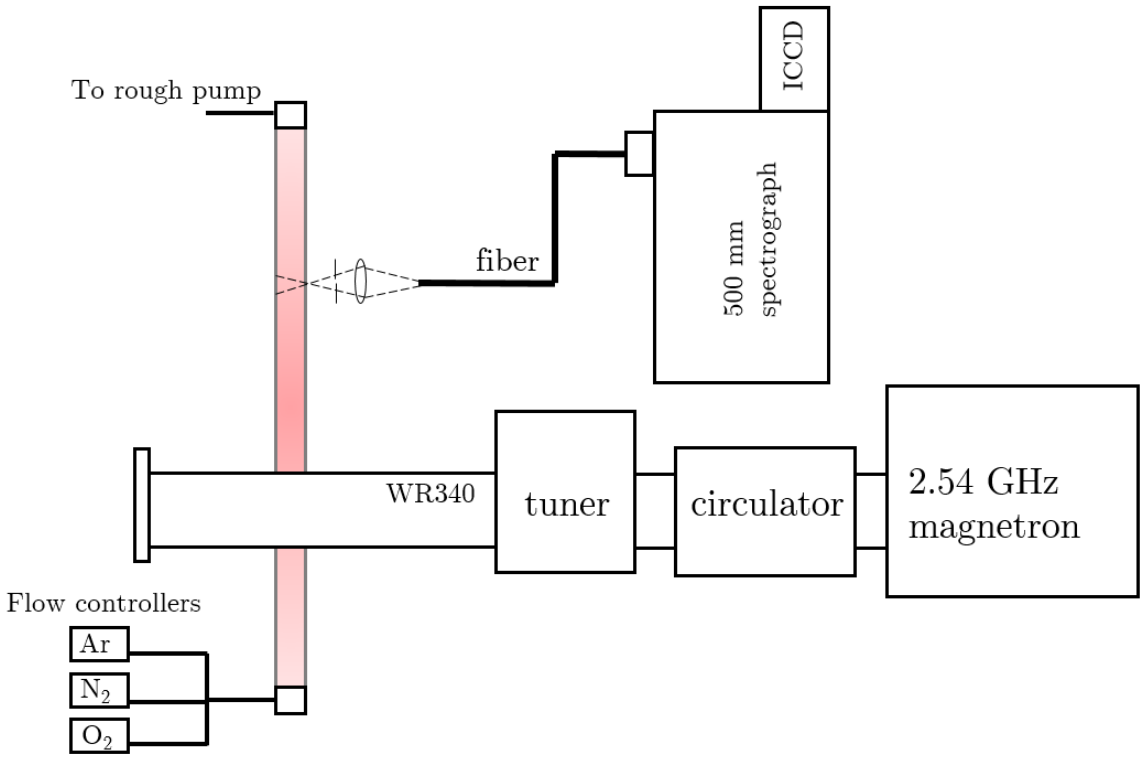

Figure 11. General experimental setup of microwave discharge and OES instrumentation

Spectroscopic data was collected with a 500 mm focal length Andor spectrograph with a 1200 line/mm grating blazed at 500 nm and an Andor iStar 334t intensified CCD camera. For the near UV data (350-450 nm), light was collected with an iris and a UV 50 mm lens focused on a circular 100 μm optical fiber bundle. The fiber was coupled to the spectrometer slit where the fibers are vertically aligned with the slit and ICCD counts were vertically binned along the slit. For the red side of the spectrum, light was collected using an iris and a two lens collimating system with an approximate focal length of 25 mm incident on the same circular fiber bundle. In both cases the field of view of each optical system constituted a cone approximately 2 mm in diameter crossing the radial center of the quartz tube approximately 10 cm above the waveguide. Thus the measurements in this experiment reflect the plasma conditions averaged along the light cone at an axial location 10 cm above the waveguide. Separate collection optics were used to maximize

optical efficiency in both regions and provide a relatively flat optical response for each. A NIST traceable Deuterium/Halogen calibration lamp (Ocean Optics DH-3plus-CAL) was used to calibrate the relative response of the complete optical systems. In the UV the spectral response only changes by approximately 3% between 380 and 390 nm (near the two lines considered). The blue/green portion of the spectra was also very flat, however in the infrared the detectivity sharply decreases; the detectivity at 844 nm was found to be approximately 25% the value of detectivity at 777 nm. Though, due to the strong nature of the 777 nm and 844 nm lines, signal to noise was sufficiently high to overcome any detectivity issues (approximately 30 for the 777 nm oxygen line). To test the accuracy of the calibration, lines ratios from mercury/argon and mercury/neon lamps with shared upper states were compared against their known Einstein A coefficient ratios. In all cases it was shown that the calibration resulted in measured line ratios which agreed with the Einstein A coefficient ratios with error less than the propagated Einstein A coefficient uncertainty and the average error was approximately 10%. For this reason, an estimated uncertainty in line ratios related to calibration of 10% is used for all of the results presented below. Atomic line-widths using the spectroscopic system had a full width at half maximum (FWHM) of approximately 0.1 nm and are considered to be instrument line-shape dominated.

4.4 Results

The general process is as follows: (1) the N_2/N_2^+ method is used to determine effective electron temperature and gas temperature, (2) the 844 nm actinometry ratio is used to determine dissociation fraction, (3) 777 nm actinometry is used to determine relative oxygen 3s $^5S^\circ$ density, and (4) analytic and CRM models of 3s $^5S^\circ$ density are used to determine electron density.

Actinometry Spectra and Line Intensities.

Figure 12 below shows an example of the collected atomic oxygen and argon spectra for the gas composition $N_2/O_2/Ar = 0.75/0.20/0.05$. Satisfactory removal of significant background spectra was achieved by collecting spectra in absence of the species of interest and allowed for isolation and integration of each line. In the case of the argon spectra near 750 nm, the background is largely composed of second order grating diffraction from the N_2 SPS. Additionally, this methodology was effective in showing that the presence of the argon actinometer had negligible influence on the remainder of the spectra. The resulting subtraction and integration of the four actinometry lines for a range of molecular oxygen partial fractions is shown in figure 13. Due to its relatively weak intensity, the 615 nm oxygen line is scaled by a factor of 100. The estimated uncertainty in line intensities is given by the error bars and represent an assumed 7% error in integrated line intensity as well as the standard deviation of 3 separate measurements. Figure 13 shows that the argon line is negligibly influenced by increased oxygen partial fractions while the oxygen lines increase nearly linearly with increasing O_2 partial pressure. Linear extrapolation of the oxygen line intensities approximately approach zero for zero partial pressure of O_2, with a linear regression of the first 4 points (0.065- 0.12 O_2 partial pressure) leading to integrated intensities of -8, 8.6, and -29 Counts s^{-1}nm for the 844 nm, 777 nm and 615 nm $\times 100$ lines at $n_{O_2} = 0$, respectively.

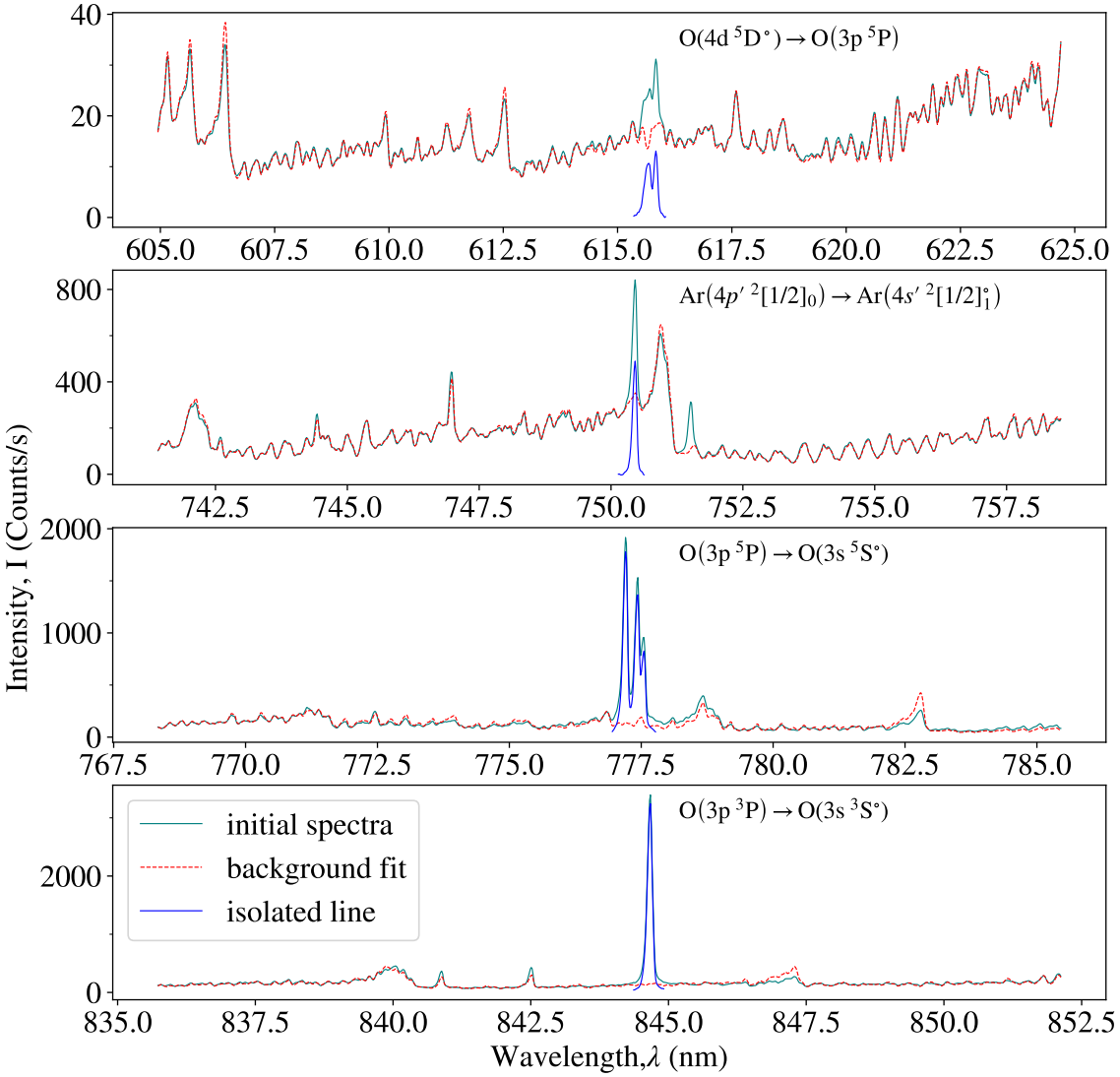

Figure 12. Oxygen and argon spectra, background, and corrected spectra for gas ratio $N_2/O_2/Ar = 0.75/0.20/0.05$. The backgrounds were experimentally measured in absence of either oxygen or argon. These experimentally determined backgrounds were then scaled to fit the spectra containing the argon and oxygen lines, though in most cases the scaling was minimal as the background spectra was highly repeatable and not significantly impacted by absence of argon or oxygen. All curves are calibrated as discussed in section 4.3.

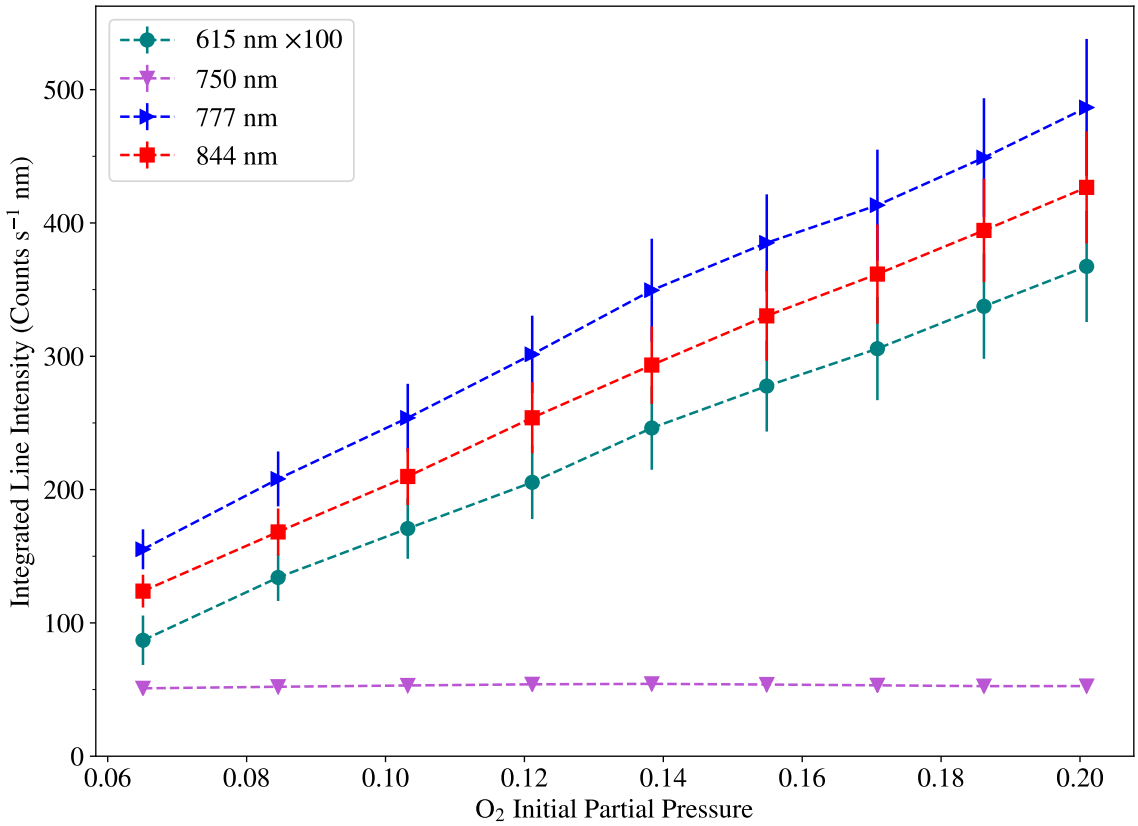

Figure 13. Integrated line intensities for each of the lines used in the 3 actinometry ratios as a function of initial O_2 partial pressure

Molecular Nitrogen Spectra and Line Intensities.

The line ratio method described in section 4.1 can be applied to any optically accessible SPS and FNS bands if the appropriate cross sections are used. The $v' \rightarrow v'' = 0 \rightarrow 0$ band of the FNS, which peaks near 391 nm, is typically used as it is often the strongest part of the $N_2^+(B-X)$ system. For this work, this band along with the $v' \rightarrow v'' = 0 \rightarrow 2$ band of the SPS was used, due to its close proximity at 380 nm and its origination from the $v = 0$ vibrational state of $N_2(C^3\Pi_u)$. As discussed in section 2.3, full spectral simulations of both the SPS and the FNS are used to extract accurate band intensities as well as rotational temperatures and vibrational distributions. Figure 14 below shows an example of the spectral simulation fit to experimental data. Figure 14 (b) shows the result of a least square fit with

rotational temperature, vibrational distribution function and SPS/FNS ratio as optimization parameters. The N_2 SPS fits correspond to an average $N_2(C^3\Pi_u)$ rotational temperature of $T_r = 915$ K with a standard deviation of 30 K. Rotational temperatures were not found to be significantly sensitive to changes in O_2 partial fraction. The resulting fit is used to model the SPS $v' \rightarrow v'' = 0 \rightarrow 2$ band and the $v' \rightarrow v'' = 0 \rightarrow 0$ band of the FNS with the remainder of the spectrum removed so that they may be integrated and their ratio calculated. In addition to the fit parameters discussed above, the model accounted for a small amount of radiation trapping. Though inclusion of radiation trapping as a fit parameter reduced fit residuals for the SPS, it did not significantly change the integrated band intensities.

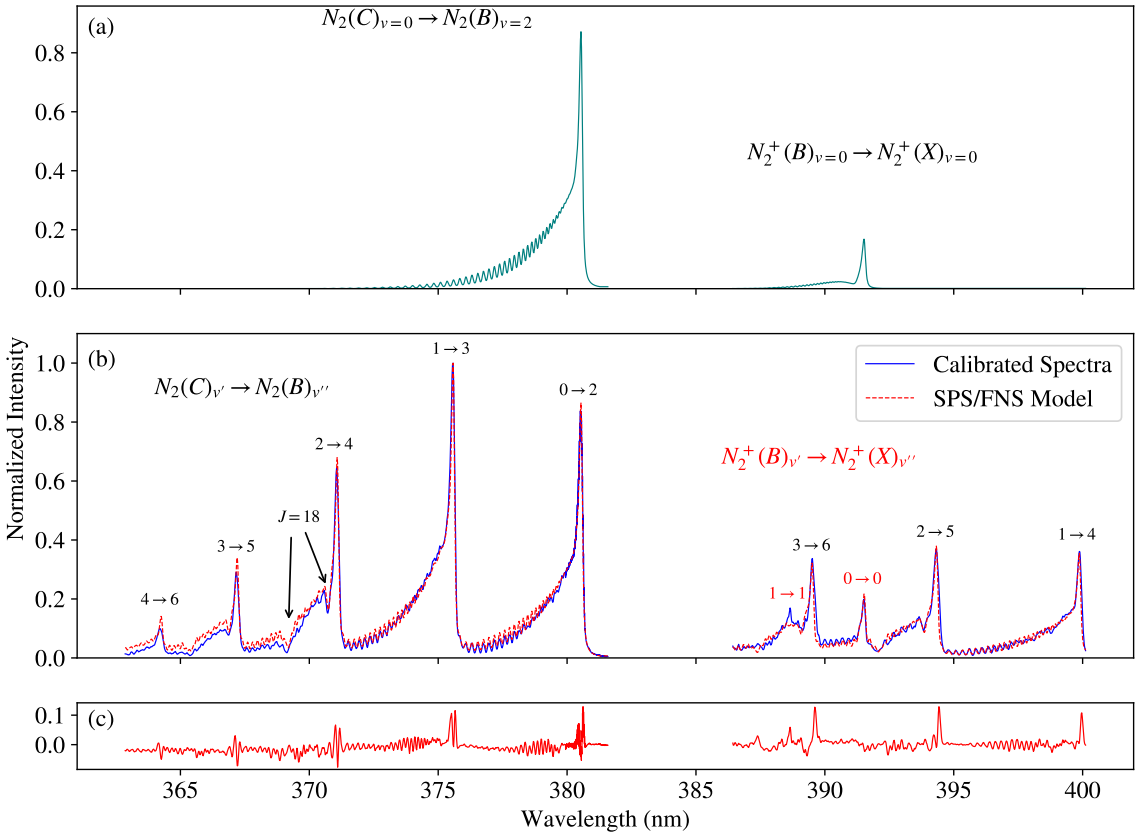

Figure 14. Example of N_2 SPS and FNS fitting: a) model fit of isolated band for integration and use in line ratio, b) experimental data and least squares fit, c) residual of fit and model. Band heads for SPS are labeled in black by $v' \rightarrow v''$ and the FNS band heads are similarly labeled in red.

We report one significant irregularity in the data which does not agree with the SPS

model or most spectra available in literature in which rotational transitions near $J = 18$ in $N_2(C^3\Pi_u), v \geq 2$ states are significantly diminished compared to the Boltzmann distribution and those in other vibrational states. This irregularity exists for all bands examined ($\Delta v = 1, 2, 3$) and can be seen in figure 14 (b) most obviously near 369 nm and 392 nm. No satisfactory explanation for this irregularity was arrived at, and it appears only two previous works describe similar observations. In those cases the unusual spectra were theorized to have been caused by rotational perturbations related to interactions of the $C^3\Pi_u$ state with $C''^5\Pi_u$ [38, 102]. However, it is not expected that this irregularity had any impact our results as 1) the irregular distribution was fit (by modifying the relative density of the $J = 18$ rotational state) and removed with a relatively low residual and 2) none of the $N_2(C^3\Pi_u), v \geq 2$ states were used in calculating line ratios.

The ratio of interest, $I_{SPS(0,2)}/I_{FNS(0,0)}$ is shown in figure 15 below for the range of fractional O_2 concentrations considered for this experiment. The error bars in figure 15 again include both the standard deviation of 3 measurements as well as an assumed 5% error for each integrated band intensity.

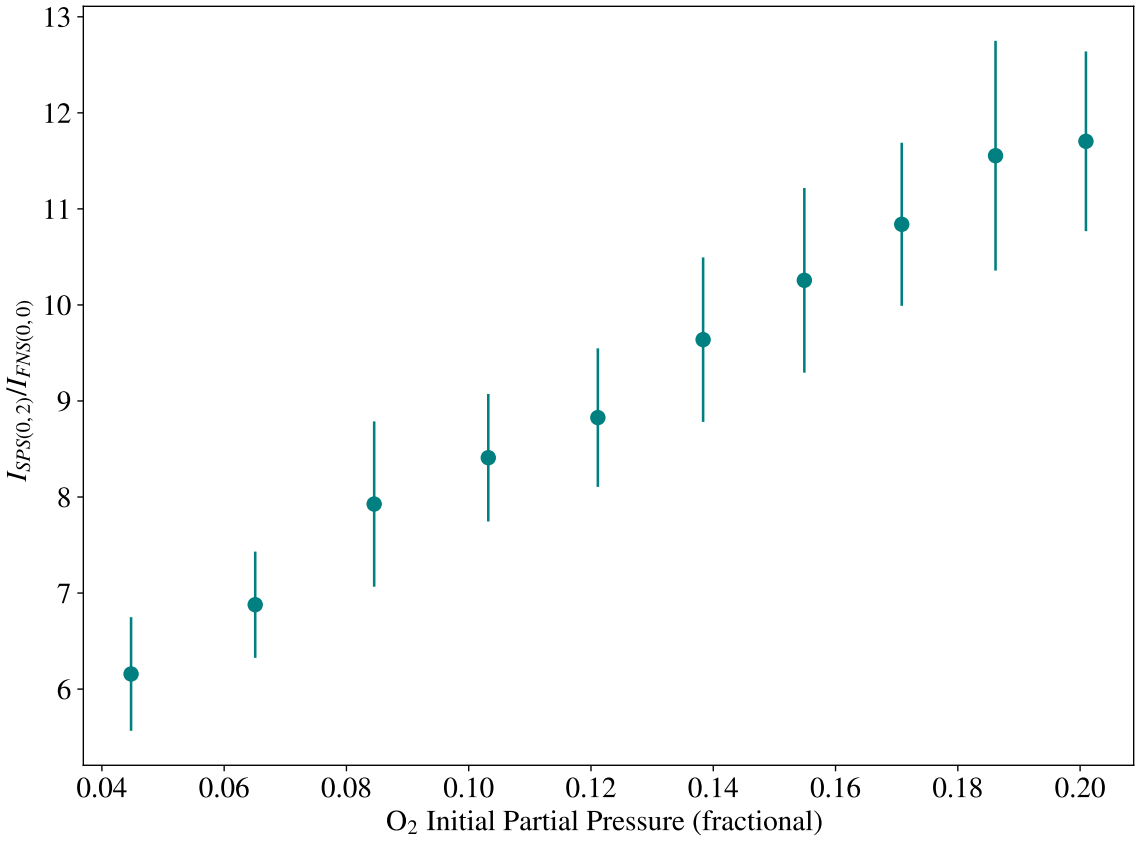

Figure 15. Experimental SPS / FNS integrated band ratio as a function of O_2 partial pressures.

Effective electron temperatures.

The SPS/FNS measured ratios as shown in figure 15 above can be used to estimate the effective electron temperature using equation 40 and the process described in section 4.1. However, as discussed in section 4.1, equation 40 yields two sets of solutions for the measured line ratios. Both solutions are presented in figure 16 below. Additionally, using any 2 of the 3 available actinometry ratios (as in equations 35 and 36) a simultaneous determination of both atomic oxygen density and effective electron temperature can be made. Initially, the metastable excitation rate ($3s\ ^5S^\circ \rightarrow 3p\ ^5P$) was assumed to be zero in equation 34, and an actinometry equation identical to equations 35 and 36 was used for the 777 nm / 750 nm actinometry ratio. However, the 844 nm / 777 nm combined actinome-

try yielded no meaningful solutions for the range of electron temperatures considered (0.7 eV - 7.5 eV) when metastable excitation was ignored, and for this reason is not included in figure 16. Instead, Figure 16 below shows the results of effective electron temperature determinations using both the N_2/N_2^+ method as well as the 844 nm / 777 nm combined actinometry technique where metastable excitation of the 3p ^{5}P state is included for 3 different metastable densities corresponding to $n_{5S^\circ}/n_O = 2\times10^{-4}$, 5×10^{-5}, and 10^{-5}. The error bars in figure 16 represent the propagation of the uncertainty in measured line/band intensities through the line ratio models, they do not include uncertainty introduced by cross sections, Einstein A coefficients or quenching rates. The results show that if metastable excitation is included at a fractional concentration relative to the total atomic oxygen density of 2×10^{-4}, the combined actinometry approach provides reasonable agreement with the hot N_2/N_2^+ results, while a value of 5×10^{-5} shows good agreement with the cold N_2/N_2^+ results. For the experimental conditions here, it is argued that the cold solution (2-3 eV) more reasonably reflects the actual EEDF than the hotter solution branch (4-4.5 eV). This argument is made on the following basis: (1) previous studies of similar N_2-O_2 microwave discharges report electron temperatures of 2.21 eV (derived from E/N) [78], approximately 2 eV (OES) [47] and approximately 3 eV (double Langmuir Probe) [103], (2) the general increasing trend of the cold temperatures with respect to partial fraction of O_2 agrees with both the actinometry results and the results of Ichikawa et al. [103], (3) actinometry based on the high temperature solutions yields dissociation fractions which are much higher than expected and which disagree with all previous work, and (4) in general high frequency (MW) discharges are characterized by relatively low values of reduced electric field [40]. For the remainder of the results, the effective electron temperatures and associated EEDFs as predicted by cold branch the SPS/FNS (N_2/N_2^+) method are used.

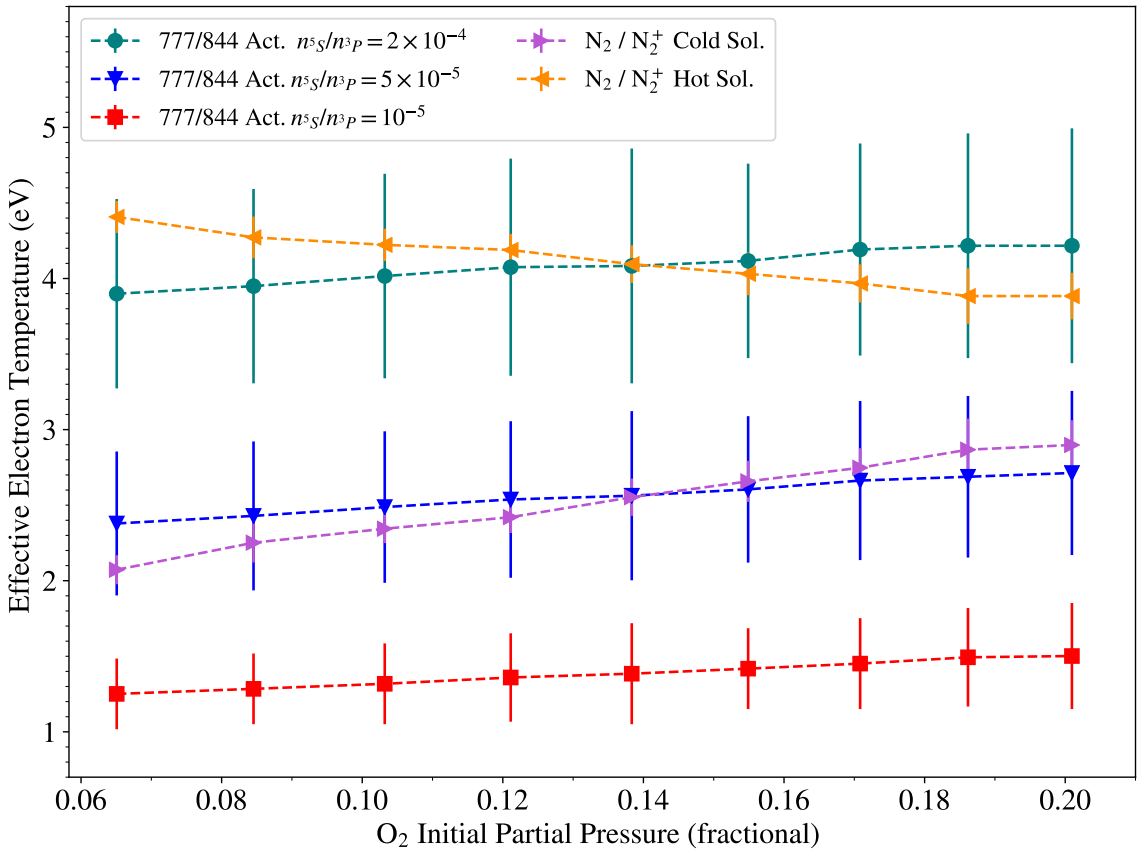

Figure 16. Calculated effective electron temperatures using the SPS/FNS (N_2/N_2^+) method and combined 844 nm / 777 nm argon actinometry with metastable excitation included for the $3p\ ^5P$ state for several fractional densities of $3s\ ^5S^\circ$.

Dissociation Fraction.

For a more direct comparison of the oxygen line models and the experimental results, figure 17 shows the dissociation fraction predicted by argon actinometry of each of the three lines. Dissociation fraction is defined here as n_O/n_{O_2}, where n_{O_2} represents the initial O_2 density, prior to dissociation. The effective electron temperatures and corresponding EEDFs used were those calculated using the SPS/FNS (N_2/N_2^+) method as discussed in section 4.4 above. In this case, it can be assumed that the metastable excitation rate is zero in equation 34. The standard 844 nm / 750 nm method yields dissociation fractions lower than all other results, at an average of approximate dissociation fraction of 53%, while the

777 nm / 750 nm actinometry predicts significantly higher dissociation at approximately $n_O/n_{O_2} = 103\%$, which disagrees with similar measurements in literature of microwave discharges which range from 25–60% [47, 78, 104] to significantly lower in the case of Ichikawa et al [103]. This disagreement of the 777 nm results with both previous work and the 844 nm results, represents stronger 777 nm emission than is accounted for by electron excitation channels included in the extended corona model (which ignores metastable excitation). This result is consistent with the observations of Collart et al. [49]. The results for the 616 nm / 750 nm actinometry are presented for both the case quenching is ignored and in the case quenching rates are assumed to be equal to those of the 844 nm line. In the case which quenching is ignored, the 616 nm based actinometry results are close to those predicted by the 844 nm based actinometry, with reasonable agreement for O_2 initial partial pressures greater than 15%. When quenching rates equal to that of the 844 nm line are assumed, results show good agreement with the standard 777 nm based actinometry approach where metastable excitation is ignored. The error bars shown in figure 17 reflect uncertainty in measured line intensities and the uncertainty in 3p ^{5}P quenching coefficients as discussed in section 4.1.

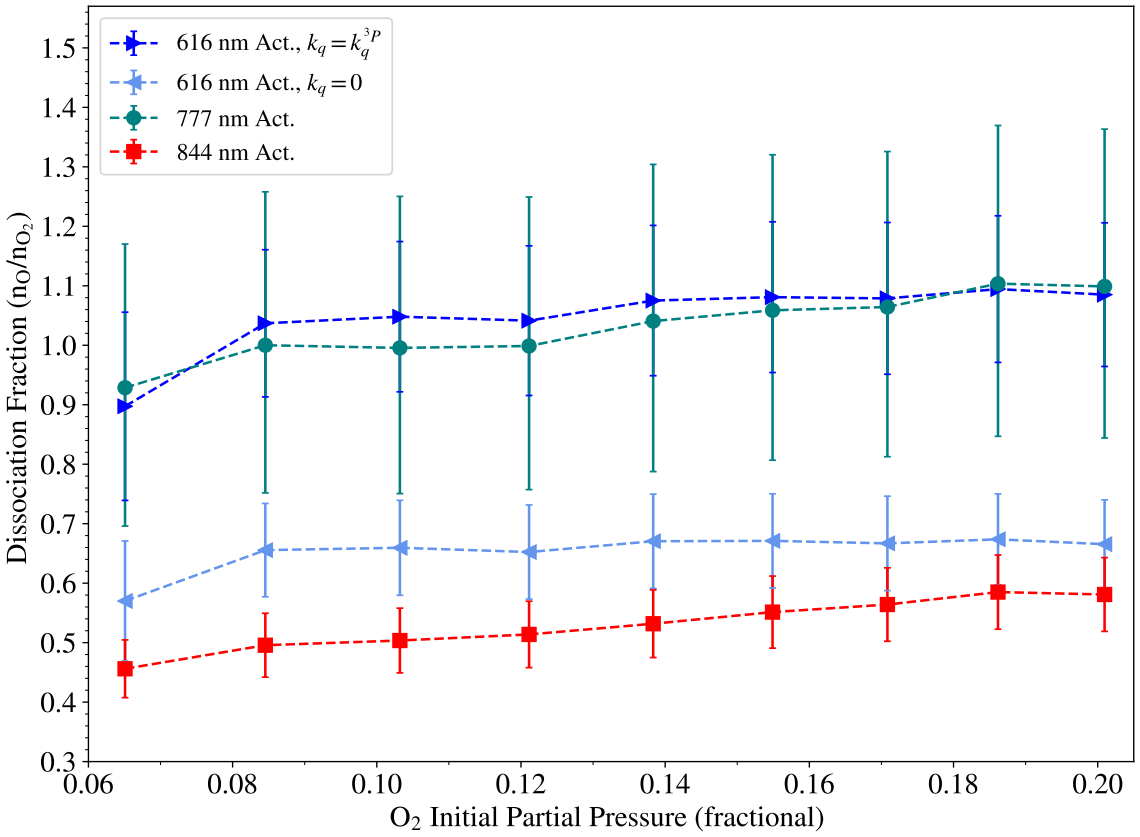

Figure 17. Oxygen dissociation fraction predicted by argon actinometry of the 616 nm, 777 nm and 844 nm oxygen lines, using EEDFs corresponding to effective electron temperatures predicted by the SPS/FNS (N_2/N_2^+) method. The rate k_q refers to the total effective quenching rate.

O($3s\ ^5S^\circ$) and electron densities.

If it is assumed that the dissociation fraction predicted by the 844 nm actinometry in figure 17 is correct and further assume that the disagreement of the 777 nm actinometry is due to metastable excitation from O($3s\ ^5S^\circ$) , then the absolute density of O($3s\ ^5S^\circ$) can be determined using equation 37. This process can be seen as identical to adjusting the metastable density and its enhancement of the 777 nm line until the dissociation fraction as predicted by the 777 nm actinometry in figure 17 agrees with the results of the 844 nm actinometry ratio. Additionally, using both the analytic model (equation 41) and the collisional-radiative model as discussed in chapter III, the electron density can be deter-

mined for each value of O(3s $^5S^\circ$) density. Figure 18 (a) shows relative O(3s $^5S^\circ$) concentrations as determined using this combined actinometry approach while 18 (b) shows the corresponding electron densities as predicted by each model. The relative O(3s $^5S^\circ$) concentration has a similar increasing trend with respect to O_2 partial pressure as the electron temperatures and dissociation fractions. The electron densities, as determined using the analytic model, show excellent agreement for all initial partial pressures of O_2 with the values obtained using the CRM. This indicates that the extended corona model is a complete model for these operating conditions and more complex mechanisms such as electron excitation to the 3s $^3S^\circ$ and 3p ^3P states, which could introduce a more complex dependence on electron density than the one considered by the basic analytic model and equation 42, are not important for these conditions.

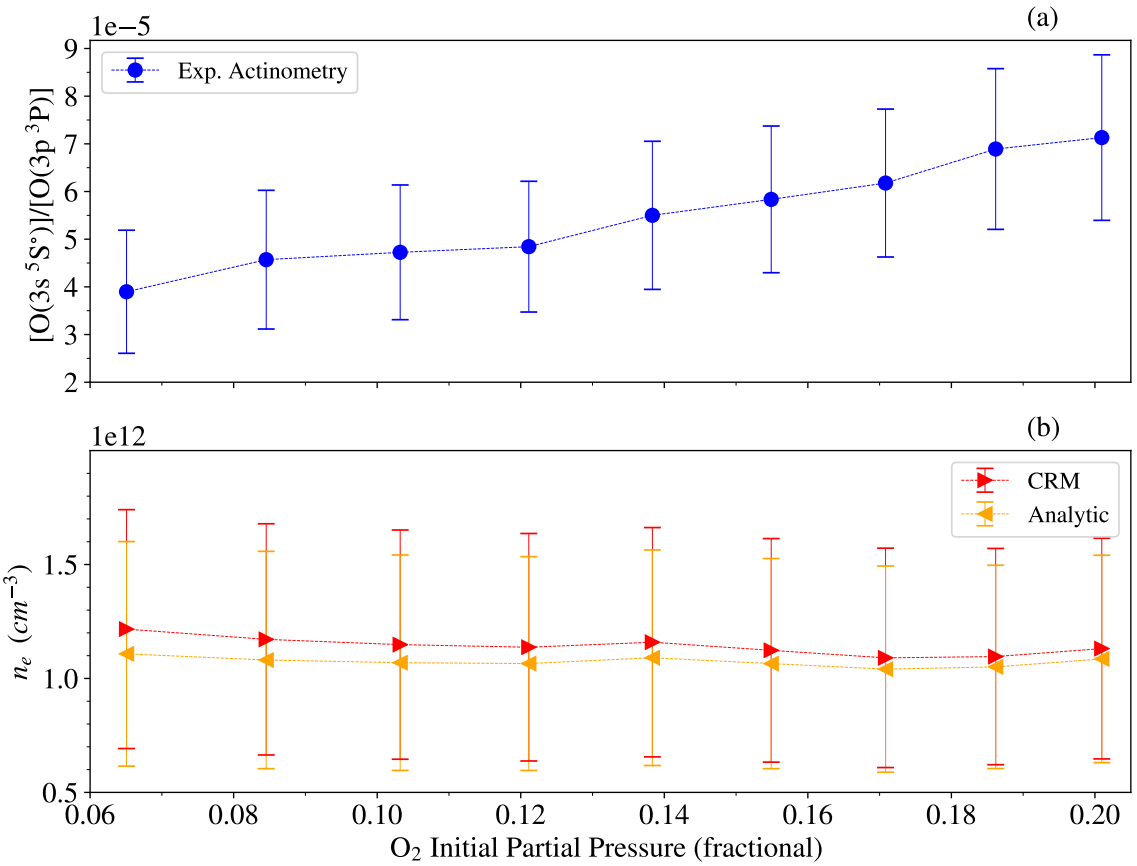

Figure 18. Concentration of O(3s ^{5}S°) relative to the ground state O(2p^4 ^{3}P) as determined from experimental actinometry and corresponding electron densities as calculated using the analytic and CRM models.

In lieu of an accurate in situ electron diagnostic for comparison with the measured electron densities, table 8 below provides a summary of electron densities as determined for similar microwave discharges in literature as well as the values determined in this work for both models. Values determined here are reasonably consistent with the literature values, and though they are higher than the other experimental results, they are within experimental uncertainty of the 2 values obtained experimentally at 1 Torr, [78, 103], which is expected as those measurements have discharge pressures and powers most similar to this work.

Table 8. Electron densities determined for similar microwave (2.54 GHz) discharges in literature and for this work. Ranges of values for some measurements are based on spatial variations while others contain only uncertainty. Measurement types for literature values include microwave interferometry (MWI), double Langmuir probe (DLP), multipole resonance probe (MRP) and two models. Values from this work represent the mean electron density and mean uncertainty over the range of partial oxygen fractions considered.

n_e (10^{11}cm^{-3})	Gas Comp.	P (Torr)	Power (W)	Meas. Type	Ref.
(11.4 ± 5.0)	N_2/O_2/Ar	0.75	600	CRM/Act.	this work
(10.7 ± 4.7)	N_2/O_2/Ar	0.75	600	Analytic/Act.	this work
(6 ± 1)	O_2	1.0	600	MWI	[78]
(5 ± 2)	N_2/O_2	1.0	500	DLP	[103]
(13 ± 7)	O_2	7.5	400	Model	[105]
(47.5 ± 10.5)	N_2/O_2	2.25	129	Model	[106]
(1.25 ± 0.26)	N_2(Trace)/O_2	0.19	600	MRP	[47]

4.5 Discussion

As observed in previous work [85–88], the results above show that the standard 2 mechanism excitation model (extended corona) for the O(3p ^{5}P) state does not agree with the same model for the O(3p ^{3}P) state, for some experimental conditions including those considered here. This is evident due to the lack of agreement of dissociation fractions (figure 17) as well as electron temperatures predicted by the N_2/N_2^+ method and those predicted using a 2 ratio combined actinometry approach using the 844 nm / 750 nm and 777 nm /750 nm ratios which ignores metastable excitation. The inclusion of metastable excitation from the O(3s ^{5}S$^\circ$) state, using cross sections calculated by Barklem [18], mitigates this disagreement and allows the 2 actinometry ratios along with the N_2/N_2^+ method to be utilized to simultaneously determine effective electron temperature, dissociation fraction, and O(3s ^{5}S$^\circ$) density. Furthermore, a basic analytic model for O(3s ^{5}S$^\circ$) densities (equation 41) shows excellent agreement with the relatively complete oxygen CRM and allows for direct calculation of electron density using effective electron temperatures, dissociation fractions, and O(3s ^{5}S$^\circ$) densities as determined from the combined actinometry technique. The resulting electron density as determined using this method and the CRM are relatively consistent with other values in literature for similar microwave discharges. Together, these results strongly suggest that metastable excitation from O(3s ^{5}S$^\circ$) is an important mechanism when using the 777 nm line for actinometry for our conditions and likely for the conditions used by previous authors who observed significant disagreement between methods using 777 nm and methods using the 844 nm line. These results reflect the same behavior observed in chapter III, where the importance of metastable excitation in sufficiently ionized discharges was confirmed using the oxygen CRM.

For simplicity, the results above were calculated and presented in a linear fashion, eliminating one unknown at a time. Because of this, it was necessary to assume an electron density before calculation of effective electron temperatures using the N_2/N_2^+ method. Ini-

tially, an average value from literature was assumed and used to calculated effective electron temperature using the N_2/N_2^+ method. Those subsequent EEDFs were then used for the combined actinometry technique, which in turn yielded a new value for electron density. This created an iterative process composed of many complete calculations of all parameters which converged to a final value of $8 \times 10^{11} \text{cm}^{-3}$. Though this value is slightly lower than the average value obtained using the final actinometry results, it falls within the uncertainty of the actinometry results and higher densities do not correspond to solutions to equation 13 for measured N_2/N_2^+ intensity ratios. Thus, the value ($8 \times 10^{11} \text{cm}^{-3}$) represents the approximate average intersection of solutions to the N_2/N_2^+ equation and the actinometry equations for our experimental line ratios and ranges of uncertainty. Though a direct approach which simultaneously solves the actinometry and N_2/N_2^+ equations for all unknowns alleviates the need to initially assume any parameters, it would be less illustrative of the conclusions presented here.

The working pressure and electron density are crucial to the applicability of using this combined actinometry approach to determine electron density. As electron densities increases or pressure decreases, the lifetime of 3s $^5\text{S}^\circ$ becomes dominated by electron processes and collisional quenching with neutrals become negligible. In this case the electron density dependence cancels and thus the technique is no longer sensitive to electron density. For a dominantly O_2 discharge at a pressure of 1 Torr, a gas temperature of 300 K and an electron temperature of approximately 5 eV, the loss rate for electron depopulating processes of the 3s $^5\text{S}^\circ$ state becomes comparable to the quenching rate at $n_e \approx 4 \times 10^{13}$ cm^{-3}. Therefore for these parameters the upper limit in terms of sensitivity is near $n_e \approx 10^{14}$ cm^{-3} and approximate upper limits at different pressures can be found by scaling the electron density by the working pressure in Torr.

Using the available spectroscopic data along with quenching rates equal to those of the 844 nm line, actinometry based on the 616 nm line (4d $^5\text{D}^\circ \rightarrow$ 3p ^5P) does not agree with

the generally trusted 844 nm line and model and instead shows good agreement with the 777 nm based actinometry for which metastable excitation of the 3p ^{5}P state is ignored. Though in the case where quenching of the 616 nm line is ignored, the dissociation fractions show reasonable agreement with the 844 nm based actinometry when O_2 partial pressures approach that of air. This result suggests that either the actual quenching rates for the 4d ^{5}D$^\circ$ state are slow or there is an additional production mechanism, such as metastable excitation, which is not included in the model, as the line is significantly stronger than the actinometry equations predict for dissociation fractions and electron temperatures measured here and in other studies. Independent measurement of either quenching rates or the metastable excitation rate would be required to make further conclusions regarding the importance and likely values of those rates for the experimental conditions used here. The 616 nm / 750 nm does however show a strong correlation to atomic oxygen density, similar to that of the other two often used ratios. If an accurate model for the relative line intensity of the 616 nm is realized, the additional oxygen line could be used to eliminate an additional unknown and remove the need for the argon actinometer. This would allow a comprehensive OES technique using only optically accessible lines of air which could simultaneously determine electron temperature, electron density and dissociation fraction. With regard to the observed disagreement of the 777 nm actinometry results using the extended corona model (which ignores O(3s ^{5}S$^\circ$) metastable excitation), it is possible that other factors, besides the metastable excitation route considered here, contribute to the observed disagreement. In the following sections the influence of three such potential mechanisms is examined in more detail; collisional quenching on oxygen atoms, dissociative excitation from the $O_2(^1\Delta)$ and uncertainties related to selected EEDFs.

Quenching on atomic oxygen.

The results here, as well as previous work, show that for medium pressure microwave discharges, molecular oxygen is highly dissociated, and a value of approximately 53% was measured here. Despite this, the gas composition used to calculate quenching coefficients does not reflect either the changes to molecular oxygen density or the presence of oxygen atoms as a result of the dissociation. With regard to quenching rates, the rates for quenching of the 3p ^{3}P and 3p ^{5}P states (as well as most others) on atomic oxygen are not available in literature. Thus the overall approximation made here is that total quenching from oxygen atoms is equal to the quenching from molecular oxygen which it replaces. Two reasonable limits can be assumed in order to estimate the error introduced by this approximation for 20% O_2 partial pressure. In one limit the quenching rates on atomic oxygen are negligible compared to those of the other species. In this case the lifetimes of the 3p ^{3}P and 3p ^{5}P states would increase by only approximately 2%. In the other limit the quenching rates on atomic oxygen could be double the quenching rates on molecular oxygen. In this case the lifetimes of the 3p ^{3}P and 3p ^{5}P states would decrease by approximately 6%. In both cases the change in lifetimes is small compared to remainder of the experimental uncertainty, and even in the case where the predicted dissociation fraction of the 3p ^{5}P based actinometry decreases by 2% and the result from the 3p ^{3}P based actinometry increases by 6%, the two results are still in significant disagreement and outside of the experimental uncertainties as given in figure 17. Thus, for our conditions, the effect of unknown quenching rates on atomic oxygen collision partners is deemed negligible. This is largely because O_2 at most accounts for 20% of the total gas composition. However, in a highly dissociated discharge in which O_2 is the dominant species these unknown rates may impact the applicability of these actinometry techniques.

Metastable excitation from $O_2(^1\Delta)$.

It was proposed in [79] that the discrepancies between the 777 nm and 844 nm actinometry approaches could be due to metastable dissociative excitation from the long lived $O_2(^1\Delta)$ state which can exist at significant fractions of the total O_2 density. However, due to the unavailability of excitation cross sections from the $O_2(^1\Delta)$ state, estimating the influence of its presence is difficult. One simple estimate can be made by assuming the dissociative excitation cross sections from the $O_2(^1\Delta)$ are simply those of O_2(X) with an appropriate shift in excitation threshold ($\approx 1\ eV$). This assumption carries some degree of validity based on the similarity of potential energy curves of the $O_2(^1\Delta)$ and the O_2(X) states. This approximation however only results in a slight decrease in total dissociative excitation to all states as including $O_2(^1\Delta)$ at any significant fraction only decreases total dissociative excitation from O_2(X). Additionally, in order to model the experimentally observed larger than predicted 777 nm / 844 nm ratio, the dissociative branch would need to increase as dissociative cross sections for the 3p ^{5}P state are nearly double that of the 3p ^{3}P state [64]. If any $O_2(^1\Delta)$ influence on the 844 nm line is ignored, the necessary magnitude of the excitation cross section for the dissociative channel from $O_2(^1\Delta)$ to 3p ^{5}P to solve the discrepancy can be estimated. In the case $O_2(^1\Delta)$ constitutes an unreasonably large fraction of the total O_2 density (50%), the cross section would need to be nearly 6 times greater than that of the dissociative path from O_2(X) with a peak value of approximately $2.6 \times 10^{-17}\ cm^2$. Given these considerations and the fact that inclusion of the atomic oxygen 3s ^{5}S$^\circ$ metastable excitation at 3s ^{5}S$^\circ$ densities consistent with our modeling provides good agreement between the actinometry methods, it seems unlikely that metastable dissociative excitation from $O_2(^1\Delta)$ is an important process for our conditions.

EEDF related uncertainty.

The EEDFs used for actinometry here should be considered a 'best fit' of the experimental EEDF based on N_2/N_2^+ method and the associated cross sections of that technique as well as the inputted cross sections and other parameters used to calculate the BOLSIG EEDFs. It is possible that the EEDFs used here may vary significantly from the actual EEDFs. In particular it is possible there exists a stronger high-energy tail which could disproportionally populate the 3p ^{5}P state and result in more 777 nm emission due to the strong dissociative excitation cross section for the 3p ^{5}P state and its high activation energy. Thus, the discrepancies observed here could be related to a missing population of high energy electrons which are responsible for the additional 3p ^{5}P excitation. However, due to the strongly dissociated nature of this and similar microwave discharges, excitation of 3p ^{5}P proceeds dominantly via electron excitation from the ground state and only weekly via dissociative excitation. Additionally, the presence of a high energy tail (with $E < 50\ eV$) does not actually lead to a reduction in the measured dissociation fraction and instead leads to an increase in n_O/n_{O_2}, as such a tail also strongly increases the argon excitation rate, which the measured density, n_O , directly depends on. This is because the cross section for excitation of the 750.4 nm line $\left(4p'^{\,2}\left[{}^1/_2\right]_0 \rightarrow 4s'^{\,2}\left[{}^1/_2\right]_1^\circ\right)$ remains strong for high energies and greater than the 3p ^{5}P dissociative excitation cross section until approximately 50 eV. And since the 777 nm results already constitute a likely unreasonably high dissociation fraction, as compared to previous results and the 844 nm results, the presence of a stronger high energy tail which increases measured dissociation fraction is unlikely and would require significant electron populations with $E > 50\ eV$. Furthermore, similar disagreement between 777 nm and 844 nm results which include dissociative excitation, and likely constitute a variety of different EEDFs, have been observed in previous work [85–88]. Thus, the observed disagreement is unlikely to have been caused by uncertainty related to EEDFs and it seems that the disagreement exists for a wide range of possible EEDFs and there-

fore can only be accounted for by the inclusion of an additional mechanism, such as the metastable route proposed here. However, it is noted that like most OES methods, the accuracy of our resulting plasma parameters such as dissociation fraction, electron temperature and electron density strongly depend on the questionable accuracy of the cross sections, EEDFs, and other rates used for this work and thus contain significant uncertainty, beyond the experimental uncertainty given in figures, until further validation can be performed.

Table 6. Populating processes and radiative transitions considered for this work; cross section references are given for excitation rates. The index i refers to the oxygen state of interest and is replaced by the appropriate term symbol in the text, while the index j refers to arbitrary oxygen states with $j \neq i$, except in the case of the oxygen dissociation reaction, in which both fragments could potentially be the same state.

Argon		
symbol	reaction	ref.
$k_e^{4p'}$	$\mathrm{Ar}(3p^6\ {}^1S) + e^- \rightarrow \mathrm{Ar}\left(4p'\ {}^2\left[{}^1/_2\right]_0\right) + e^-$	[90]
A_{750}	$\mathrm{Ar}\left(4p'\ {}^2\left[{}^1/_2\right]_0\right) \rightarrow \mathrm{Ar}\left(4s'\ {}^2\left[{}^1/_2\right]_1^\circ\right) + \mathrm{h}\nu(750.4\ nm)$	[33]
Oxygen		
symbol	reaction	ref.
k_e^i	$\mathrm{O}(2p^4\ {}^3P) + e^- \rightarrow \mathrm{O}_i + e^-$	[7]
k_{de}^i	$\mathrm{O}_2 + e^- \rightarrow \mathrm{O}_i + \mathrm{O}_j + e^-$	[64, 91]
k_{csc}^i	$\mathrm{O}(2p^4\ {}^3P) + e^- \rightarrow \mathrm{O}_i + e^- + \Sigma_j \gamma$	[7, 89],Table 9
k_{em}	$\mathrm{O}(3\mathrm{s}\ {}^5\mathrm{S}^\circ) + e^- \rightarrow \mathrm{O}(3\mathrm{p}\ {}^5\mathrm{P}) + e^-$	[18]
A_{616}	$\mathrm{O}(4\mathrm{d}\ {}^5\mathrm{D}^\circ) \rightarrow \mathrm{O}(3\mathrm{p}\ {}^5\mathrm{P}) + \mathrm{h}\nu(615.7\ nm)$	[33]
A_{777}	$\mathrm{O}(3\mathrm{p}\ {}^5\mathrm{P}) \rightarrow \mathrm{O}(3\mathrm{s}\ {}^5\mathrm{S}^\circ) + \mathrm{h}\nu(777.4\ nm)$	[33]
A_{844}	$\mathrm{O}(3\mathrm{p}\ {}^3\mathrm{P}) \rightarrow \mathrm{O}(3\mathrm{s}\ {}^3\mathrm{S}^\circ) + \mathrm{h}\nu(844.6\ nm)$	[33]
Molecular Nitrogen		
symbol	reaction	ref.
$k_e^{(X-C)}$	$\mathrm{N}_2(\mathrm{X}^1\Sigma_\mathrm{g}^+) + e^- \rightarrow \mathrm{N}_2(\mathrm{C}^3\Pi_\mathrm{u})_{v=0} + e^-$	[40]
$k_e^{(X-B)}$	$\mathrm{N}_2(\mathrm{X}^1\Sigma_\mathrm{g}^+) + e^- \rightarrow \mathrm{N}_2^+(\mathrm{B}^2\Sigma_u^+)_{v=0} + 2e^-$	[1, 40, 92]
$k_e^{(Xp-B)}$	$\mathrm{N}_2^+(\mathrm{X}^1\Sigma_g^+) + e^- \rightarrow \mathrm{N}_2^+(\mathrm{B}^2\Sigma_u^+) + e^-$	[93]
A_{380}	$\mathrm{N}_2(\mathrm{C}^3\Pi_\mathrm{u})_{v=0} \rightarrow \mathrm{N}_2(\mathrm{B}^3\Pi_g)_{v=2} + \mathrm{h}\nu(380.4\ nm)$	[1]
A_{391}	$\mathrm{N}_2^+(\mathrm{B}^2\Sigma_u^+)_{v=0} \rightarrow \mathrm{N}_2^+(\mathrm{X}^1\Sigma_g^+)_{v=0} + \mathrm{h}\nu(391.4\ nm)$	[1]

V. Spectroscopic Characterization of a Supersonic Microwave Discharge

The final focus of this work regards the application of the knowledge gained and techniques developed in chapters III and IV to a bench top laboratory supersonic flowing discharge which can be seen as a basic laboratory model of high-Mach vehicles plasma sheath, similar to the laboratory modeling of atmospheric reentry of previous work [42]. Indeed the highly ionized and dissociated nature of the discharge along with the supersonic velocities capture many of the fundamental characteristics of these environments. Though these laboratory models differ in many ways from operational environments, such as the fact that discharge is driven electronically rather than by heating and gas-kinetics, they offer an investigative medium which would otherwise be significantly cost-prohibitive in most cases. In the sections that follow, the application of OES techniques similar to those used in chapter IV is investigated for the case of a supersonic flowing discharge and by extension the potential feasibility of using such methods in the plasma sheath of a high Mach vehicle.

5.1 Experimental Setup

The basis of the setup used for this work is a blown quartz tube with a 2 mm throat de Laval nozzle at its approximate center placed through a WR340 microwave waveguide, with the convergent section of the nozzle just upstream from the waveguide. On the downstream side of the nozzle, vacuum is provided by 3 rough pumps having a combined pump rate of approximately 20 m^3/hour and buffered by a 0.20 m^3 chamber which attains an ultimate pressure of approximately 1 mTorr with the aid of a turbo-molecular pump. On the inlet side of the nozzle, a 200 SCCM full scale mass flow controller and a 140 SCCM mass flow controller provide air and argon, respectively. For all results presented below the air flow is set to 200 SCCM while the argon is included at 10 SCCM (95% Air, 5% Argon). The mass flow controllers are separated by a small volume from a fast solenoid vacuum

valve with an open time of approximately 50 ms, which is incident upon the quartz tube and contained nozzle. A 6 KW 2.54 GHz magnetron excites the discharge and operates at approximately 600 Watts of absorbed power. To aid ignition of the discharge, a UV lamp is placed near the bottom of the waveguide. A copper plate terminates the waveguide, but contains a vertical cutout where the only microwave shielding is a copper mesh, which allows full viewing of the discharge tube. This copper mesh does influence the imaging as discussed in section 5.2 below. The resulting emission is imaged upon a 1/2 meter spectrograph with an Andor iStar 334t ICCD detector. A schematic of the full experimental setup is given in figure 19

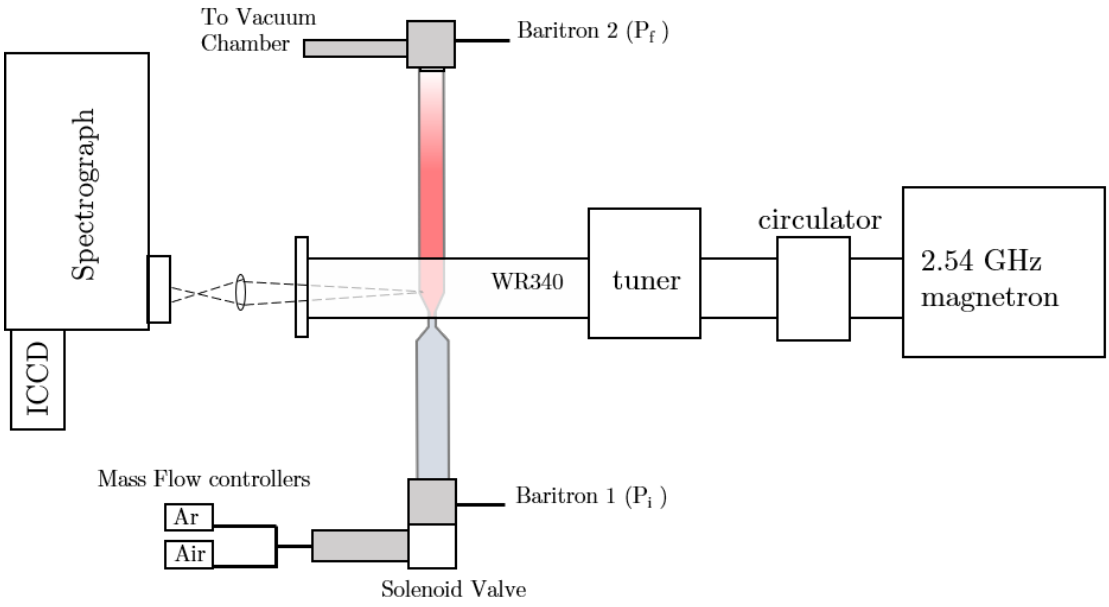

Figure 19. General experimental setup of microwave discharge and OES instrumentation

The design Mach number of the nozzle is M= 3.4 and is based on isentropic flow relation given in equation 14, at Mach 3.4, equation 14 yields a ratio of $A/A^* \approx 6.5$. Due to the flow limitations of our vacuum pumps, a relatively small throat diameter is chosen. Based on this consideration and the design area ratio, the throat diameter was fabricated at $D^* = 2$ mm and the exit diameter was subsequently fabricated at D= 5 mm. Using a similar isentropic relation, the expected pressure ratio as measured experimentally can be

estimated as $P_i/P_f \approx 71$. The designed profile of the nozzle is given if figure 20, though the actual profile consists of more continuous and rounded changes in diameter due to the glass blowing process. Figure 21 shows the actual nozzle with and its approximate profile. The overall profile is achieved by fusing several small quartz tubes together which have different diameters which correspond to the tube, throat, and exit diameters. An important difference in design and actual nozzle profile is the steep exit angle as the divergent section approaches a diameter of 5 mm. Because the exit angle of the nozzle is steep (approximately 80 degrees) and significantly greater than the an appropriate Prandtl-Meyer angle, it is expected that the flow separates from the tube wall and effectively is a free expansion until further downstream where the supersonic flow meets the wall. This situation is complex and given the unique profile would likely require the application of computational fluid dynamics (CFD) to properly solve. Further, if the non-isentropic effects caused by the incident microwave power were also considered the problem may even require treatment beyond standard CFD tools. Such studies of this complex flow are outside of the scope of this work and thus descriptions of flow mechanics are largely limited to predictions of Mach numbers based on measured pressure ratios.

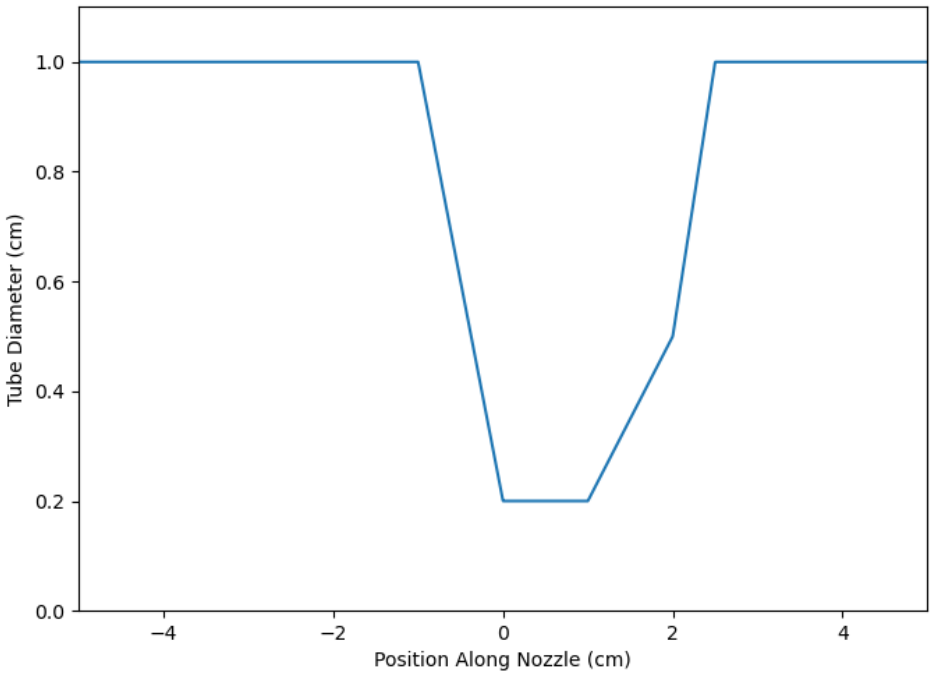

Figure 20. Designed Nozzle Profile

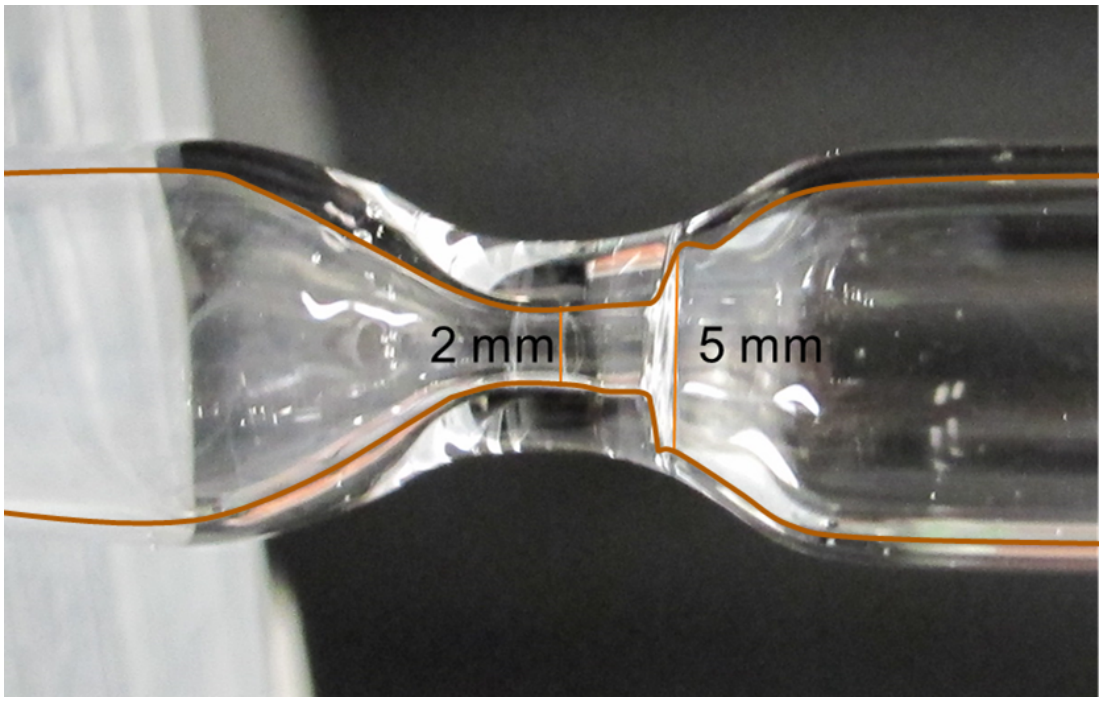

Figure 21. Actual approximate Nozzle Profile

5.2 Results

Figure 22 below shows an example of the pressures measured using the two Baratrons as shown in figure 19 as well as their ratio. The microwave power is incident until approximately 3.75 seconds when it is turned off; the solenoid valve initiates the flow near t=0 seconds. The flat portion of the curve represents pressures outside of the measureable range for the combined Baratron and oscilloscope acquisition setup. After the saturation period, 3 distinct flow regimes exist, which are separated by vertical dotted lines in figure 22. The first regime, from 0.5 to 1.3 seconds, corresponds to the discharge igniting but being limited to beyond the throat and downstream. The second regime, 1.3 to 2.8 seconds, corresponds to the discharge existing in both the throat and the downstream tube. The third regime, $t > 3.6$ s, corresponds to the discharge being off. In the first and third cases the pressure ratio is approaching a value of approximately 10, while in the second case has a pressure ratio greater than 20. These ratios are significantly lower than the design pressure ratio as in equation 15, which predicted a ratio near 71 for a Mach 3.4 flow. This result is likely primarily due to the flow being under-expanded and separated from the tube wall as discussed above. Additionally, the discharge seems to be contributing strongly to the flow conditions, as evidenced by the two unique flow regimes, as discussed further below in section 5.2.

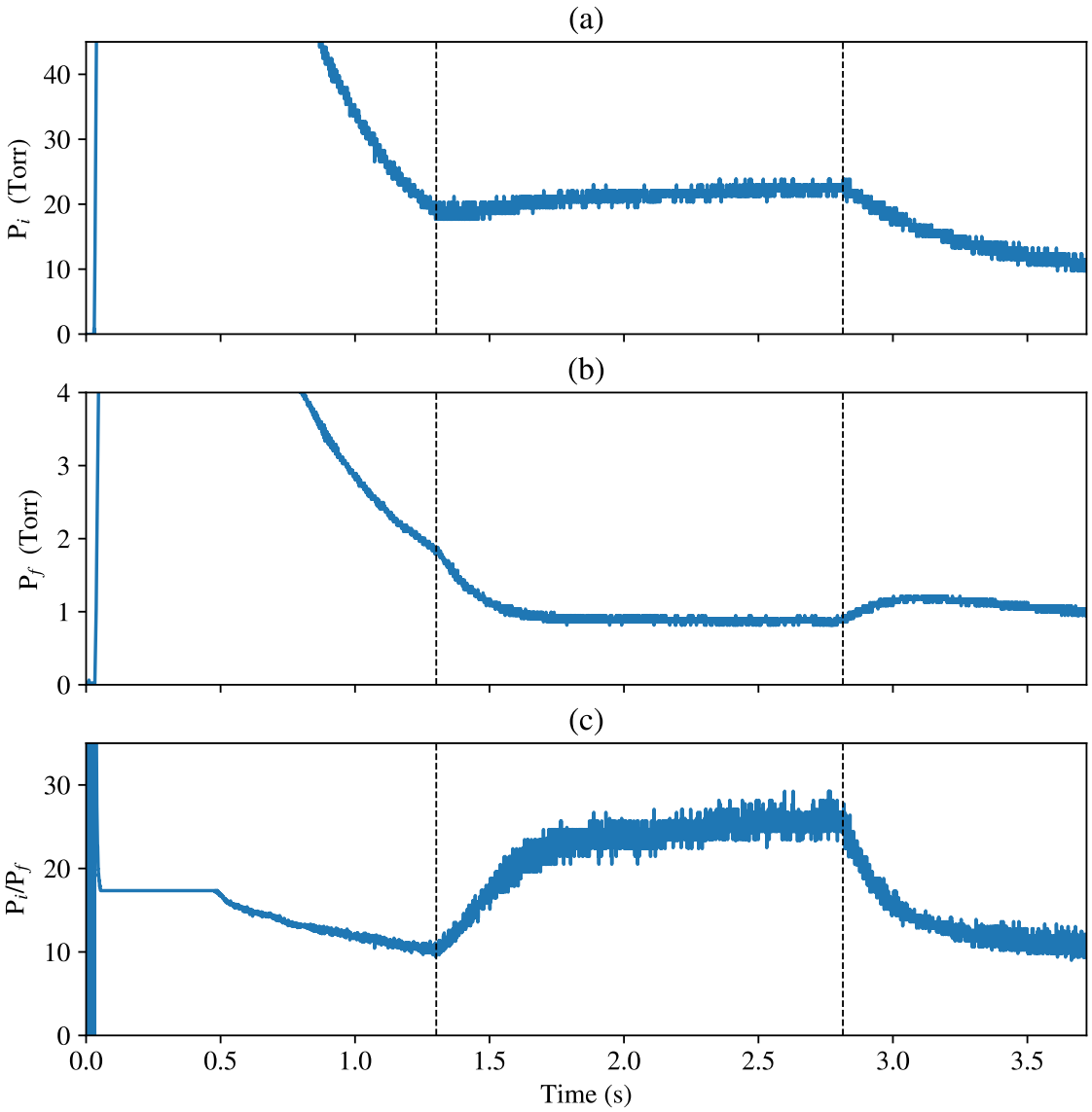

Figure 22. Time dependence of upstream (A) and downstream pressures (B), as well as the pressure ratio (C), for a typical discharge on and valve opening pulse.

Atomic Oxygen Imaging.

In order to capture the spatial distribution of the discharge as a function of time, a spectroscopic imaging system was used which uses optical band-pass filters which were custom fabricated to specifically image three atomic oxygen lines, namely the two strong 777 nm and 844 nm lines as well as the weaker 616 nm. The optical setup is similar to the

general setup in figure 19 with the addition of the appropriate optical filter. The imaging was performed through the spectrometer, with the slit opened fully and the grating at its zeroth order position acting effectively as a mirror. This method was chosen to minimize changes in the setup between acquisitions and calibrations which used spectrally dispersed images and those which were direct filtered images with horizontal spatial resolution, as in the oxygen line images shown and discussed below. The two strong infrared oxygen lines (777 nm and 844 nm) are particularly good candidates for spectroscopic imaging as they are among the strongest lines in the entire optical spectra of air and additionally carry strong dependence on important plasma parameters. Figures 23 and 24 show examples of the 3 discrete spectral lines as imaged during the first and second flow regimes, as discussed above. Images were collected as kinetic series for 3 separate experiments each having one of the 3 Oxygen line filters in place. The camera gating was provided to an oscilloscope in order to synchronize the pressure measurements with the imaging data. Figure 23 below shows an example of the emission distribution for each of the lines, and corresponds to the first regime where the discharge is more diffuse and limited to the section downstream from the throat. It is noted that the presence of a copper mesh over the window introduces strong artifacts in some of the data which can be seen as periodic structure in both the radial and axial dimensions. This structure is most apparent in figure 25 and does not reflect actual variation in the discharge structure. One noticeable real feature is the somewhat asymmetric distribution of the emission in the first flow regime, and the existence of a darker region on the right side of the tube. This region may correspond to the supersonic jet region, as the exit of the nozzle has a diameter similar to the size of the darkened region. The discharge ignites as shown in figure 23 when the pressure measured by the downstream Baratron falls to an average of approximately 6.5 Torr. Previous work using this microwave source as a stationary discharge consisting of a nearly identical setup showed that the discharge fails to ignite for pressures above approximately 3 Torr. This suggests that the actual pressure in

the ignited region is likely approximately half of the pressure as measured downstream.

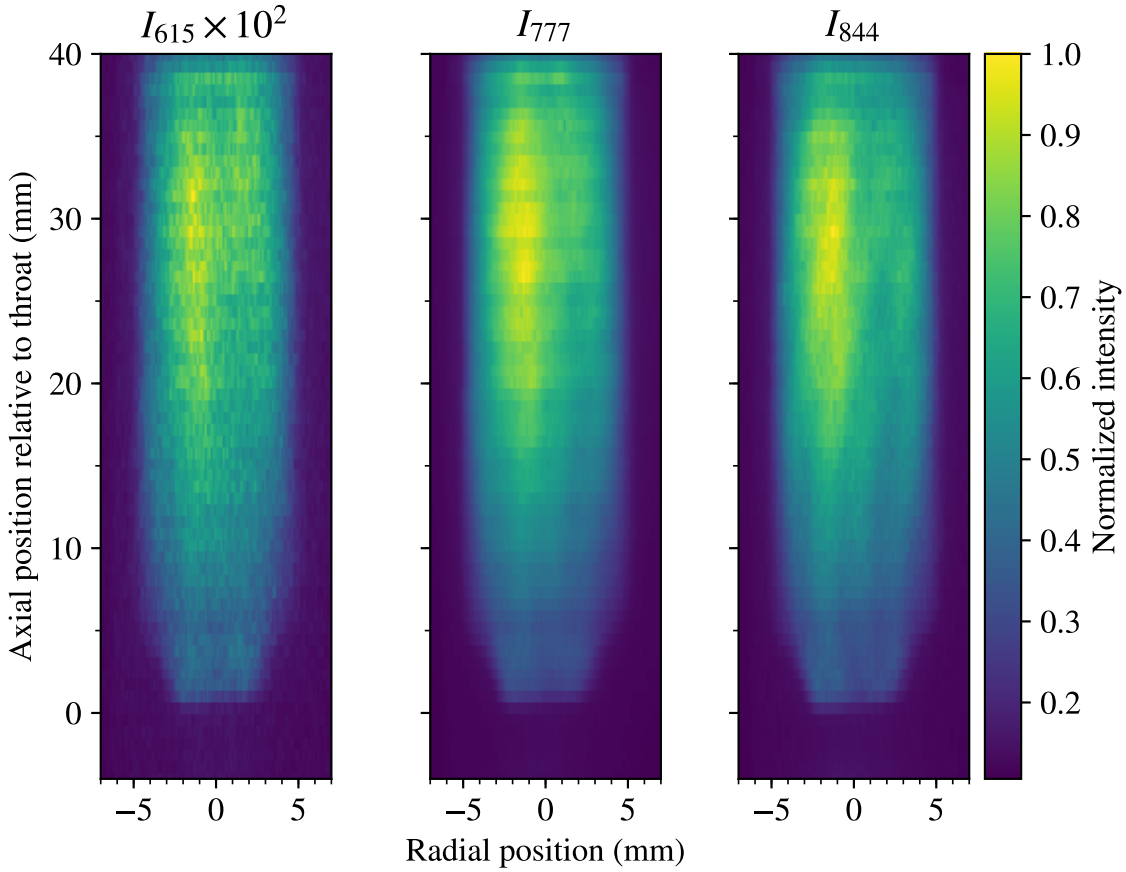

Figure 23. Excited Oxygen Spectroscopic images integrated from 0.7 to 0.95 seconds

The most interesting result of these images and the pressure data is the drastic change in upstream and downstream pressures as well as the resulting pressure ratio when the throat of the discharge ignites, as show in figure 24. This would suggest that the discharge at the throat significantly controls the flow as the pressure ratio increases to nearly double that of previous times. In the case which the plasma is formed in the nozzle throat, the strongly heated discharge acts as an obstacle for the cold flow which creates a pressure increase and velocity decrease before the throat [107]. Thus fewer particles enter the nozzle region and flow downstream [107]. Additionally, as boundary layer thickness is dependent on gas temperature (via viscocity), changes in local gas temperature caused by the local differences in microwave energy deposition into the plasma create dynamic boundary layers [107]. These two effects can be seen as responsible for the changes in pressure ratio for the different discharge regimes as well as contributing to the departure of the pressure ratio from that of the designed operating ratio and are directly related to the topic of plasma flow control applications which exploit similar effects, such as boundary layer modification [108]. Also observable in figure 24 is the clear appearance of a jet exiting the nozzle which appears to approach the same path as the darker region near +2 mm as observed in figure 23. The length of the flow for which the velocity is supersonic beyond the throat exit (or the location of the shock), can be estimated using the experimentally determined empirical relationship $z_s = 0.67 d_{ex}\sqrt{P_f/P_i}$ [53], where z_s is the location of the shock relative to the exit plane and d_{ex} is the exit diameter. For a pressure ratio of $P_f/P_i = 20$ and a 5 mm exit diameter, the supersonic region extends to approximately 10 mm, this distance corresponds to the approximate characteristic length of the jet in figure 24.

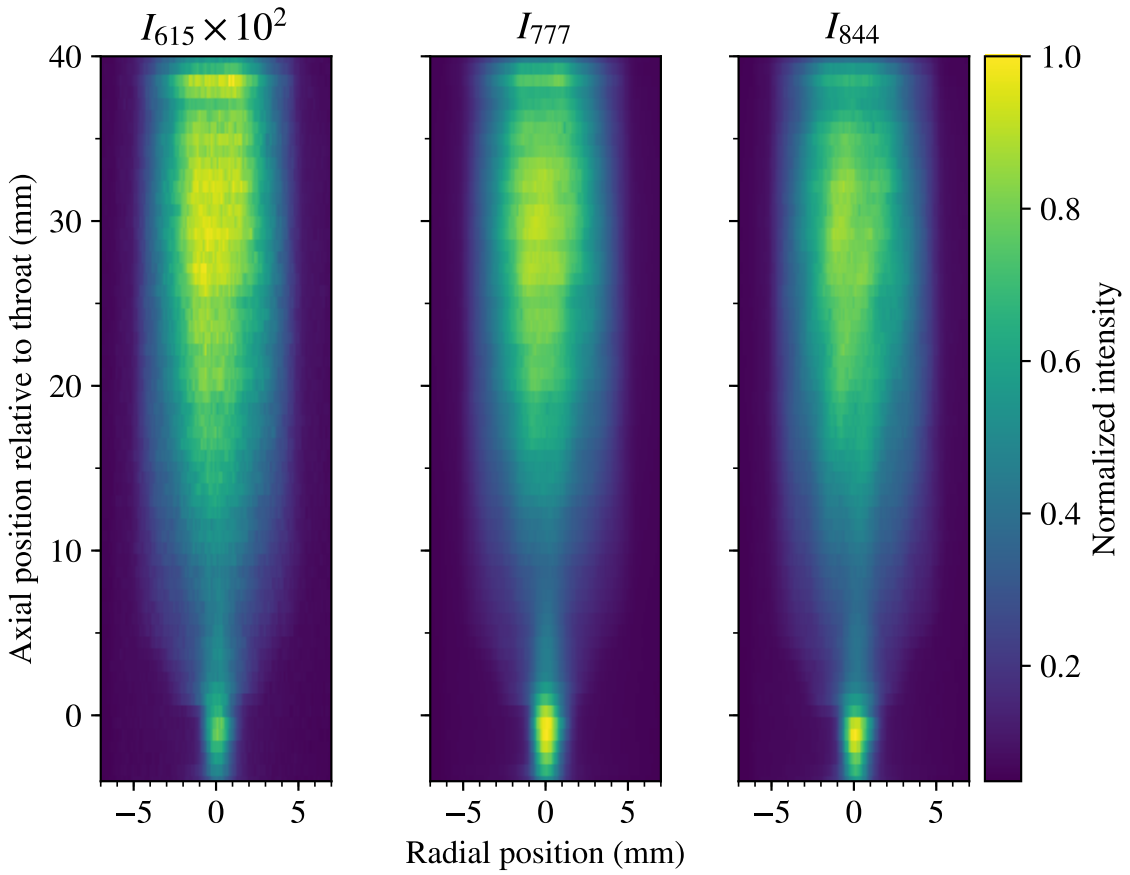

Figure 24. Excited Oxygen Spectroscopic images integrated from 2.0 to 2.5 seconds

Using the results of figure 24, a calibrated ratio of 777 nm to 844 nm lines can be found, as discussed in great length in chapter III. This ratio is given in figure 25. It is possible, based on the results of chapters III and IV, to develop an approximate analytical form of the line ratio in figure 25 which gives insight into its physical meaning. If it is assumed that the dissociation fraction in the case of the supersonic flow is near that of the subsonic case as measured in chapter IV (53%) , production of 3p ^{5}P and 3p ^{3}P by dissociative excitation accounts for a small percentage of the total production ($< 10\%$), and therefore can be reasonable ignored as an approximation. In this case the line ratio can be expressed as

$$\frac{I_{777(O)}}{I_{844(O)}} \approx \frac{P_{750}}{P_{844}} \left[\frac{n_O(k_e^{5P}) + n_{5S} k_{em}^{5P}}{n_O(k_e^{3P})} \right], \tag{43}$$

where k_e includes the cascade rate. As the dissociative excitation for production of 3s ^{5}S$^\circ$ was also small in chapter IV, at a branching of approximately 6.7%, its steady state density can be approximated as

$$n_{5S} \approx \frac{n_O n_e k_e^{5S}}{N k_q^{5S}}, \tag{44}$$

where N is the gas number density and k_q^{5S} is the total effective quenching rate. Substituting equation 44 into equation 43, the ratio is

$$\frac{I_{777(O)}}{I_{844(O)}} \approx \frac{P_{777}}{P_{844}} \left[\frac{k_e^{5P} + n_e k_e^{5S} k_{em}^{5P} / (N k_q^{5S})}{k_e^{3P}} \right], \tag{45}$$

thus for a given EEDF, the line ratio is proportional to the ionization fraction of the discharge, n_e/N. In the case where both the local EEDF and the local gas density are known, figure 25 could be converted to an approximate map of electron density. Additionally, if variation in local EEDF is small, figure 25 is in fact proportional to ionization fraction. Though, because it is expected that the number density is dynamic along the flow, it's reasonable to assume that EEDFs are also dynamic, as they depend directly on E/N. However if coupled with the N_2/N_2^+ or similar method as was done in chapter IV, the two techniques together could provide a powerful combined tool for direct imaging of electron density. A similar approach is briefly explored in the following section.

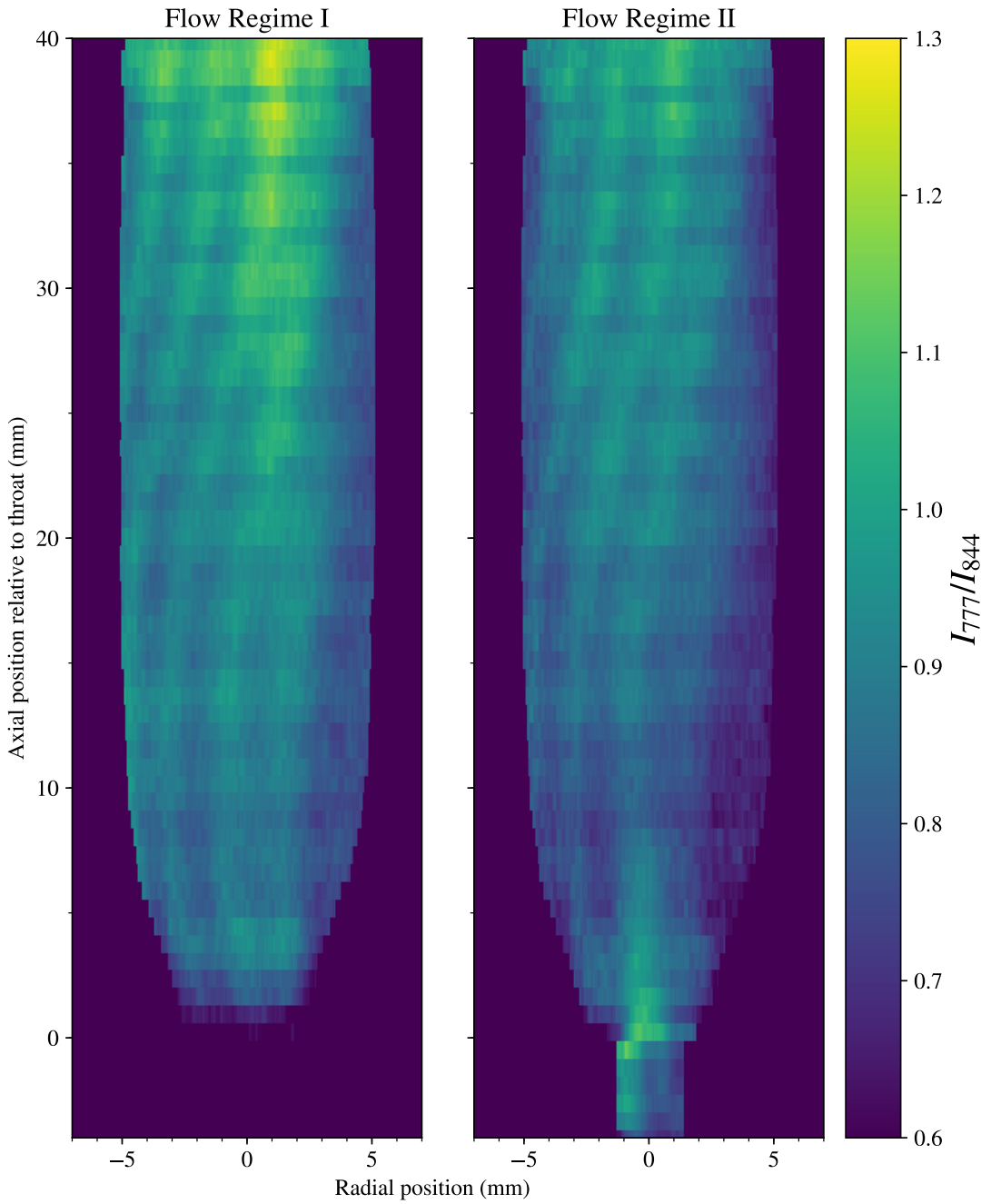

Figure 25. Imaged intensity ratio of 777 nm and 844 nm lines for the diffuse flow regime (I), near t=1.0 seconds and for the regime which has the throat ignited (II), near t=2.0 seconds. Note that the periodic structure in both dimensions is due to copper mesh covering window.

N_2 and Argon Spectra.

Similar results were obtained for the ΔV=2 bands of the $N_2(C-B)$ (365 nm to 380 nm) as well as the spectrum near 750 nm which contains the $4p'^{\,2}\left[{}^1/_2\right]_0 \rightarrow 4s'^{\,2}\left[{}^1/_2\right]_1^\circ$ argon line as well as the 3p $^4S^\circ \rightarrow$ 3s ^4P triplet nitrogen triplet, though rather than the filtered spectral imaging presented above, the center of the nozzle and discharge tube was imaged onto the spectrometer slit and the horizontal camera axis provided spectral resolution while the vertical axis gives axial spatial resolution of the discharge. Figure 26 below shows the total integrated intensity of the first three ΔV=2 bands as well as the argon and nitrogen lines as a function of position from the nozzle. These results were obtained in a flow situation similar to the second flow regime as discussed above, though they were integrated over approximately 3 seconds. If strong variations in the electron energy distribution function (EEDF) and subsequent electron excitation rates along the flow axis are neglected, the total integrated $N_2(C-B)$ emission as in figure 26 can be approximated as directly proportional to the product of electron density and gas number density. All of the lines have a strong maximum near the throat exit which sharply declines to a minimum near 7 mm and then make a gradual recovery along the tube, likely reflecting the recovery in pressure far downstream from the nozzle. With regard to the atomic nitrogen emission, the line carries an intensity relative to the argon intensity similar to that of the subsonic flow in chapter IV, suggesting that N_2 remains similarly dissociated. The ratio of nitrogen 747 nm emission to that of the $N_2(C-B)$ ΔV=2 bands increases nearly linearly from 2 to 25 mm, which could suggest that the dissociation fraction increases along the flow.

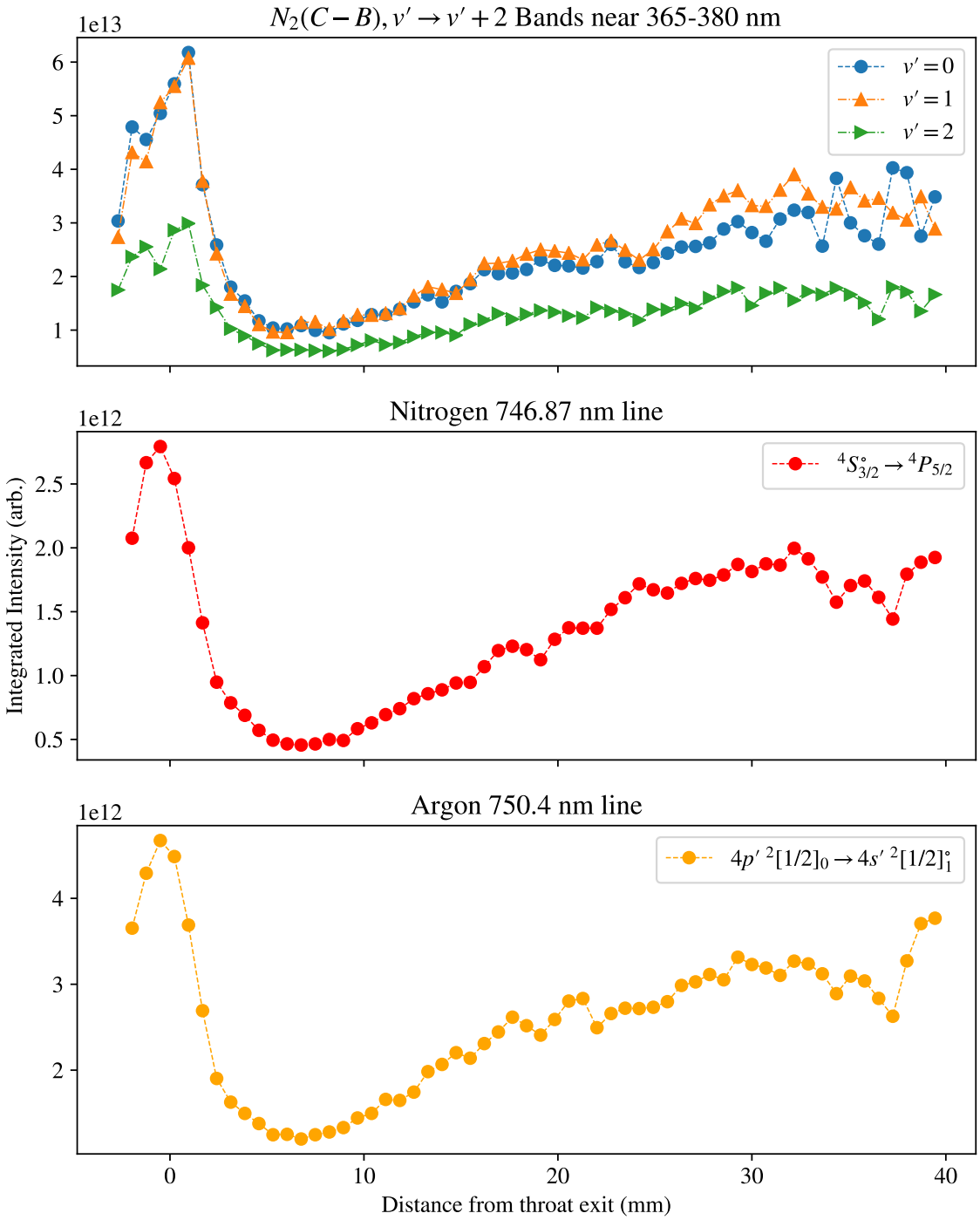

Figure 26. Axial spatial distribution of (a), the total integrated intensity of the ΔV=2 bands of the $N_2(C-B)$ and (b), the fraction of the total $N_2(C-B)$,ΔV=2 emission from the $v\prime \rightarrow v\prime\prime = 0 \rightarrow 2$.

Figure 27 below shows 3 examples of the near UV $N_2(C-B)$, ΔV=2 spectrum for positions corresponding to (a) the emission maximum along the axis or within the throat, (b)

at the emission minimum beyond the throat, and (c) far downstream. There are two readily apparent changes in these spectra. First, the fraction of the ΔV=2 emission arising from $v' = 1'$ decreases slightly by about 6 % from its initial relative value at the throat, this is apparent in the differences between figure 27 (a) and (b). This could be interpreted as either a shift in vibrational temperature of the N_2 ground state or a change in the excitation route of N_2(C). The second difference between the spectra are apparent changes in line-shape with the line-shape being broader near the nozzle. All have rotational temperatures near approximately 1500K for the least square fits performed for this work which had satisfactory residuals. It is worth noting that for these spectra, the best fit rotational temperature depends strongly on the line-shape function used to convolve the model, this is because the effect of lowering the rotational temperature results in changes to spectra which are similar to the changes caused by increasing the line-widths. Therefore, it is possible the changes in the spectra in figure 27 reflect a dynamic rotational temperature, though at the current time only satisfactory residuals are obtained by changing the line-shape. A calibration of the instrument line-shape using a mercury-argon lamp seemed to rule out any systematic or instrument based explanations for any increase or decrease in line-width along the spectrograph's vertical axis. One possible explanation is that the spectroscopic imaging system is not viewing the flow in an entirely perpendicular fashion and therefore the change in line-shape is due to velocity broadening. This seems unlikely, but could arise if the flow was turbulent.

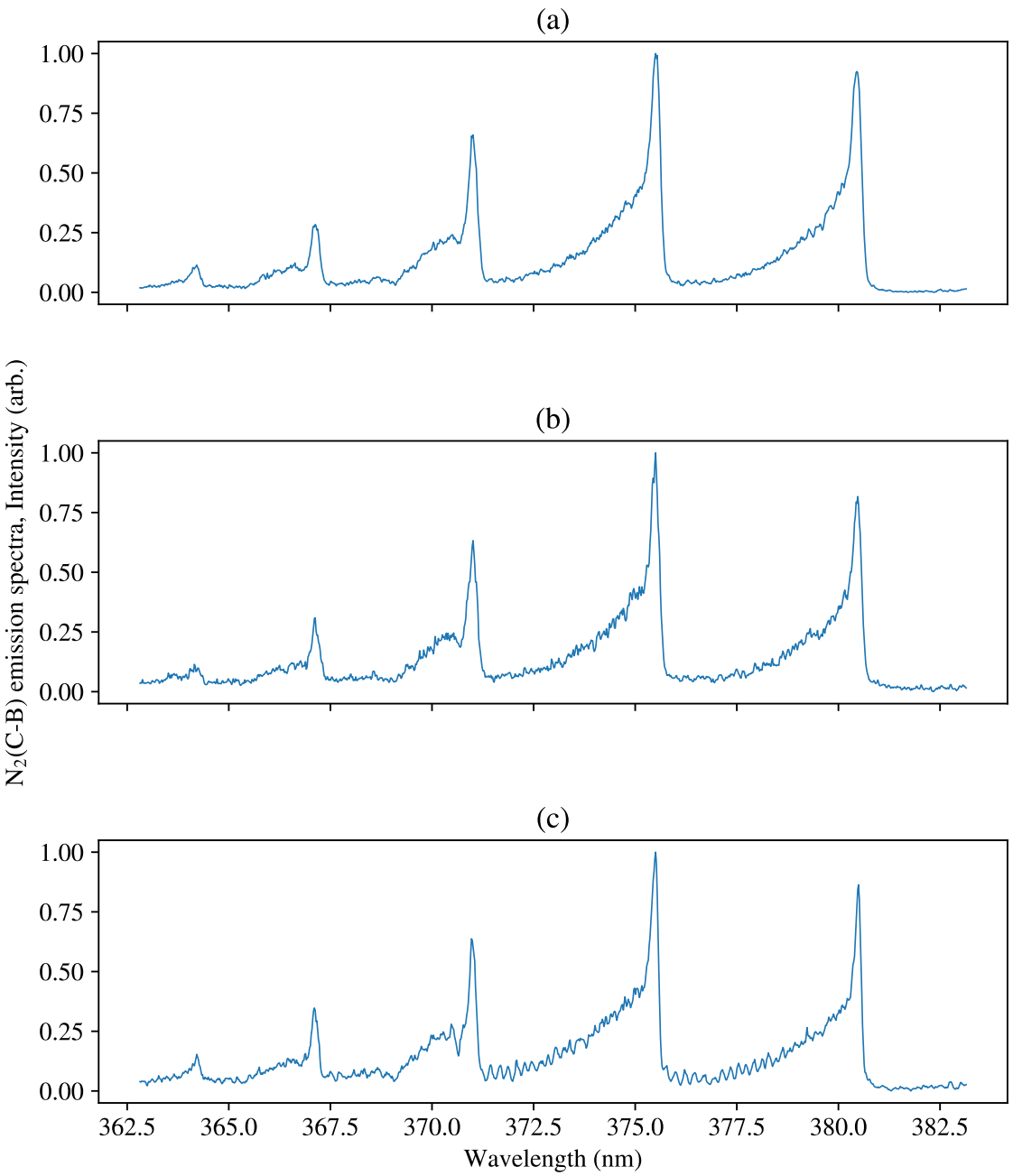

Figure 27. ΔV=2 spectrum of the $N_2(C-B)$ for three different axial positions: (a) at the throat, (b) at the emission minimum after the exit and (c) far downstream.

5.3 Estimation of Plasma Parameters

If as in chapter IV both the argon line and the $N_2(C-B), v' \rightarrow v'' = 0 \rightarrow 2$ band can be approximated using the corona model, their ratio can be used to estimate the electron temperature and associated EEDF. In that approximation, the ratio can be expressed as

$$\frac{I_{SPS}(v', v'')}{I_{750(Ar)}} = \frac{P_{SPS}(v', v'')}{P_{750}} \left[\frac{n_{N_2} k_e^{(X-C)}}{n_{Ar} k_e^{4p'}} \right]. \tag{46}$$

In this case the only unknown in equation 46 above is the EEDF used to calculation the excitation rate, and a similar procedure as used in section 4.4 can be used to determine a best fit EEDF. The ratio, $I_{SPS}(0,2)/I_{750}$, as taken from the intensities in figure 26, remains near approximately 10, though they are dynamic and tend to decrease from approximately 13 to 8.5, from 0 to 7 mm. These two ratios, 13 and 8.5, correspond to electron temperatures of 2.8 and 3.8 eV, respectively and suggest that the EEDF heats in the region just beyond the nozzle and settles near 3.75 eV after approximately 7 mm. This conclusion is however questionable for the many reasons, as discussed below.

It should be strongly noted, that this general procedure, of determining electron temperature using the corona model approximation of the $N_2(C^3\Pi_u)$ and Argon $4p'^{\,2}\left[{}^1/_2\right]_0$is potentially problematic for several reasons including the potential influence of metastables on both states by both stepwise excitation and the metastable pooling reaction for $N_2(C^3\Pi_u)$ production, as well as collisional quenching. The applicability of the method described above strongly depends on the densities of these metastables and its viability depends on electron density, electron temperature and neutral number density, all of which are difficult to determine in this dynamic flow. In the case of $N_2(C^3\Pi_u)$ in a stationary microwave discharge containing highly dissociated O_2 the argument has been made by Steves et al. [47] that collisional quenching of the $N_2(A^3\Sigma_u^+)$ metastable by atomic oxygen makes stepwise excitation of $N_2(C^3\Pi_u)$ from $N_2(A^3\Sigma_u^+)$ negligible, though no statement

regarding the commonly considered pooling reaction [40] was discussed. Additionally, $N_2(C^3\Pi_u), v = 0$ can be strongly produced by argon metastables [109]. Though this is not expected as in chapter IV the addition of a 5% total gas fraction of argon had a negligible influence on the N_2 spectra. The corona approximation (including quenching) for the $N_2(C^3\Pi_u), v = 0$, as used in the N_2/N_2^+ ratio technique in chapter IV is considered for this work a reasonable approximation (due to the above argument made by Steves et al. [47]), though it may contain some error associated with the $N_2(A^3\Sigma_u^+)$ metastable pooling reaction. However, in the case of the supersonic flow, the dynamic nature and unknown gas and plasma parameters make that extension questionable. Thus the electron temperature results discussed above could reflect changes in metastable densities as a result of reduced collisions in the supersonic flow rather than actual modifications of the EEDF. Indeed in the same region the $I_{SPS}(0,2)/I_{750}$ ratio is dynamic a change in the vibrational distribution of $N_2(C^3\Pi_u)$ is evident, with more density in higher vibrational states downstream. Despite this, they provide reasonable electron temperatures with an average of approximate 3.3 eV, though they are hotter than the results in chapter IV, which were closer to 2.5 eV, this is a reasonable outcome as those results were obtained outside the cavity where weaker electric fields are reasonably expected.

If it is assumed that the temperatures calculated above using the $I_{SPS}(0,2)/I_{750}$ ratio are a reasonable approximation, equation 43 can be used to estimate ionization fraction if rearranged as follows:

$$\frac{n_e}{N} \approx \frac{k_e^{5S} k_{em}^{5P}}{k_q^{5S}} \left[\frac{I_{777(O)}}{I_{844(O)}} \frac{P_{844}}{P_{777}} k_e^{3P} - k_e^{5P} \right]. \tag{47}$$

The line ratio, as given in figure 25 has a value of 1.05 at the throat exit and decreases to 0.9 near 7 mm. Using the electron temperature calculated above at those same locations, equation 47 yields dissociation fractions of $n_e/N = 1.75 \times 10^{-4}$ at z=0 mm and $n_e/N = 1.4 \times 10^{-4}$ at z = 7 mm. Equation 47 is not significantly sensitive to changes in electron

temperature for temperatures greater than approximately 2 eV, with the measured ionization fraction only decreasing by about 8% from 2 eV to 3 eV, therefore the electron procedure conducted would not significantly alter these results unless the actual temperatures were less than 2 eV. In any case, the estimation of electron temperature should be considered here as a potentially significant but necessary approximation in order to demonstrate the utility of the imaged 777 nm / 844 nm results and their relationship to equation 47, which is much less questionable based on the significant study conducted regarding the kinetics of those two lines in chapters III and IV.

5.4 Discussion

A supersonic microwave discharge was developed and operated at pressure ratios which corresponds to a Mach numbers ranging from 2.15 to 2.75. The variability of the Mach number is attributed to the modification of the flow by the discharge, such as by variable boundary layer thickness. Though the variability should be caused by variations in ratio of specific heat, k, as its value depends on the gas temperature and composition, the latter is likely dynamic due to varying degrees of dissociation. Nearly all spectra were at a maximum intensity at the throat exit and decayed rapidly until approximately 7 mm where an inflection point occurred. This likely indicates the location of the shock and is on the order of the approximation provided by the empirical formula from [53], which predicts a shock location of 10 mm. Rotational temperatures measured from the $N_2(C-B)$ here were near 1500 K and higher than the downstream temperatures measured by Drake et al. [20], wherein a similar supersonic microwave discharge flow was created. The rotational temperatures in that work was measured to be approximately 1150 K at a microwave power near 525 W, though in the case of Drake et al. [20] the gas mixture was dominantly argon with an approximately 5% and 9% admixture of H_2 and air, respectively.

With regard to the estimation of plasma parameters in section 5.3, two approximations

were made relative to the kinetic situation previously described in chapter IV, in order to reduce the ratio of the 777 nm / 844 nm into an analytical form useful for determining ionization fraction. First, dissociative excitation was neglected based on the low branching of that route ($< 10\%$) found for all EEDFs considered in chapter IV. Second, collisional quenching is ignored, which is an approximation made out of necessity due to the unknown local gas densities and temperatures. However, because the 777 nm and 844 nm lines have similar quenching rates for known values, the effect of including quenching on their ratio is small and less than our spectral calibration error. For example, including quenching at a pressure of 1 Torr and a temperature of 300 K only changes the ratio P_{844}/P_{777} by 3%, thus ignoring quenching is a reasonable approximation for this ratio. The situation is very similar for quenching and the $I_{SPS}(0,2)/I_{750}$ ratio, where inclusion of quenching at the same pressure and temperature changes the ratio of lifetimes by 4%. The other principal approximation made for calculation of electron temperatures use the N_2 / argon ratio was that electron excitation from the ground state is the dominant populating mechanism for both states, the questionable nature of this approximation was discussed in detail in section 5.3 above. Based on a these approximations, two simplified analytical equations were used to estimate electron temperature and ionization fraction for two locations. An average electron temperature of 3.3 eV was estimated along the flow and ionization fraction was estimated to be $n_e/N = 1.75 \times 10^{-4}$ near the throat (z=0 mm) and $n_e/N = 1.4 \times 10^{-4}$ downstream near the emission minimum (z=7 mm). For comparison, Kolesnichenko et al. [60] measured an electron density and gas temperature in a supersonic flow microwave discharge which corresponded to an ionization fraction of approximately 1.5×10^{-5}, though in the case of [60] microwave power was both significantly higher and pulsed for short durations (up to 2 μs). Additionally, in general, for high frequency discharges such as the microwave discharge used here are characterized by ionization fractions greater than approximately 10^{-5} [40]. In the subsonic case in chapter IV, the ionization fraction was measured to

be $n_e/N = 1.4 \times 10^{-4}$ which agrees well with values for the supersonic flow, which is somewhat expected as the value was measured using a very similar, though slightly more complete approach. In general ionization fraction is considered to be frozen in supersonic flows, as recombination is typically negligible in the expanded flow [107]. This is counter to what was estimated here in which a decrease of around 20% in ionization fraction was observed. It is not clear though, if this situation applies to flows in which energy is deposited in the supersonic region, as is the case here. One reasonable interpretation of the results is that the decrease in 777 nm / 844 nm reflects both a decrease in ionization fraction and electron temperature, since a decrease in electron temperature would decrease the electron-neutral collision frequency and subsequently the ionization rate. In this case the disagreement of this interpretation with the $I_{SPS}(0,2)/I_{750}$ ratio results could simply be seen as a divergence of the actual kinetic situation from the corona model in the supersonic flowing discharge for the reasons discussed in section 5.3 above. It is also possible that some of the changes of the 777 nm / 844 nm line ratio are indeed caused by changes in dissociation fraction, though for this to be a significant factor, it would require the actual dissociation fraction to be significantly lower than it was measured in chapter IV. In any case, the 777 nm / 844 nm imaging technique provides a reasonable estimate of ionization fraction and if properly validated could be extremely powerful for high temporal and spatial imaging of ionization fraction in highly dissociated plasma flows, though it remains to be proven that the ratio is indeed correlated to electron density.

VI. Conclusions

A 96-level collisional radiative model for atomic oxygen has been developed in order to test the validity of commonly used basic models for the 777 nm/ 844 nm line ratio. The model includes a relatively complete set of quenching or heavy particle collisional relaxation rates for a variety of common gas species for the first 6 excited states, dissociative excitation rates for the lowest 7 states, electron impact excitation rates for 96 excited states from the ground state and a complete electron impact excitation rate matrix for the lowest 7 states. Rates for electron processes are calculated using electron energy distribution functions calculated by BOLSIG [11] and using cross sections primarily from Laher and Gilmore [7], Barkelm [18] and Schulman et al. [64]. Computed line ratios are compared to both the basic model in literature which considers radiation, quenching, electron impact excitation from the ground state and dissociative excitation as well as the same basic model with the inclusion of a cascade emission populating rate. Comparisons are made for both a synthetic air mixture and an O_2/Ar mixture for a variety of oxygen dissociation fractions and gas pressures. It was determined that 3 factors account for the discrepancy between the collisional radiative model results and the basic model (1) metastable excitation, (2) cascade radiation, and (3) collisional quenching from 3p ^{3}P to 3p ^{5}P. Metastable excitation becomes dominant at low pressures for both gas mixtures and at low temperatures in the case of the O_2/Ar mixture. For all other situations cascade emission and collisional quenching from 3p ^{3}P to 3p ^{5}P account for nearly all disagreement between the 96 level collisional model and the basic model. At the present time, there is no simple way to include the effects of metastable excitation or collisional quenching from 3p ^{3}P to 3p ^{5}P without estimates of metastable densities and the density of the 3p ^{3}P state. Though the ground state and the ^{1}D and ^{1}S may be well approximated by a Saha equilibrium [61], higher lying states such as the 3s ^{5}S$^\circ$ state, which at low pressures can significantly populate the 3p ^{5}P state, exist in the active region which require a collisional-radiative model to accurately

estimate. However, inclusion of a cascade radiation rate, using the cross section calculated in this work and based on the electron impact excitation cross sections from Laher and Gilmore [7], does not over-complicate the basic model and can be implemented without additional knowledge. Additionally, inclusion of the cascade rate improves agreement with the collisional radiative model for all cases and in the case of a medium pressure air plasma it provides excellent agreement.

Finally, with regard to the CRM results, it was found that the 777 nm/ 844 nm line ratio has the most utility as an electron temperature or EEDF diagnostic at medium and high pressures (1-760 Torr) and for low dissociation fractions ($< 10\%$). Outside of this parameter space the line ratio is either not sensitive to moderate changes in electron temperature or too difficult to compute due to metastable excitation.

In the subsonic experimental investigation, strong evidence was provided that metastable excitation ($3s\,^5S^\circ \rightarrow 3p\,^5P$) is an important mechanism for accurately modeling the relative 777 nm oxygen line intensity in medium pressure microwave N_2/O_2 discharges and the addition of this mechanism introduces an electron density dependence to the 777 nm / 750 nm actinometry ratio which can be exploited along with other techniques to extract estimates of electron density. The additional mechanism is most important for low pressures and high electron densities as it depends the product of $O(3s\,^5S^\circ)$ and electron densities. This technique is enhanced by the fact that the extended corona model, which includes direct electron impact excitation from the ground state, cascade electron impact excitation and dissociative excitation can be extended to the $3s\,^5S^\circ$ metastable for the conditions observed here and shows excellent agreement with a relatively complete collisional radiative model, thus allowing for experimental determinations of electron and metastable $3s\,^5S^\circ$ densities using analytical solutions. On the basis of these conclusions, a combined technique which uses 2 oxygen / argon actinometry ratios (844 nm / 750 nm and 777 nm / 750 nm) with a corrected excitation scheme for the $3p\,^5P$ state along with the N_2/N_2^+ method has been

developed which can be used to simultaneously determine dissociation fraction, effective electron temperature, metastable 3s ^{5}S$^\circ$ density and an estimate of electron density. This combined actinometry technique however does require the three conditions (in addition to any general oxygen/argon actinometry requirements) for applicability: 1) metastable 3s ^{5}S$^\circ$ density is sufficiently high such that metastable excitation is significant for the 777 nm line, 2) collisional de-excitation is dominant loss mechanism for 3s ^{5}S$^\circ$ and 3) it is possible to resolve between the two possible solutions to electron temperature. This combined actinometry technique was shown to produce dissociation fractions, effective electron temperatures and electron densities reasonably consistent with those found in similar discharges in literature and O(3s ^{5}S$^\circ$) densities consistent with values predicted by a relatively complete collisional radiative model. In the case of the 4d ^{5}D$^\circ$ state, the lack of available quenching and metastable excitation rates make comparison of experimental results somewhat inconclusive, though results indicate that the 616 nm / 750 nm actinometry ratio is correlated to atomic oxygen density and when quenching is ignored the ratio produced dissociation fractions which nearly agreed with the more trustworthy 844 nm technique. These results indicate that the 616 nm line shows promise as an additional OES line and thus measurement of quenching rates for air collisional partners along with some estimation of metastable excitation for the 4d ^{5}D$^\circ$ state is strongly suggested for future work.

With regard to the final experiments conducted in chapter V, a supersonic flowing microwave discharge was achieved using a quartz de Laval nozzle and a high power 2.54 GHz magnetron. The resulting discharge was analyzed with a number of spectroscopic tools from within the waveguide cavity. Based on the results of chapters III and IV, a simple relationship between the common 777 nm / 844 nm and ionization fraction was developed and the ratio itself was imaged using narrow band interference filters to produce spatially resolved images which can be seen as a qualitative examination of the spatial dependence of ionization fraction. Ionization fraction was estimated near $n_e/N = 1.75 \times 10^{-4}$ at the

throat exit and $n_e/N = 1.4 \times 10^{-4}$ at a position 7 mm downstream. If local EEDFs and gas densities are determined, this image can be converted to an approximate map of electron density, though further validation of the spectroscopic model and required assumptions are required.

Finally, with regard to the general utility and accuracy of OES diagnostic techniques, such as the ones developed here and similar approaches, they certainly carry significant benefits over other techniques including their non-invasive, experimentally simple to apply approaches, as well as their high spatial and temporal resolution afforded by imaging methods. However, the primary trade-off is accuracy which depends strongly on the accuracy of cross sections, EEDFs, quenching coefficients and other spectroscopic data. In the case of cross sections, significant uncertainties exist and are evident by the variety of different cross sections for the same process from different authors. Similarly, modeling of EEDFs using BOLSIG and other Boltzmann solvers rely on the accuracy of these cross sections as well as other input parameters such as gas composition and densities of excited neutrals and ions as well as the overall validity of the two-term approximation. In addition to this, OES requires that the spectroscopic models be a good approximation of the kinetic situation and are not missing any non-negligible processes. For these reasons, OES applications typically require in-situ validation specific to their application in order to provide accurate results. In other cases, such as the OES results for electron densities, metastable densities and electron temperatures performed here, which have been not been verified with other diagnostics, results should be treated as somewhat qualitative in nature. Thus validation of the techniques presented here with more trustworthy and robust diagnostics is a necessary future step. However, this trade off in terms of accuracy can be worth the powerful nature of imaging techniques such as those used in chapter V which can capture plasma characteristics with high temporal and spatial resolution with a relatively simple an inexpensive acquisition setup. Thus, the optimal utility of these diagnostics exists in situations where

validation or calibration of accuracy is possible and situations which require high spatial and temporal resolution, simple experimental application, and non-invasive probing.

Appendix A: Cascade emission cross sections.

Cascade emission cross sections used in this work are given in table 9 below. These cross sections capture the excitation resulting from direct electron excitation to higher lying states and were calculated using the direct cross sections from Laher and Gilmore [7] and the recursive equations in chapter III, where a complete description is available.

Table 9. Cascade cross sections for important atomic oxygen states derived from the cross sections of [7]. Values for each are given in 10^{-18} cm^{-2}.

Energy (eV)	3s ^{5}S°	3p ^{5}P	3p ^{3}P	4d ^{5}D°
11.2	0.465	-	-	-
11.4	0.855	-	-	-
11.6	1.062	-	-	-
11.8	1.186	-	-	-
12.0	1.329	0.020	-	-
12.2	1.460	0.050	0.050	-
12.4	1.600	0.090	0.106	-
12.6	2.266	0.610	0.148	-
12.8	2.498	0.738	0.175	-
13.4	3.123	1.054	0.347	0.035
13.6	3.340	1.167	0.415	0.055
13.8	3.548	1.273	0.482	0.066
14	3.781	1.406	0.707	0.074
16	4.379	1.952	1.084	0.136
18	4.442	2.133	1.307	0.143
20	4.331	2.153	1.459	0.136
22	3.972	2.039	1.546	0.128
25	3.149	1.696	1.561	0.107
28	2.205	1.284	1.566	0.074
30	1.765	1.061	1.583	0.055
35	1.120	0.679	1.616	0.032
40	0.745	0.451	1.639	0.021
45	0.539	0.328	1.646	0.014
50	0.378	0.231	1.643	0.010
55	0.294	0.179	1.576	0.007
60	0.221	0.137	1.499	0.006
70	0.132	0.080	1.296	0.003
100	0.063	0.043	0.837	0.001
150	0.015	0.009	0.695	0.000
200	0.006	0.004	0.585	0.000

Bibliography

1. F. R. Gilmore, R. R. Laher, and P. J. Espy, "Franck–Condon Factors, r-Centroids, Electronic Transition Moments, and Einstein Coefficients for Many Nitrogen and Oxygen Band Systems," *Journal of Physical and Chemical Reference Data*, vol. 21, pp. 1005–1107, Sept. 1992. Publisher: American Institute of Physics.

2. K. Niemi, V. Schulz-von der Gathen, and H. F. Döbele, "Absolute calibration of atomic density measurements by laser-induced fluorescence spectroscopy with two-photon excitation," *Journal of Physics D: Applied Physics*, vol. 34, pp. 2330–2335, July 2001.

3. P. J. Dagdigian, B. E. Forch, and A. W. Miziolek, "Collisional transfer between and quenching of the 3p ^{3}P and ^{5}P states of the oxygen atom," *Chemical Physics Letters*, vol. 148, pp. 299–308, July 1988.

4. N. Sadeghi, D. W. Setser, A. Francis, U. Czarnetzki, and H. F. Döbele, "Quenching rate constants for reactions of Ar ($4p'\ [1/2]_0$, $4p\ [1/2]_0$, $4p\ [3/2]_2$, and $4p\ [5/2]_2$) atoms with 22 reagent gases," *The Journal of Chemical Physics*, vol. 115, pp. 3144–3154, Aug. 2001. Publisher: American Institute of Physics.

5. S. Pancheshnyi, "Comments on 'Intensity ratio of spectral bands of nitrogen as a measure of electric field strength in plasmas'," *Journal of Physics D: Applied Physics*, vol. 39, pp. 1708–1710, Apr. 2006.

6. G. Dilecce, P. F. Ambrico, and S. De Benedictis, "On the collision quenching of $N_2^+(B^2\Sigma_u^+, v = 0)$ by N_2 and O_2 and its influence on the measurement of E/N by intensity ratio of nitrogen spectral bands," *Journal of Physics D: Applied Physics*, vol. 43, p. 195201, May 2010.

7. R. R. Laher and F. R. Gilmore, "Updated Excitation and Ionization Cross Sections for Electron Impact on Atomic Oxygen," *Journal of Physical and Chemical Reference Data*, vol. 19, pp. 277–305, Jan. 1990.

8. I. Adamovich, S. D. Baalrud, A. Bogaerts, P. J. Bruggeman, M. Cappelli, V. Colombo, U. Czarnetzki, U. Ebert, J. G. Eden, P. Favia, D. B. Graves, S. Hamaguchi, G. Hieftje, M. Hori, I. D. Kaganovich, U. Kortshagen, M. J. Kushner, N. J. Mason, S. Mazouffre, S. M. Thagard, H.-R. Metelmann, A. Mizuno, E. Moreau, A. B. Murphy, B. A. Niemira, G. S. Oehrlein, Z. L. Petrovic, L. C. Pitchford, Y.-K. Pu, S. Rauf, O. Sakai, S. Samukawa, S. Starikovskaia, J. Tennyson, K. Terashima, M. M. Turner, M. C. M. v. d. Sanden, and A. Vardelle, "The 2017 Plasma Roadmap: Low temperature plasma science and technology," *Journal of Physics D: Applied Physics*, vol. 50, p. 323001, July 2017.

9. J. B. Boffard, C. C. Lin, and C. A. DeJosephJr, "Application of excitation cross sections to optical plasma diagnostics," *Journal of Physics D: Applied Physics*, vol. 37, pp. R143–R161, May 2004.

10. X.-M. Zhu and Y.-K. Pu, "Optical emission spectroscopy in low-temperature plasmas containing argon and nitrogen: determination of the electron temperature and density by the line-ratio method," *Journal of Physics D: Applied Physics*, vol. 43, p. 403001, Sept. 2010.

11. G. J. M. Hagelaar and L. C. Pitchford, "Solving the Boltzmann equation to obtain electron transport coefficients and rate coefficients for fluid models," *Plasma Sources Science and Technology*, vol. 14, pp. 722–733, Nov. 2005.

12. A. Tejero-del Caz, V. Guerra, D. Gonçalves, M. L. d. Silva, L. Marques, N. Pinhão, C. D. Pintassilgo, and L. L. Alves, "The LisbOn KInetics Boltzmann solver," *Plasma Sources Science and Technology*, vol. 28, p. 043001, Apr. 2019.

13. X. Gao and B. Jiang, "A matching approach to communicate through the plasma sheath surrounding a hypersonic vehicle," *Journal of Applied Physics*, vol. 117, p. 233301, June 2015. Publisher: American Institute of Physics.

14. A. O. Korotkevich, A. C. Newell, and V. E. Zakharov, "Communication through plasma sheaths," *Journal of Applied Physics*, vol. 102, p. 083305, Nov. 2007. Publisher: American Institute of Physics Publising LLC.

15. J. W. Marini, "On the decrease of the radar cross section of the Apollo Command Module due to reentry plasma effects," 1967.

16. R. L. Stenzel and J. M. Urrutia, "A new method for removing the blackout problem on reentry vehicles," *Journal of Applied Physics*, vol. 113, pp. 103303–103303–5, Mar. 2013.

17. C. Park, R. L. Jaffe, and H. Partridge, "Chemical-Kinetic Parameters of Hyperbolic Earth Entry," *Journal of Thermophysics and Heat Transfer*, vol. 15, no. 1, pp. 76–90, 2001. Publisher: American Institute of Aeronautics and Astronautics _eprint: https://doi.org/10.2514/2.6582.

18. P. S. Barklem, "Electron-impact excitation of neutral oxygen," *Astronomy & Astrophysics*, vol. 462, pp. 781–788, Feb. 2007.

19. Y. A. Lebedev, "Microwave discharges: generation and diagnostics," *Journal of Physics: Conference Series*, vol. 257, p. 012016, Nov. 2010. Publisher: IOP Publishing.

20. D. J. Drake, S. Popović, and L. Vušković, "Characterization of a supersonic microwave discharge in Ar/H2/Air mixtures," *Journal of Applied Physics*, vol. 104, p. 063305, Sept. 2008.

21. V. Lago, E. Barbosa, F. Passarinho, and J.-P. Martin, "Electron and vibrational temperatures in hypersonic co_2-n_2 plasma jets," *Plasma Sources Science and Technology*, vol. 16, pp. 139–148, Feb. 2007.

22. M. Nikolić, A. Samolov, F. Čučkov, S. Popović, L. Vušković, and A. Godunov, "Characterization of the supersonic flowing microwave discharge using two dimensional plasma tomography," *Journal of Applied Physics*, vol. 113, p. 103301, Mar. 2013. Publisher: American Institute of Physics.

23. K. V. Khodataev, "Microwave Discharges and Possible Applications in Aerospace Technologies," *Journal of Propulsion and Power*, vol. 24, pp. 962–972, Sept. 2008. Publisher: American Institute of Aeronautics and Astronautics.

24. Y. A. Lebedev, "Microwave discharges at low pressures and peculiarities of the processes in strongly non-uniform plasma," *Plasma Sources Science and Technology*, vol. 24, p. 053001, Aug. 2015. Publisher: IOP Publishing.

25. S. A. Gower, "Development of a high power microwave plasma beam applicator," 2001. Publisher: Research Online.

26. K. H. Becker, U. Kogelschatz, K. H. Schoenback, and R. J. Barker, *Non-Equilibrium Air Plasmas at Atmospheric Pressure*. Bristol and Philadelphia: Institute of Physics, 2005.

27. R. Schunk and A. Nagy, *Ionospheres*. Cambridge: Cambridge University Press, 2018.

28. J. Vlcek, "A collisional-radiative model applicable to argon discharges over a wide range of conditions. I. Formulation and basic data," *Journal of Physics D: Applied Physics*, vol. 22, pp. 623–631, May 1989.

29. M. A. Lieberman and A. J. Lichtenberg, *Principles of Plasma Discharges and Materials Processing*. Hoboken: Wiley, second edition ed., 2005.

30. J. B. Boffard, R. O. Jung, C. C. Lin, L. E. Aneskavich, and A. E. Wendt, "Argon 420.1–419.8 nm emission line ratio for measuring plasma effective electron temperatures," *Journal of Physics D: Applied Physics*, vol. 45, p. 045201, Feb. 2012.

31. R. Engeln, B. L. M. Klarenaar, and O. Guaitella, "Foundations of optical diagnostics in low-temperature plasmas," *Plasma Sources Science and Technology*, 2020.

32. P. F. Bernath, *Spectra of Atoms and Molecules*. New York: Oxford University Press, third edition ed., 2016.

33. A. Kramida and Y. Ralchenko, "NIST Atomic Spectra Database, NIST Standard Reference Database 78," 1999. type: dataset.

34. P. J. Bruggeman, N. Sadeghi, D. C. Schram, and V. Linss, "Gas temperature determination from rotational lines in non-equilibrium plasmas: a review," *Plasma Sources Science and Technology*, vol. 23, p. 023001, Apr. 2014.

35. S. Adams, J. Miles, T. Ombrello, R. Brayfield, and J. Lefkowitz, "The effect of interpulse coupling on gas temperature in nanosecond-pulsed high-frequency discharges," *Journal of Physics D: Applied Physics*, vol. 52, p. 355203, July 2019. Publisher: IOP Publishing.

36. S. F. Adams, J. E. Caplinger, and B. S. Sommers, "Spatial temperature mapping of an atmospheric microdischarge using ultraviolet Rayleigh scatter imaging," *Plasma Sources Science and Technology*, vol. 24, p. 025031, Apr. 2015. Publisher: IOP Publishing.

37. J. Caplinger, "Ultraviolet Rayleigh Scatter Imaging for Spatial Temperature Profiles in Atmospheric Microdischarges," *Browse all Theses and Dissertations*, Jan. 2014.

38. L. R. Ventura and C. E. Fellows, "The N_2 second positive ($C^3\Pi_u \rightarrow B^3\Pi_g$) system reviewed: Improved data and analysis," *Journal of Quantitative Spectroscopy and Radiative Transfer*, vol. 239, p. 106645, Dec. 2019.

39. R. R. Laher and F. R. Gilmore, "Improved Fits for the Vibrational and Rotational Constants of Many States of Nitrogen and Oxygen," *Journal of Physical and Chemical Reference Data*, vol. 20, pp. 685–712, July 1991.

40. P. Bílek, M. Šimek, and Z. Bonaventura, "Electric field determination from intensity ratio of N_2^+ and N_2 bands: nonequilibrium transient discharges in pure nitrogen," *Plasma Sources Science and Technology*, vol. 28, p. 115011, Nov. 2019.

41. A. H. Shapiro, *The Dynamics and Thermodynamics of Compressible Fluid Flow*, vol. Volume I. New York, Chichester, Brisbane and Toronto: John wiley & Sons, 1953.

42. S. Mazouffre and E. Pawelec, "Metastable oxygen atom velocity and temperature in supersonic CO2plasma expansions," *Journal of Physics D: Applied Physics*, vol. 42, p. 015203, Dec. 2008. Publisher: IOP Publishing.

43. Y. A. Lebedev and V. A. Shakhatov, "Diagnostics of a nonequilibrium nitrogen plasma from the emission spectra of the second positive system of N2," *Plasma Physics Reports*, vol. 32, pp. 56–71, Jan. 2006.

44. L. M. Isola, B. J. Gómez, and V. Guerra, "Determination of the electron temperature and density in the negative glow of a nitrogen pulsed discharge using optical emission spectroscopy," *Journal of Physics D: Applied Physics*, vol. 43, p. 015202, Jan. 2010.

45. D. Xiao, C. Cheng, J. Shen, Y. Lan, H. Xie, X. Shu, Y. Meng, J. Li, and P. K. Chu, "Electron density measurements of atmospheric-pressure non-thermal N_2 plasma jet

by Stark broadening and irradiance intensity methods," *Physics of Plasmas*, vol. 21, p. 053510, May 2014.

46. S. Keller, P. Rajasekaran, N. Bibinov, and P. Awakowicz, "Characterization of transient discharges under atmospheric-pressure conditions applying nitrogen photoemission and current measurements," *Journal of Physics D: Applied Physics*, vol. 45, p. 125202, Mar. 2012.

47. S. Steves, T. Styrnoll, F. Mitschker, S. Bienholz, B. Nikita, and P. Awakowicz, "Characterization of low-pressure microwave and radio frequency discharges in oxygen applying optical emission spectroscopy and multipole resonance probe," *Journal of Physics D: Applied Physics*, vol. 46, p. 445201, Nov. 2013.

48. R. Pothiraja, C. Ruhrmann, M. Engelhardt, N. Bibinov, and P. Awakowicz, "Characterization of atmospheric-pressure ac micro-discharge in He–N_2 mixture using time- and space-resolved optical emission spectroscopy," *Journal of Physics D: Applied Physics*, vol. 46, p. 464012, Nov. 2013.

49. E. J. H. Collart, J. a. G. Baggerman, and R. J. Visser, "Excitation mechanisms of oxygen atoms in a low pressure O2 radio-frequency plasma," *Journal of Applied Physics*, vol. 70, pp. 5278–5281, Nov. 1991. Publisher: American Institute of Physics.

50. T. Tsutsumi, A. Greb, A. R. Gibson, M. Hori, D. O'Connell, and T. Gans, "Investigation of the radially resolved oxygen dissociation degree and local mean electron energy in oxygen plasmas in contact with different surface materials," *Journal of Applied Physics*, vol. 121, p. 143301, Apr. 2017.

51. A. Greb, K. Niemi, D. O'Connell, and T. Gans, "Energy resolved actinometry for simultaneous measurement of atomic oxygen densities and local mean electron ener-

gies in radio-frequency driven plasmas," *Applied Physics Letters*, vol. 105, p. 234105, Dec. 2014.

52. V. Milosavljević, N. MacGearailt, P. J. Cullen, S. Daniels, and M. M. Turner, "Phase-resolved optical emission spectroscopy for an electron cyclotron resonance etcher," *Journal of Applied Physics*, vol. 113, p. 163302, Apr. 2013.

53. S. Caldirola, R. Barni, and C. Riccardi, "Characterization of a low pressure supersonic plasma jet," *Journal of Physics: Conference Series*, vol. 550, p. 012042, Nov. 2014. Publisher: IOP Publishing.

54. M. E. Morsli and P. Proulx, "A chemical non-equilibrium model of anairsupersonic ICP," *Journal of Physics D: Applied Physics*, vol. 40, pp. 380–394, Jan. 2007. Publisher: IOP Publishing.

55. A. S. Boreisho, M. Y. Vovk, A. D. Edigarev, I. A. Kiselev, V. V. Kulalaev, A. V. Morozov, A. E. Orlov, and P. G. Smirnov, "Combustion-driven gas-dynamic CO2-laser on the basis of modern aviation engines," *Journal of Physics: Conference Series*, vol. 1565, p. 012021, June 2020. Publisher: IOP Publishing.

56. A. Broc, S. D. Benedictis, and G. Dilecce, "LIF investigations on NO, O and N in a supersonic N2/O2/NO RF plasma jet," *Plasma Sources Science and Technology*, vol. 13, pp. 504–514, July 2004. Publisher: IOP Publishing.

57. V. A. Lashkov, A. G. Karpenko, R. S. Khoronzhuk, and I. C. Mashek, "Effect of Mach number on the efficiency of microwave energy deposition in supersonic flow," *Physics of Plasmas*, vol. 23, p. 052305, May 2016. Publisher: American Institute of Physics.

58. V. Sember, D. V. Gravelle, and M. I. Boulos, "Spectroscopic study of a supersonic plasma jet generated by an ICP torch with a convergent-divergent nozzle," *Journal*

of Physics D: Applied Physics, vol. 35, pp. 1350–1361, June 2002. Publisher: IOP Publishing.

59. Y. G. Utkin, S. Keshav, J.-H. Kim, J. Kastner, I. V. Adamovich, and M. Samimy, "Development and use of localized arc filament plasma actuators for high-speed flow control," *Journal of Physics D: Applied Physics*, vol. 40, pp. 685–694, Jan. 2007. Publisher: IOP Publishing.

60. Y. Kolesnichenko, V. Brovkin, D. Khmara, V. Lashkov, I. Mashek, and M. Ryvkin, "Microwave discharge parameters in supersonic flow," in *40th AIAA Aerospace Sciences Meeting & Exhibit*, Aerospace Sciences Meetings, American Institute of Aeronautics and Astronautics, Jan. 2002.

61. F. J. Gordillo-Vazquez and J. A. Kunc, "Diagnostics of plasmas with substantial concentrations of atomic oxygen," *Physical Review E*, vol. 51, pp. 6010–6015, June 1995.

62. B. Gordiets, C. Ferreira, V. Guerra, J. Loureiro, J. Nahorny, D. Pagnon, M. Touzeau, and M. Vialle, "Kinetic model of a low-pressure $N_2 - O_2$ flowing glow discharge," *IEEE Transactions on Plasma Science*, vol. 23, pp. 750–768, Aug. 1995.

63. N. O'Connor, H. H. Humphreys, and S. Daniels, "Oxygen line ratio method for the determination of plasma parameters in atmospheric pressure discharges using air as the working gas," (Granada, Spain), 31st International Conference on Phenomena in Ionized Gases, July 14-19 2013.

64. M. B. Schulman, F. A. Sharpton, S. Chung, C. C. Lin, and L. W. Anderson, "Emission from oxygen atoms produced by electron-impact dissociative excitation of oxygen molecules," *Physical Review A*, vol. 32, pp. 2100–2116, Oct. 1985.

65. W. H. Soon and J. A. Kunc, "Thermal nonequilibrium in partially ionized atomic oxygen," *Physical Review A*, vol. 41, pp. 825–843, Jan. 1990.

66. A. Bourdon, Y. Térésiak, and P. Vervisch, "Ionization and recombination rates of atomic oxygen in high-temperature air plasma flows," *Physical Review E*, vol. 57, pp. 4684–4692, Apr. 1998.

67. T. Mori, K. Kanou, K. Mizuta, T. Kuramasu, Y. Ishikawa, and S. Arai, "Reactions of highly excited oxygen atoms O($2p^3 3s, {}^5S$) with simple gas molecules," *The Journal of Chemical Physics*, vol. 97, pp. 9094–9098, Dec. 1992.

68. S. Tendo, H. Kohguchi, and K. Yamasaki, "Detection of atomic oxygen O (^3P_J) with vacuum ultraviolet emission subsequent to two-photon absorption," *Chemical Physics Letters*, vol. 710, pp. 96–99, Oct. 2018.

69. U. Meier, K. Kohse-Höinghaus, and T. Just, "H and O atom detection for combustion applications: study of quenching and laser photolysis effects," *Chemical Physics Letters*, vol. 126, pp. 567–573, May 1986.

70. R. E. Walkup, K. L. Saenger, and G. S. Selwyn, "Studies of atomic oxygen in O_2+CF_4 rf discharges by two-photon laser-induced fluorescence and optical emission spectroscopy," *The Journal of Chemical Physics*, vol. 84, pp. 2668–2674, Mar. 1986.

71. J. W. McConkey, C. P. Malone, P. V. Johnson, C. Winstead, V. McKoy, and I. Kanik, "Electron impact dissociation of oxygen-containing molecules–A critical review," *Physics Reports*, vol. 466, pp. 1–103, Sept. 2008.

72. L. R. LeClair, "Production and detection of metastable atomic oxygen.," *Electronic Theses and Dissertations*, Jan. 1993.

73. I. Kanik, C. Noren, O. P. Makarov, P. Vattipalle, J. M. Ajello, and D. E. Shemansky, "Electron impact dissociative excitation of O2: 2. Absolute emission cross sections of the OI(130.4 nm) and OI(135.6 nm) lines," *Journal of Geophysical Research: Planets*, vol. 108, Nov. 2003.

74. P. C. Cosby, "Electron-impact dissociation of oxygen," *The Journal of Chemical Physics*, vol. 98, pp. 9560–9569, June 1993.

75. N. J. Mason and W. R. Newell, "Electron impact dissociation of O2," *Journal of Physics B: Atomic, Molecular and Optical Physics*, vol. 23, pp. 4641–4653, Dec. 1990.

76. Y. Itikawa, A. Ichimura, K. Onda, K. Sakimoto, K. Takayanagi, Y. Hatano, M. Hayashi, H. Nishimura, and S. Tsurubuchi, "Cross Sections for Collisions of Electrons and Photons with Oxygen Molecules," *Journal of Physical and Chemical Reference Data*, vol. 18, pp. 23–42, Jan. 1989.

77. P. W. Erdman and E. C. Zipf, "Excitation of the OI (3s 5s0–3p 5p; λ 7774 å) multiplet by electron impact on O2," *The Journal of Chemical Physics*, vol. 87, pp. 4540–4545, Oct. 1987.

78. A. Granier, D. Chéreau, K. Henda, R. Safari, and P. Leprince, "Validity of actinometry to monitor oxygen atom concentration in microwave discharges created by surface wave in O_2-N_2 mixtures," *Journal of Applied Physics*, vol. 75, pp. 104–114, Jan. 1994.

79. H. M. Katsch, A. Tewes, E. Quandt, A. Goehlich, T. Kawetzki, and H. F. Döbele, "Detection of atomic oxygen: Improvement of actinometry and comparison with laser spectroscopy," *Journal of Applied Physics*, vol. 88, pp. 6232–6238, Nov. 2000.

80. A. Greb, K. Niemi, D. O'Connell, and T. Gans, "Energy resolved actinometry for simultaneous measurement of atomic oxygen densities and local mean electron energies in radio-frequency driven plasmas," *Applied Physics Letters*, vol. 105, p. 234105, Dec. 2014.

81. K. Niemi, S. Reuter, L. M. Graham, J. Waskoenig, N. Knake, V. S.-v. d. Gathen, and T. Gans, "Diagnostic based modelling of radio-frequency driven atmospheric pressure plasmas," *Journal of Physics D: Applied Physics*, vol. 43, p. 124006, Mar. 2010.

82. D. V. Lopaev, A. V. Volynets, S. M. Zyryanov, A. I. Zotovich, and A. T. Rakhimov, "Actinometry of O, N and F atoms," *Journal of Physics D: Applied Physics*, vol. 50, p. 075202, Jan. 2017.

83. J. P. Booth, O. Guaitella, A. Chatterjee, C. Drag, V. Guerra, D. Lopaev, S. Zyryanov, T. Rakhimova, D. Voloshin, and Y. Mankelevich, "Oxygen (^{3}P) atom recombination on a Pyrex surface in an O_2 plasma," *Plasma Sources Science and Technology*, vol. 28, p. 055005, May 2019.

84. F. W. Breitbarth, E. Ducke, and H. J. Tiller, "EPR investigation of plasma-chemical resist etching in O2 and O2/CF4 discharges," *Plasma Chemistry and Plasma Processing*, vol. 10, pp. 377–399, Sept. 1990.

85. P. Macko, P. Veis, and G. Cernogora, "Study of oxygen atom recombination on a Pyrex surface at different wall temperatures by means of time-resolved actinometry in a double pulse discharge technique," *Plasma Sources Science and Technology*, vol. 13, pp. 251–262, Mar. 2004.

86. M. A. Khan and A. M. Al-Jalal, "Cumulative contributions of 3s–np ($n \geq 3$) transitions in comparing O atom densities in low-pressure Ar–O_2 and He–O_2 glow discharges," *Applied Physics Letters*, vol. 89, p. 171501, Oct. 2006.

87. Z. Kregar, R. Zaplotnik, M. Mozetič, and S. Milošević, "Comparison of spatial distributions of atomic oxygen and hydrogen in ICP by means of catalytic probes and actinometry," *Vacuum*, vol. 109, pp. 8–14, Nov. 2014.

88. G. Cartry, X. Duten, and A. Rousseau, "Atomic oxygen surface loss probability on silica in microwave plasmas studied by a pulsed induced fluorescence technique," *Plasma Sources Science and Technology*, vol. 15, pp. 479–488, June 2006. Publisher: IOP Publishing.

89. J. E. Caplinger and G. P. Perram, "The importance of cascade emission and metastable excitation in modeling strong atomic oxygen lines in laboratory plasmas," *Plasma Sources Science and Technology*, vol. 29, p. 015011, Jan. 2020. Publisher: IOP Publishing.

90. J. E. Chilton, J. B. Boffard, R. S. Schappe, and C. C. Lin, "Measurement of electron-impact excitation into the ${3p}^{5}4p$ levels of argon using Fourier-transform spectroscopy," *Physical Review A*, vol. 57, pp. 267–277, Jan. 1998. Publisher: American Physical Society.

91. J. W. McConkey, C. P. Malone, P. V. Johnson, C. Winstead, V. McKoy, and I. Kanik, "Electron impact dissociation of oxygen-containing molecules–A critical review," *Physics Reports*, vol. 466, pp. 1–103, Sept. 2008.

92. Y. Itikawa, "Cross Sections for Electron Collisions with Nitrogen Molecules," *Journal of Physical and Chemical Reference Data*, vol. 35, pp. 31–53, Dec. 2005.

93. T. Tabata, T. Shirai, M. Sataka, and H. Kubo, "Analytic cross sections for electron impact collisions with nitrogen molecules," *Atomic Data and Nuclear Data Tables*, vol. 92, pp. 375–406, May 2006.

94. D. Pagnon, J. Amorim, J. Nahorny, M. Touzeau, and M. Vialle, "On the use of actinometry to measure the dissociation in O2DC glow discharges: determination of the wall recombination probability," *Journal of Physics D: Applied Physics*, vol. 28, pp. 1856–1868, Sept. 1995. Publisher: IOP Publishing.

95. "PHELPS database." http://www.lxcat.laplace.univ-tlse.fr. Accessed: 2013-06-04.

96. "SIGLO database." http://www.lxcat.laplace.univ-tlse.fr. Accessed: 2013-06-04.

97. A. V. Phelps and L. C. Pitchford, "Anisotropic scattering of electrons by N_2 and its effect on electron transport," *Physical Review A*, vol. 31, pp. 2932–2949, May 1985. Publisher: American Physical Society.

98. C. Yamabe, S. J. Buckman, and A. V. Phelps, "Measurement of free-free emission from low-energy-electron collisions with Ar," *Physical Review A*, vol. 27, pp. 1345–1352, Mar. 1983. Publisher: American Physical Society.

99. S. A. Lawton and A. V. Phelps, "Excitation of the $b^1\Sigma_g^+$ state of O_2 by low energy electrons," *The Journal of Chemical Physics*, vol. 69, pp. 1055–1068, Aug. 1978. Publisher: American Institute of Physics.

100. Jeffrey I. Steinfeld, Joseph S. Francisco, and William L. Hase, *Chemical Kinetics And Dynamics*. Englewood Cliffs, New Jersey 07632: Prentice Hall.

101. J. Bittner, K. Kohse-höinghaus, U. Meier, and T. Just, "Quenching of two-photon-excited H(3s, 3d) and O(3p 3P2,1,0) atoms by rare gases and small molecules," *Chemical Physics Letters*, vol. 143, pp. 571–576, Feb. 1988.

102. F. Roux, F. Michaud, and M. Vervloet, "High-Resolution Fourier Spectrometry of $^{14}N_2$ Violet Emission Spectrum: Extensive Analysis of the ($C^3\Pi_u \rightarrow B^3\Pi_g$) System," *Journal of Molecular Spectroscopy*, vol. 158, pp. 270–277, Apr. 1993.

103. Y. Ichikawa, T. Sakamoto, A. Nezu, H. Matsuura, and H. Akatsuka, "Actinometry Measurement of Dissociation Degrees of Nitrogen and Oxygen in N_2–O_2 Microwave Discharge Plasma," *Japanese Journal of Applied Physics*, vol. 49, p. 106101, Oct. 2010.

104. A. Ershov and J. Borysow, "Atomic oxygen densities in a downstream microwave O2/Ar plasma source," *Plasma Sources Science and Technology*, vol. 16, pp. 798–802, Oct. 2007.

105. E. Kemaneci, E. Carbone, M. Jimenez-Diaz, W. Graef, S. Rahimi, J. v. Dijk, and G. Kroesen, "Modelling of an intermediate pressure microwave oxygen discharge reactor: from stationary two-dimensional to time-dependent global (volume-averaged) plasma models," *Journal of Physics D: Applied Physics*, vol. 48, p. 435203, Oct. 2015.

106. G. D. Stancu, O. Leroy, P. Coche, K. Gadonna, V. Guerra, T. Minea, and L. L. Alves, "Microwave air plasmas in capillaries at low pressure II. Experimental investigation," *Journal of Physics D: Applied Physics*, vol. 49, p. 435202, Sept. 2016.

107. Z. Szymanski, Z. Peradzynski, J. Kurzyna, J. Hoffman, M. Dudeck, M. d. Graaf, and V. Lago, "Spectroscopic study of a supersonic jet of laser-heated argon plasma," *Journal of Physics D: Applied Physics*, vol. 30, pp. 998–1006, Mar. 1997. Publisher: IOP Publishing.

108. S. Leonov, V. Bityurin, K. Savelkin, and D. Yarantsev, "Progress in Investigation for Plasma Control of Duct-Driven Flows," in *41st Aerospace Sciences Meeting and Exhibit*, Aerospace Sciences Meetings, American Institute of Aeronautics and Astronautics, Jan. 2003.

109. L. Isola, M. López, B. J. Gómez, and V. Guerra, "On the influence of metastable states and the behavior of the EEDF in the characterization of the negative glow of a N_2-Ar discharge by OES," *Journal of Physics: Conference Series*, vol. 511, p. 012013, May 2014.

REPORT DOCUMENTATION PAGE

Form Approved
OMB No. 0704–0188

1. REPORT DATE *(DD–MM–YYYY)*	2. REPORT TYPE	3. DATES COVERED *(From — To)*
12–24–2020	Doctoral Dissertation	Jan 2018 — Dec 2020

4. TITLE AND SUBTITLE

Spectroscopic Diagnostics for Supersonic Air Microwave Discharges
Spectroscopic Diagnostics for Supersonic Discharges

5a. CONTRACT NUMBER

5b. GRANT NUMBER

5c. PROGRAM ELEMENT NUMBER

6. AUTHOR(S)

Caplinger, James, E., Mr.

5d. PROJECT NUMBER

5e. TASK NUMBER

5f. WORK UNIT NUMBER

7. PERFORMING ORGANIZATION NAME(S) AND ADDRESS(ES)

Air Force Institute of Technology
Graduate School of Engineering and Management (AFIT/ENP)
2950 Hobson Way
WPAFB OH 45433-7765

8. PERFORMING ORGANIZATION REPORT NUMBER

AFIT-ENP-DS-20-D-016

9. SPONSORING / MONITORING AGENCY NAME(S) AND ADDRESS(ES)

Sensors Directorate
Jason Williams, RYMF Branch Chief
2241 Avionics Circle
WPAFB OH 45433-7765
COMM 937-713-8953
Email: jason.williams.95@us.af.mi

10. SPONSOR/MONITOR'S ACRONYM(S)

RYMF

11. SPONSOR/MONITOR'S REPORT NUMBER(S)

12. DISTRIBUTION / AVAILABILITY STATEMENT

DISTRIBUTION STATEMENT A:
APPROVED FOR PUBLIC RELEASE; DISTRIBUTION UNLIMITED.

13. SUPPLEMENTARY NOTES

14. ABSTRACT

Optical Emission Spectroscopy (OES) is an increasingly relevant technique in plasma diagnostics due to its non-invasive nature and simple application relative to other popular techniques. In this work, common OES techniques are combined with novel methods in an effort to provide comprehensive OES techniques for stationary and supersonic air microwave discharges. To this end, a detailed collisional-radiative model for strong atomic oxygen lines has been developed and used to identify the importance of mechanisms including cascade emission and metastable excitation. Using these results, a combined argon actinometry technique was developed which makes use of the two strong oxygen triplets (777 nm and 844 nm) as well as the common N_2/N_2+ method in order to make simultaneous experimental estimates of gas temperature, dissociation fraction, electron temperature and electron density in a medium pressure synthetic air microwave discharge. Finally, a similar technique is proposed and tested in a supersonic flowing air microwave discharge which shows promise for rapid spatial imaging of electron temperature and ionization fraction in high Mach plasma flows.

15. SUBJECT TERMS

OES, microwave discharge, supersonic,atomic oxygen, plasmas

16. SECURITY CLASSIFICATION OF:			17. LIMITATION OF ABSTRACT	18. NUMBER OF PAGES	19a. NAME OF RESPONSIBLE PERSON
a. REPORT	b. ABSTRACT	c. THIS PAGE			Dr. Glen P. Perram, AFIT/ENP
U	U	U	UU	139	19b. TELEPHONE NUMBER *(include area code)* (937) 255-3636, x4504; glen.perram@afit.edu